Theoretical Study of Electron Transfer Reactions by Energy Decomposition

エネルギー分割による電子移動反応の理論的研究

Akihiro Mutsuji

六辻 晶大

Graduate School of Chemical Sciences and Engineering

Hokkaido University

北海道大学大学院総合化学院

March 2025

Contents

Chapter 1

General Introduction

1.1 Electron Transfer Reactions in Chemistry

Molecules consist of atoms. Atoms consist of nuclei and electrons. Chemical reactions are the movement of nuclei and electrons. Electron transfer reaction is a phenomenon in which one electron transfers from an electron donor (D) to an electron acceptor (A). This process can be represented as the following reaction formula.

$$D^- + A \rightarrow D + A^-$$

The donor is oxidized, and the acceptor is reduced in this process. Electron transfer plays fundamental roles in the vast field of chemistry[1]. For example, biochemistry such as natural photosynthesis and aerobic respiration[2], electrochemistry such as organic electrosynthesis and electrocatalysis for oxygen evolution, and photochemistry including photoredox catalysis and solar energy conversion, just to name a few.[3–11] Photochemistry is a key of environmentally friendly chemistry. Indeed, electron transfer is ubiquitous in chemistry and indispensable in our society. Therefore, understanding the mechanism of electron transfer is an essential task for designing and controlling chemical reactions. Electron transfer may be seen as the simplest chemical reaction, at least in the above reaction formula. However, its mechanism is not so simple. In the case of thermal electron transfer in solution, not only the donor and acceptor species but also the surrounding solvent molecules are involved in the activation process. There is a long history of theoretical and experimental studies trying to understand the nature of electron transfer.

1.1.1 Theory by W. F. Libby

Modern studies of electron transfer can date back to the 1940s.[1,12] In those years, experimental measurements of reaction rates were conducted on the electron self-exchange reactions between two transition metal complexes using radioactive isotopes. This trend invoked the interaction between experimental and theoretical studies. In 1952, W. F. Libby proposed his theory trying to explain the magnitudes of experimental rate constants for transition metal complexes.[13,14] He used the Frank-Condon principle[15–17] in his explanation, saying positions of the nuclei were fixed in the process of rapid transfer of an electron. The importance of the orientation of solvent molecules was also discussed. However, his theory required sudden vertical transition of electronic states, which was not likely to occur in the condition. Moreover, energy conservation was not satisfied. Still, these concepts were grasping some important aspects of the phenomenon, leading to the Marcus theory.

1.1.2 The Marcus Theory

In 1956, Rudolph A. Marcus proposed his first theory on the mechanism and rate of electron transfer, which is now known as the Marcus theory, followed by more papers on the theory[1,18–22]. In the theory, potential curves of two electronic states, initial states (before electron transfer) and final state (after electron transfer), are approximated as harmonic potentials along the reaction coordinate. It was assumed that electron transfer occurred at the crossing point of the two harmonic potentials, satisfying the energy conservation. This description led to an important prediction; the existence of the Marcus inverted region (Fig. 1.1).[22] In most chemical reactions, the reaction goes faster when the reaction is more exothermic because the reaction barrier is lower. The same goes for electron transfer when it is not too exothermic, and this region is known as the

Marcus normal region. By lowering the final state potential, electron transfer eventually becomes barrierless (top region). However, lowering the final state potential further creates the barrier again, making electron transfer slower. This extremely exothermic region of electron transfer is called the Marcus inverted region. Though the experimental proof of the existence of the inverted region took a long time, it was clearly proved in 1984 by Miller, Calcaterra and Closs (Fig. 1.2)[23–25], and Marcus received the Nobel prize in chemistry in 1992.[1] Today, many systems in the inverted region, not only simple electron transfer reactions without bond formation neither breaking[26–32] but also proton coupled electron transfer reactions[33–37], are known.

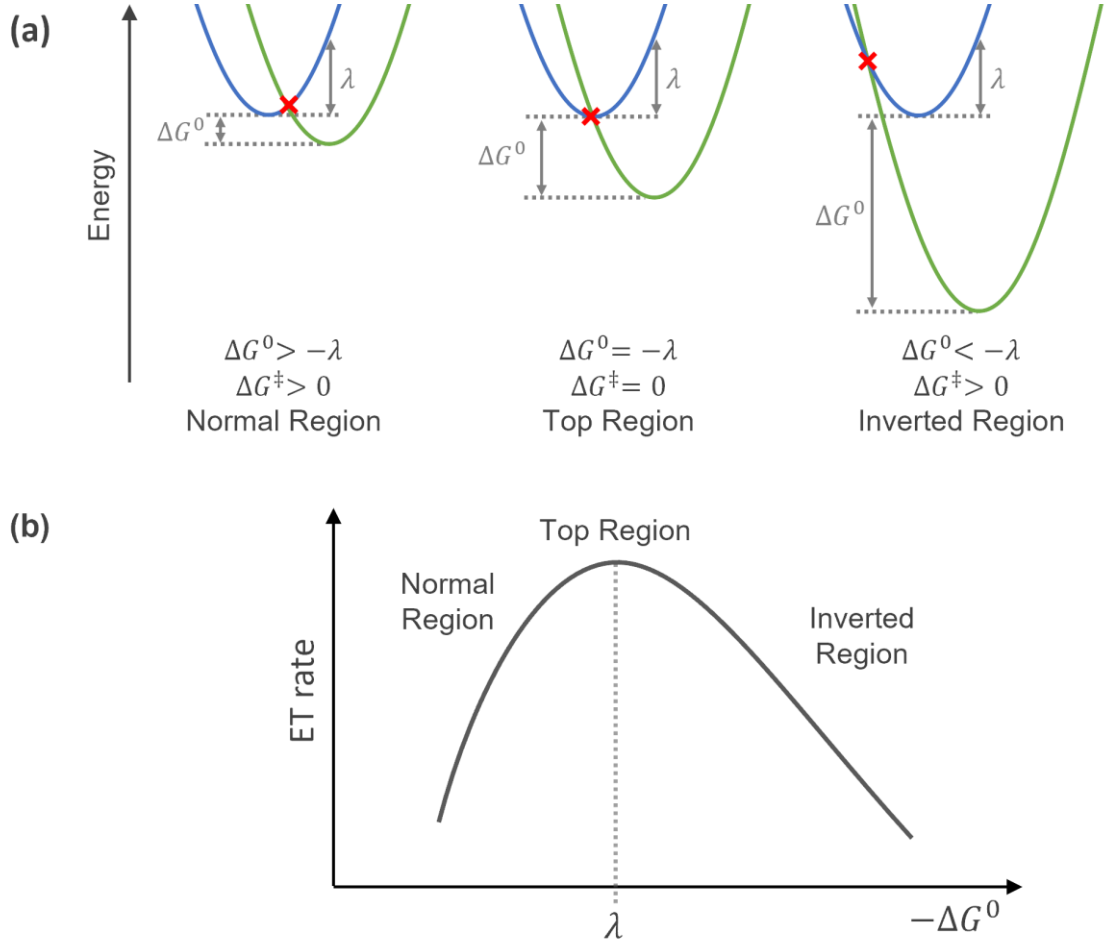

Fig. 1.1 (a) Illustrations of the Marcus normal region, top region, and inverted region. Blue curves are the potentials of initial state, and green curves are the potentials of final state. Value λ is a

parameter called reorganization energy in the Marcus theory. (b) Predicted behavior of the rate constants against the reaction energy. The curve of inverted region is less steep due to the increasing nuclear tunneling effect.

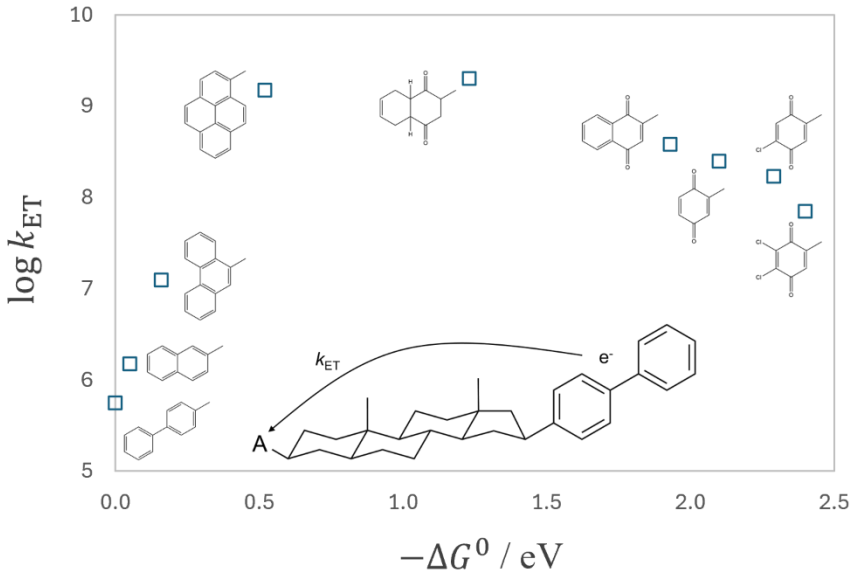

Fig. 1.2 The first clear experimental evidence of the Marcus inverted region. The rate constants of intramolecular electron transfer (k_{ET}), from donor species (1,1-biphenyl) to acceptor species (A) within an anion radical with charge of -1, are plotted against the reaction energies ($-\Delta G^0$) for nine different acceptor species. The data from reference[23] was used for the plots.

1.1.3 Challenges in Electron Transfer

Marcus theory is a milestone in the field of electron transfer, explaining electron transfer with two harmonic potentials and just a few parameters; electronic coupling, reorganization energy, and reaction energy[21]. However, detailed experimental observation of the electron transfer process is not always accessible, especially in the actual synthesis situation where multiple chemical

processes are taking place simultaneously. As will be mentioned in the following chapters, computational chemistry has contributed to the theoretical analysis of the various chemical reactions. Naturally, computational chemistry has been combined with the Marcus theory and applied to the theoretical analysis of electron transfer reactions.[38,39] In this study, focus is on the analysis of electron transfer reactions by geometry optimization, and the target is limited to the intermolecular and intramolecular electron transfer reactions in solution. Though the Marcus theory is a powerful tool, there are still several challenges to be considered in theoretical analysis of electron transfer reactions.

1. Selective calculation of the initial and final state potentials.
2. Geometry optimization of the crossing region.
3. Consideration of activation by solvent orientation change.
4. Consideration of anharmonicity in the potential crossing.
5. Computation of the parameters in the Marcus theory
6. Consideration of the nuclear tunneling effect.

Selective calculations of the initial and final state potentials are needed for geometry optimization of the crossing region. By optimizing the equilibrium of initial and final states and the crossing region geometry, the reaction path of the electron transfer is obtained. If the crossing region is optimized without harmonic approximation, the anharmonicity is naturally incorporated. However, if the solvent molecules are explicitly considered, the vast degree of freedom makes proper geometry optimization difficult. Moreover, the calculation of each parameter in the Marcus theory requires individual considerations in the computation. Lastly, the nuclear tunneling effect calculation is indispensable in the inverted region.[21,40]

1.2 Quantum Chemistry and Computation Chemistry

Quantum chemistry helps us to understand the chemical reactions, or behavior of the nuclei and electrons, through the equations of quantum mechanics, such as the Schrödinger equation.[41] Though the Schrödinger equation is too complicated to be solved analytically in most cases, progress of computer technology has made it practical to compute the solution numerically.

1.2.1 Schrödinger Equation

The Schrödinger equation describes the behavior of non-relativistic quantum mechanical system. This equation was reported in 1926 by Erwin Schrödinger.[41] In eqn (1.1), **H** is the Hamiltonian operator, Ψ is the wavefunction of the system, and E is the energy of the system. In 1928, Paul Dirac reported the theory, known as the Dirac equation, by combining quantum mechanics and special relativity[42]. The Dirac equation led to the concept of the spins (spin-up and spin-down) of electrons.

$$\mathbf{H}\Psi = E\Psi \tag{1.1}$$

By solving the Schrödinger equation, E is obtained. In the field of quantum chemistry, E is the energy of the reaction system or the molecules. However, the Schrödinger equation cannot be solved analytically, except for very limited cases. The difficulty comes from the three-body problem, the complex interactions between multiple nuclei and electrons. Therefore, some approximations were necessary to solve the equation for molecules.

1.2.2 Hartree-Fock Method

In 1930, the Hartree-Fock method[43] was proposed by Vladimir Fock and became the basis of solving the Schrödinger equation for molecules. This method is based on two theories: the Hartree method[44,45] and the Slator determinant.[46] In the Hartree method, the motions of nuclei and electrons are separated, and the motions of nuclei are treated in classical mechanics because nuclei are much heavier than electrons. This approximation is known as the Born-Oppenheimer approximation.[47] On the interactions between electrons, mean-field theory, or self-consistent field theory, was introduced to reduce the three-body problem of electrons into a one-body problem. In this approximation, every electron feels the averaged electric field created by other electrons. Another important approximation is "linear combination of atomic orbitals – molecular orbital (LCAO-MO) approximation".[48] In this approximation, molecular orbitals are expressed as linear combinations of atomic orbitals. The total electron wave function of the Hartree method does not satisfy the antisymmetry, which is requested by the Pauli principle.[49] The Slator determinant was employed to solve the problem of antisymmetry. By introducing above approximations, the Hartree-Fock equation is obtained. The solutions of the Hartree-Fock equation are determined based on the variational principle, and the obtained electronic states are called adiabatic states. However, computers did not exist at that time, and solving the Hartree-Fock equation for molecules by hand calculation was impractical.

1.2.3 Density Functional Theory

Density functional theory (DFT) proposed another way to solve the Schrödinger equation of molecules.[50,51] The DFT has been used widely in computational chemistry because of the good balance of computational cost and accuracy. The first concept of DFT was individually proposed by Llewellyn Thomas and Enrico Fermi in 1927.[52,53] In a framework of DFT calculation, the Schrödinger equation is solved based on the electronic density instead of the electron wave

functions. This treatment reduced the dimension of the equation and had the potential to accelerate the calculation compared to the methods with similar accuracy based on Hartree-Fock method. Since the 1980s, DFT has increasingly become popular not only for crystals, but also for molecules. The original framework of modern DFT based on the Hohenberg–Kohn theorems[54,55] was limited to the electric ground state. Later, time-dependent density-functional theory (TD-DFT) for excited state calculation was developed based on the Runge–Gross theorem.[56]

In practical use of DFT, choice of the functional is crucial.[57] One of the most popular functional is B3LYP functional[58]. However, B3LYP functional has a shortage of poor description of long-range effect. It is known that the long-range correction[59] for density functional is important for the calculation of electron transfer reaction. ωB97X-D[60] and CAM-B3LYP[61] are such functionals. Otherwise, DFT calculation tends to overestimate the delocalization of the transferring electron.[62,63]

1.2.4 Computational Chemistry

In the 1950s, computer technology emerged. A method for solving the Hartree-Fock equation numerically with computer was proposed by Clemens C. J. Roothaan in 1951.[64] The equation known as the Hartree-Fock- Roothaan equation made it practical to compute the electronic states of molecules. This can be considered as the beginning of computational chemistry. Since then, both computer technology and quantum chemistry have developed, and computational chemistry is now an essential tool for understanding and designing chemical reactions. Today, not only experimental chemistry but also information science and machine learning are also working together with computational chemistry.[65,66]

1.2.5 Potential Energy Surfaces and Chemical Reactions

Potential energy surface (PES) is obtained by solving the Schrödinger equation of molecules under the Born-Oppenheimer approximation with the nuclear coordinates as parameters. PES contains huge amounts of information on chemical reactions such as isomers, reaction paths, and dissociation paths.[67,68] PES of a molecule with N atoms has 3N variables, x, y and z coordinate for each nucleus. The number of variables can be reduced from 3N to 3N-6 for a non-linear molecule and 3N-5 for a linear molecule by removing the dimensions of translation and rotation of the entire molecule. On a single PES, there are usually multiple energy minima (Fig. 1.3). Each energy minima corresponds to a different "equilibrium (EQ)" structure of isomer with the same chemical composition. The change of molecular structure from one EQ (reactant) to another EQ (product) corresponds to the chemical reaction. The energy difference between the reactant EQ and product EQ corresponds to the reaction energy (Fig. 1.4). If product EQ is lower than reactant EQ, the reaction is exothermic. If product EQ is higher than reactant EQ, the reaction is endothermic. Along the path connecting two EQs, there is an energy peak, corresponding to "transition state (TS)". The gradients, or the first derivatives of the PES, of both EQs and TSs are ideally zero, or close to zero. EQs and TSs are distinguished by the normal vibrational analysis at the zero-gradient point. If a structure does not have imaginary frequency, it is EQ. If a structure has only one imaginary frequency, it is TS. There are also dissociation channels (DC) where the molecules dissociate.

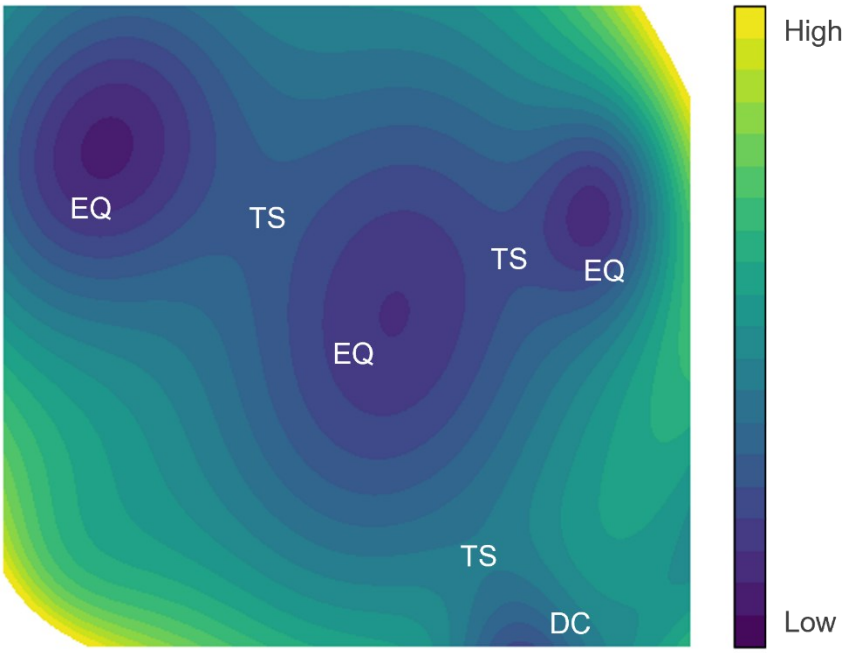

Fig. 1.3 Model potential energy surface with EQs, TSs, and DC.

The height of the TS from the reactant EQ is the reaction barrier (Fig. 1.4). By computing the reaction barrier, the reaction rate constant k can be calculated from the following transition state theory equation.[69]

$$k = \Gamma_n \frac{k_B T}{h} \exp\left(\frac{-\Delta G^{\ddagger}}{RT}\right) \tag{1.2}$$

Coefficient Γ_n represents the nuclear tunneling effect and treated as unity in classical mechanics. k_B is the Boltzmann constant, T is temperature, h is the Planck constant, $\Delta G^{\ddagger}$ is the reaction barrier, and R is the gas constant. This kind of analysis is a static approach since it does not include the dynamics of the molecules. Molecular dynamic is a dynamic approach based on the equation of motion.[70–72] In theory, all the possible products from a reactant, or reactant candidates for the desired product, can be predicted by searching for all the EQ and TSs on a PES. However, since PES has vast space of 3N-6 dimensions, complete search of all the EQ and TS is difficult for large N and efficient methods for PES search are necessary.

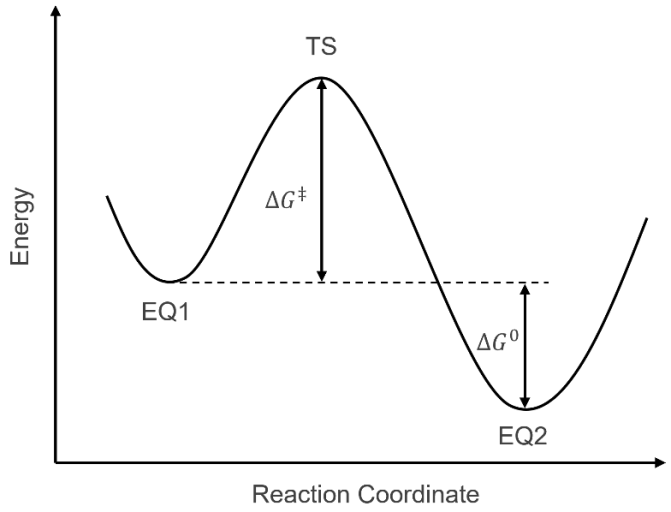

Fig. 1.4 EQs and TS along the reaction coordinate. The reaction energy ΔG^0 and the reaction barrier $\Delta G^{\ddagger}$ are also shown.

1.2.6 Nuclear Tunneling

Nuclear tunneling is a phenomenon of quantum mechanics, in which the quantum wavefunction goes into the classically forbidden area and reaches the opposite area across the barrier with finite possibility.[73,74] Due to this phenomenon, chemical reactions can proceed by tunneling through under the reaction barrier from the reaction region to the product region even when the energy of the molecule is not enough to reach the TS (Fig. 1.5). This effect ($\Gamma_n > 1$) makes the reaction rate constants larger than that of classical mechanics. In many chemical reactions in room temperature or higher temperature, the contribution of nuclear tunneling is relatively small or negligible. However, there are a few cases where the nuclear tunneling effect to the reaction rate constant can be prominent.[73,74]

1. When the temperature is so low that no molecule can reach the transition state, the reaction occurs only by the nuclear tunneling.

2. When the reaction barrier is thin. The thinner the barrier, the higher the possibility of the tunneling by quantum wavefunction. Electron transfer in the Marcus inverted region corresponds to this case.[21,40]
3. When the atom masses are small. The lighter the atoms, the less decay of the quantum wavefunction in the barrier. Proton transfer reaction is a typical example of this case.[75,76] Recently, tunneling phenomena of heavier atoms have also been reported.[77]

Various models have been developed to incorporate the nuclear tunneling effect into the reaction rates. The Wigner model[78] calculates the tunneling effect based on the sharpness of TS and is often used with the transition state theory. The model proposed by Scher and Holstein[79] is a tunneling model for the potential crossing regions explained in the following section.

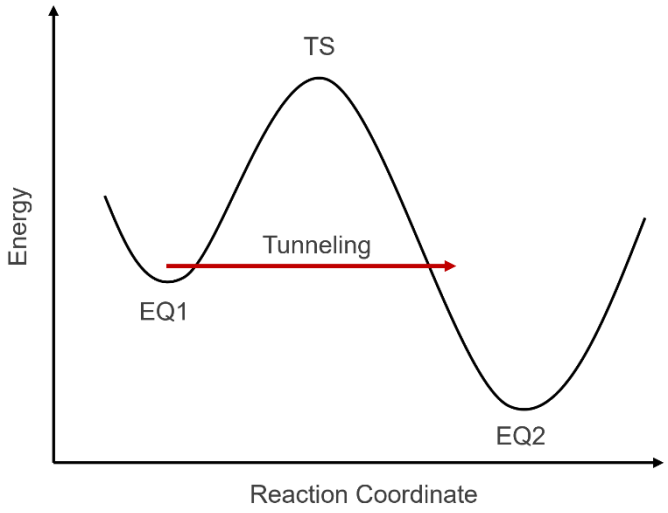

Fig. 1.5 Illustration of the nuclear tunneling through the reaction barrier.

1.3 Potential Crossing

Where the PESs of two different electronic states cross, or when two electronic states degenerate in a certain geometry, transitions of electronic states can take place. Intersystem crossing[80,81] is the radiationless transition between states of two different spin states, such as singlet and triplet. Internal conversion[81] is the radiationless transition between states of the same spin state, such as singlet and singlet, or triplet and triplet. Not only thermal electron transfer but also various important photochemical phenomena are related to these transitions at the crossing regions; photoinduced electron transfer[82,83], excitation energy transfer[84,85], singlet fission[86,87], and triplet-triplet annihilation[88]. Efficiency of fluorescence and phosphorescence are controlled by these transitions.[89] Understanding and controlling the potential crossing are the key of controlling these chemical reactions by molecular design. Depending on the combination of spin states of the crossing potentials, seam of crossing or conical intersection is formed, and they have different shapes of crossing.

1.3.1 Seam of Crossing

The seam of crossing (SX)[90,91] is formed between two PESs with different spin states. SX has the dimensions of 3N-7, removing the six dimensions of translation and rotation and one dimension of solving degeneracy. By searching for a local minimum on the SX (MESX), transitions such as intersystem crossing have been analyzed.[92–97] SX is also formed by crossing of two potentials of "diabatic" states as explained in section 1.3.3.

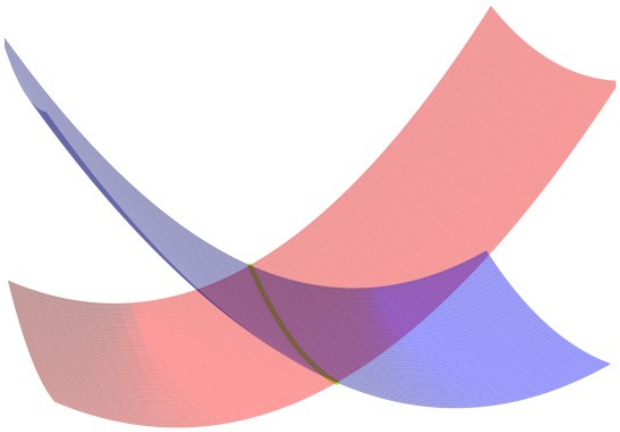

Fig. 1.6 Seam of crossing by two model potential energy surfaces with two variables. The crossing region (one-dimensional in this model) is colored green.

1.3.2 Conical Intersection and Avoided Crossing

The conical intersection (CI)[91,98] is formed between two adiabatic PESs with the same spin states. CI has the dimensions of 3N-8, removing the six dimensions of translation and rotation and two dimensions (called branching plane) of solving degeneracy. By searching for a local minimum on the CI (MECI), transitions such as internal conversion can be analyzed.[99–103] CI has a singular point. At the singular point, the derivatives of potentials are discontinuous, making search for CI harder than that of SX. This problem can be avoided by introducing the avoided model function (AMF) method.[104] The AMF method converts CI into a smooth function, which gives continuous derivatives. The avoided crossing[105–107] is formed around the CI because of mixing of two adiabatic states. The avoided crossing is important when considering the thermal process on the ground state adiabatic PES because the avoided crossing corresponds to the reaction barrier in this case.

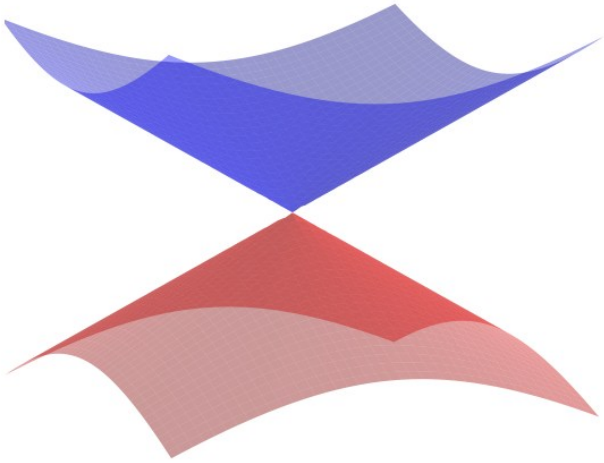

Fig. 1.7 Conical intersection by two model potential energy surfaces with two variables. The CI is zero-dimensional (singular point) in this model.

1.3.3 Adiabatic States and Diabatic States

Diabatic states are the electronic states obtained by transforming the adiabatic states with restrictions such as charge distribution or spin distribution. The diabatic states in two-level potential model is represented by the following matrix $\hat{V}$.[40]

$$\hat{V} = \begin{bmatrix} V_{11} & V_{12} \\ V_{21} & V_{22} \end{bmatrix} \tag{1.3}$$

In this matrix, diagonal component V_{11} and V_{22} are the diabatic potentials and off-diagonal component V_{12} (= V_{21}) is the nonadiabatic coupling between V_{11} and V_{22}. The following relations of adiabatic potentials (E_1 and E_2) and diabatic potentials are obtained by diagonalization of $\hat{V}$.

$$E_1 = \frac{1}{2}(V_{11} + V_{22}) - \frac{1}{2}\sqrt{(V_{11} - V_{22})^2 + 4{V_{12}}^2} \tag{1.4}$$

$$E_2 = \frac{1}{2}(V_{11} + V_{22}) + \frac{1}{2}\sqrt{(V_{11} - V_{22})^2 + 4{V_{12}}^2} \tag{1.5}$$

At the crossing points of two diabatic potentials, namely when $V_{11} = V_{22} = V_x$, the following

equations are held.

$$E_1 = V_x - V_{12} \tag{1.6}$$

$$E_2 = V_x + V_{12} \tag{1.7}$$

Therefore, there is the energy gap of $2V_{12}$ between the two adiabatic PESs at the crossing point (Fig. 1.8). This gap is caused by the mixing of the two diabatic states, or delocalization of the transferring electron in a case of electron transfer reaction.

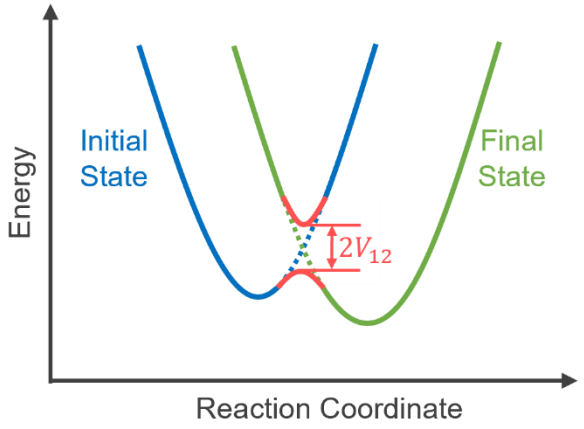

Fig. 1.8 Schematic potential crossing region of two diabatic states and coupling in the Marcus normal region. Curves colored blue and green are the initial and final diabatic states, respectively. The red curves are adiabatic potentials deviating from the diabatic potentials near the crossing region due to the mixing of the electronic states, creating the energy gap of $2V_{12}$.

Use of diabatic potentials is sometimes more convenient than adiabatic potentials. For example, searching for EQs and MESX of diabatic potentials corresponding to a thermal electron transfer is relatively easy. On the other hand, searching for TS of the thermal electron transfer on the electronic ground state of adiabatic potentials is not always feasible. There may be multiple TSs irrelevant to the electron transfer such as rotation of substituent around the desired TS. In the case of the Marcus normal region, the desired TS might be obtained by computing reaction paths

connecting the initial and final EQs by double-end methods.[108] However, such approaches are not available in the case of the Marcus inverted region because the two EQs exist on the two different adiabatic potentials and the TS connecting these EQs do not exist. Moreover, quantum mechanical calculations sometimes give discontinuous PESs around the conical intersection.[109]

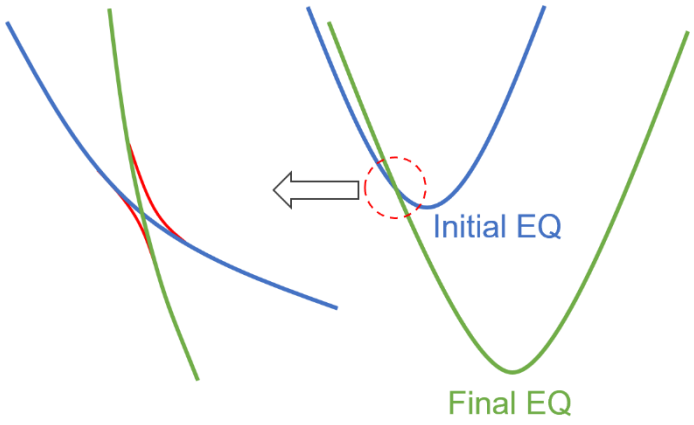

Fig. 1.9 Crossing of diabatic potentials (blue and green) and adiabatic potentials (red) in the Marcus inverted region. Initial EQ and final EQ are on different adiabatic potentials.

1.3.4 Methods for Theoretical Analysis of Electron Transfer

Various methods have been developed for theoretical analysis of electron transfer reactions and other phenomena related to the potential crossing regions. Conventional methods of computational chemistry for this purpose are roughly divided into static analyses and dynamic analyses. Static analyses are also divided into two types. Ones employe harmonic approximation at the EQs based on the vibrational frequency calculation such as the Franck-Condon weighted density of states, Fermi Golden Rule, and the Marcus-Jortner-Levich theory.[21,38,110–112] The other ones optimize the actual potential crossing geometries.[94–97,99–101,103,109,113–116] In this case, selective calculation of the two target electronic states is necessary. This can be done by constrained density functional theory (CDFT)[62,63] or multi-configurational self-consistent field (MCSCF)[117]. However,

it is difficult to calculate the excited state of the charge localized state, and computational cost of MCSCF is huge for geometry optimization. Dynamics analyses such as molecular dynamics have been also employed.[39,118–124]

1.4 Solvent Effect in Computational Chemistry

Many chemical reactions occur in solutions, and consideration of solvent effect in quantum mechanical calculation is necessary for computation in a more realistic reaction situation. There are roughly two ways of incorporating the solvent effect in the quantum mechanical calculation; explicit solvent considerations and implicit solvent methods. The combinations of the explicit solvent and implicit solvent models have been also proposed for taking advantages of both explicit and implicit solvent.[125,126]

1.4.1 Explicit Solvent

Putting explicit solvent molecules into the quantum mechanical calculation with solute is the most straight forward way to consider the solvent effect. There are the following advantages of using explicit solvents.

1. Solvent molecules can participate in the chemical reaction.
2. The specific solvent-solute interactions such as hydrogen bonding and pi-pi interactions can be considered.

On the other hand, there are the following disadvantages.

1. Quantum mechanical calculation is slower, and the computational cost is more expensive compared to the implicit solvent.

2. Large degrees of freedom (the large number of atoms) make geometry optimization and reaction path search extremely exhausting.

1.4.2 Implicit Solvent and Self-Consistent Reaction Field Models

Using implicit solvent model is another conventional way of incorporating the solvent effect. Various implicit solvent models have been developed. The models such as Onsager model are the simplest models using only one spherical or ellipsoidal cavity for representing solvation.[127,128] The self-consistent reaction field (SCRF) models, such as polarizable continuum model (PCM)[129], conductor-like PCM (C-PCM)[130,131], and SMD[132], have been widely used. These models are described as the continuum balk solvent surrounding the explicit solute molecules. Other unique models such as 3D-RISM[133,134] also have been developed. The advantages and disadvantages of implicit solvent models are the opposition of the explicit solvent. The advantages are the following.

1. Quantum mechanical calculation is faster, and the computational cost is cheaper compared to the explicit solvent.
2. Smaller degrees of freedom make geometry optimization and reaction path search drastically simpler.

The disadvantages are the following.

1. Because there are no explicit solvent molecules, they cannot participate in the chemical reaction. The implicit models are usually relaxed to the solute molecules and do not get activated in the activation process of the solute.
2. It is usually impossible in many models to consider the specific solvent-solute interactions such as hydrogen bonding and pi-pi interactions.
3. If the solvent is not parameterized for the implicit solvent method, these parameters

need to be given by users themselves.

The first disadvantage becomes problematic in calculation of electron transfer in solution. It is known that the orientation changes of the solvent molecules surrounding the donor and acceptor species are involved in the activation process and the rate constants depend on the solvent polarity.[23–25]

1.5 Purpose and Overview

1.5.1 Purpose of The Study

The purpose of the studies in this thesis is to develop methods and to establish efficient schemes for analysis of electron transfer reactions by potential crossing region optimization based on energy decomposition, and the target is limited to the intermolecular and intramolecular electron transfer reactions by thermal activation in solution. Photoinduced electron transfer reactions are also very important, but thermal activation is simpler and considered to be more suitable as benchmark systems. As mentioned in section 1.1.3, there are several problems to be considered. They can be rephrased into the following four topics.

1. Development of a diabatization method for selective calculation of the electron localized states.
2. Development of a method to incorporate the solvent activation into the crossing region optimization.
3. Ab initio calculation of parameters in the Marcus theory.
4. Consideration of the nuclear tunneling effect.

In the following chapters, these problems will be dealt with.

1.5.2 Overview of The Thesis

This thesis consists of five chapters.

Chapter 1 presents the general introduction. This chapter presents the fundamental knowledge of the contents in this thesis, including electron transfer, quantum chemistry, computational chemistry, potential crossings, and solvent effects.

Chapter 2 presents the basis of the computer programs and methods used in the study. The following contests are included: geometry optimization functions and general interface function of the Global Reaction Route Mapping program, relation of the EDEEL method and the ONIOM method, the rate constant formula of the Marcus theory, the Scher-Holstein method for the nuclear tunneling, the self-consistent reaction field (especially on C-PCM) with two types of dielectric constants, the energy shift methods for potential crossing region optimization, and the energy decomposition analysis.

Chapter 3 presents the EDEEL method for diabatization of the intermolecular electron transfer systems. The details of the EDEEL method are explained. Besides, results of benchmark calculations with electron self-exchange reactions between the transition metal complexes in aqueous solutions are presented. Calculated electron transfer rate constants show good correlation with the reported experimental values, suggesting the effectiveness of the developed scheme. Details of the activation process, the breakdown of reaction energies and structural deformation, are also presented using the energy decomposition analysis.

Chapter 4 presents the EDEEL method extended for the intramolecular electron transfer systems. Moreover, a newly developed method for incorporating the activation of solvent into the geometry optimization is presented. Just like chapter 3, results of benchmark calculations of intramolecular electron transfer within the radical anions in three different solvents are also

presented. In the calculations, the nuclear tunneling effect was incorporated by the Scher-Holstein method. Calculated rate constants show good correlation with the experimental values from the Marus normal region to the inverted region. Moreover, the reaction energies are decomposed into the solvent activation and donor-acceptor activation, prevailing the different trends of activation in the Marcus normal region and the inverted region.

Chapter 5 presents the general conclusions of this thesis. Summaries of each chapter are presented. Besides, remaining challenges in the theoretical analysis of electron transfer reactions are discussed for future studies.

References for Chapter 1

1 R. A. Marcus, *Angewandte Chemie International Edition in English*, 1993, **32**, 1111–1121.

2 H. B. Gray and J. R. Winkler, *Annu Rev Biochem*, 1996, **65**, 537–561.

3 Y. Yamazaki, K. Ohkubo, D. Saito, T. Yatsu, Y. Tamaki, S. Tanaka, K. Koike, K. Onda and O. Ishitani, *Inorg Chem*, 2019, **58**, 11480–11492.

4 D. Gust, T. A. Moore and A. L. Moore, *Acc Chem Res*, 2009, **42**, 1890–1898.

5 M. H. Shaw, J. Twilton and D. W. C. MacMillan, *Journal of Organic Chemistry*, 2016, **81**, 6898–6926.

6 N. A. Romero and D. A. Nicewicz, *Chem Rev*, 2016, **116**, 10075–10166.

7 N.-T. Suen, S.-F. Hung, Q. Quan, N. Zhang, Y.-J. Xu and H. M. Chen, *Chem. Soc. Rev.*, 2017, **46**, 337–365.

8 K. Tvrdy, P. A. Frantsuzov and P. V Kamat, *Proceedings of the National Academy of*

Sciences, 2011, **108**, 29–34.

9 A. Hagfeldt, G. Boschloo, L. Sun, L. Kloo and H. Pettersson, *Chem Rev*, 2010, **110**, 6595–6663.

10 C. Zhu, N. W. J. Ang, T. H. Meyer, Y. Qiu and L. Ackermann, *ACS Cent Sci*, 2021, **7**, 415–431.

11 M. E. El-Khouly, E. El-Mohsnawy and S. Fukuzumi, *Journal of Photochemistry and Photobiology C: Photochemistry Reviews*, 2017, **31**, 36–83.

12 R. A. Marcus, *Journal of Electroanalytical Chemistry*, 1997, **438**, 251–259.

13 W. F. Libby, *J Phys Chem*, 1952, **56**, 863–868.

14 R. A. Marcus, *J Chem Phys*, 2020, **153**, 210401.

15 J. Franck and E. G. Dymond, *Transactions of the Faraday Society*, 1926, **21**, 536–542.

16 E. U. Condon, *Phys. Rev.*, 1928, **32**, 858–872.

17 H. Mustroph, *ChemPhysChem*, 2016, **17**, 2616–2629.

18 R. A. Marcus, *J Chem Phys*, 1956, **24**, 966–978.

19 R. A. Marcus, *J Chem Phys*, 1957, **26**, 867–871.

20 R. A. Marcus, *J Chem Phys*, 1965, **43**, 679–701.

21 R. A. Marcus and N. Sutin, *Biochimica et Biophysica Acta (BBA) - Reviews on Bioenergetics*, 1985, **811**, 265–322.

22 R. A. Marcus, *Discuss. Faraday Soc.*, 1960, **29**, 21–31.

23 J. R. Miller, L. T. Calcaterra and G. L. Closs, *J Am Chem Soc*, 1984, **106**, 3047–3049.

24 G. L. Closs, L. T. Calcaterra, N. J. Green, K. W. Penfield and J. R. Miller, *J Phys Chem*, 1986, **90**, 3673–3683.

25 G. L. Closs and J. R. Miller, *Science*, 1988, **240**, 440–447.

26 T. Kakitani and N. Mataga, *J Phys Chem*, 1986, **90**, 993–995.

27 N. Mataga, T. Asahi, Y. Kanda, T. Okada and T. Kakitani, *Chem Phys*, 1988, **127**, 249–261.

28 I. R. Gould, Roger. Moody and Samir. Farid, *J Am Chem Soc*, 1988, **110**, 7242–7244.

29 I. R. Gould, D. Ege, S. L. Mattes and S. Farid, *J Am Chem Soc*, 1987, **109**, 3794–3796.

30 I. R. Gould, D. Ege, J. E. Moser and S. Farid, *J Am Chem Soc*, 1990, **112**, 4290–4301.

31 Takeshi. Ohno, Akio. Yoshimura and Noboru. Mataga, *J Phys Chem*, 1990, **94**, 4871–4876.

32 K. Koike, D. C. Grills, Y. Tamaki, E. Fujita, K. Okubo, Y. Yamazaki, M. Saigo, T. Mukuta, K. Onda and O. Ishitani, *Chem. Sci.*, 2018, **9**, 2961–2974.

33 G. A. Parada, Z. K. Goldsmith, S. Kolmar, B. P. Rimgard, B. Q. Mercado, L. Hammarström, S. Hammes-Schiffer and J. M. Mayer, *Science*, 2019, **364**, 471–475.

34 E. R. Sayfutyarova and S. Hammes-Schiffer, *J Am Chem Soc*, 2020, **142**, 487–494.

35 E. R. Sayfutyarova and S. Hammes-Schiffer, *J Phys Chem Lett*, 2020, **11**, 7109–7115.

36 L. F. Cotter, B. P. Rimgard, G. A. Parada, J. M. Mayer and L. Hammarström, *J Phys Chem A*, 2021, **125**, 7670–7684.

37 B. P. Rimgard, Z. Tao, G. A. Parada, L. F. Cotter, S. Hammes-Schiffer, J. M. Mayer and L. Hammarström, *Science*, 2022, **377**, 742–747.

38 R. Borrelli and A. Peluso, *Wiley Interdiscip Rev Comput Mol Sci*, 2013, **3**, 542–559.

39 J. Blumberger, *Chem Rev*, 2015, **115**, 11191–11238.

40 N. Sutin, in *Progress in Inorganic Chemistry*, John Wiley & Sons, Ltd, 1983, pp. 441–498.

41 E. Schrödinger, *Annalen Phys.*, 1926, **384**, 361–376.

42 P. A. M. Dirac and R. H. Fowler, *Proceedings of the Royal Society of London. Series A, Containing Papers of a Mathematical and Physical Character*, 1928, **117**, 610–624.

43 V. Fock, *Z Angew Phys*, 1930, **61**, 126–148.

44 D. R. Hartree, *Mathematical Proceedings of the Cambridge Philosophical Society*, 1928, **24**, 89–110.

45 D. R. Hartree, *Mathematical Proceedings of the Cambridge Philosophical Society*, 1928, **24**, 111–132.

46 J. C. Slater, *Phys. Rev.*, 1929, **34**, 1293–1322.

47 M. Born and R. Oppenheimer, *Ann Phys*, 1927, **389**, 457–484.

48 J. E. Lennard-Jones, *Trans. Faraday Soc.* , 1929, **25**, 668–686.

49 W. Pauli, *Zeitschrift fur Physik*, 1925, **31**, 765–783.

50 P. Geerlings, F. De Proft and W. Langenaeker, *Chem Rev*, 2003, **103**, 1793–1874.

51 N. Mardirossian and M. Head-Gordon, *Mol Phys*, 2017, **115**, 2315–2372.

52 L. H. Thomas, *Mathematical Proceedings of the Cambridge Philosophical Society*, 1927, **23**, 542–548.

53 E. Fermi, *Rend. Accad. Naz. Lincei*, 1927, **6**, 5.

54 P. Hohenberg and W. Kohn, *Phys. Rev.*, 1964, **136**, B864–B871.

55 W. Kohn and L. J. Sham, *Phys. Rev.*, 1965, **140**, A1133–A1138.

56 E. Runge and E. K. U. Gross, *Phys. Rev. Lett.*, 1984, **52**, 997–1000.

57 M. Bursch, J.-M. Mewes, A. Hansen and S. Grimme, *Angewandte Chemie International Edition*, 2022, **61**, e202205735.

58 A. D. Becke, *J Chem Phys*, 1993, **98**, 5648–5652.

59 H. Iikura, T. Tsuneda, T. Yanai and K. Hirao, *J Chem Phys*, 2001, **115**, 3540–3544.

60 J.-D. Chai and M. Head-Gordon, *Phys. Chem. Chem. Phys.*, 2008, **10**, 6615–6620.

61 T. Yanai, D. P. Tew and N. C. Handy, *Chem Phys Lett*, 2004, **393**, 51–57.

62 F. Ding, H. Wang, Q. Wu, T. Van Voorhis, S. Chen and J. P. Konopelski, *J Phys Chem A*, 2010, **114**, 6039–6046.

63 B. Kaduk, T. Kowalczyk and T. Van Voorhis, *Chem Rev*, 2012, **112**, 321–370.

64 C. C. J. Roothaan, *Rev. Mod. Phys.*, 1951, **23**, 69–89.

65 J. A. Keith, V. Vassilev-Galindo, B. Cheng, S. Chmiela, M. Gastegger, K.-R. Müller and A. Tkatchenko, *Chem Rev*, 2021, **121**, 9816–9872.

66 J. Westermayr, M. Gastegger, K. T. Schütt and R. J. Maurer, *J Chem Phys*, 2021, **154**, 230903.

67 S. Maeda, K. Ohno and K. Morokuma, *Phys. Chem. Chem. Phys.*, 2013, **15**, 3683–3701.

68 S. Maeda and Y. Harabuchi, *WIREs Computational Molecular Science*, 2021, **11**, e1538.

69 H. Eyring, *J Chem Phys*, 1935, **3**, 107–115.

70 S. Habershon, D. E. Manolopoulos, T. E. Markland and T. F. Miller, *Annu Rev Phys Chem*, 2013, **64**, 387–413.

71 B. F. E. Curchod and T. J. Martínez, *Chem Rev*, 2018, **118**, 3305–3336.

72 S. A. Hollingsworth and R. O. Dror, *Neuron*, 2018, **99**, 1129–1143.

73 J. Kästner, *WIREs Computational Molecular Science*, 2014, **4**, 158–168.

74 J. Meisner and J. Kästner, *Angewandte Chemie International Edition*, 2016, **55**, 5400–5413.

75 E. F. Caldin, *Chem Rev*, 1969, **69**, 135–156.

76 L. I. Krishtalik, *Biochimica et Biophysica Acta (BBA) - Bioenergetics*, 2000, **1458**, 6–27.

77 C. Castro and W. L. Karney, *Angewandte Chemie International Edition*, 2020, **59**, 8355–8366.

78 E. Wigner, *Phys. Rev.*, 1932, **40**, 749–759.

79 H. Scher and T. Holstein, *Philosophical Magazine B*, 1981, **44**, 343–356.

80 C. M. Marian, *WIREs Computational Molecular Science*, 2012, **2**, 187–203.

81 C. M. Marian, *Annu Rev Phys Chem*, 2021, **72**, 617–640.

82 A. V Akimov, A. J. Neukirch and O. V Prezhdo, *Chem Rev*, 2013, **113**, 4496–4565.

83 D. Escudero, *Acc Chem Res*, 2016, **49**, 1816–1824.

84 F. Zapata, M. Marazzi, O. Castaño, A. U. Acuña and L. M. Frutos, *J Chem Phys*, 2014, **140**, 34102.

85 F. Zapata, M. Nucci, O. Castaño, M. Marazzi and L. M. Frutos, *J Chem Theory Comput*,

2021, **17**, 5429–5439.

86 M. B. Smith and J. Michl, *Chem Rev*, 2010, **110**, 6891–6936.

87 T. Ullrich, D. Munz and D. M. Guldi, *Chem. Soc. Rev.*, 2021, **50**, 3485–3518.

88 P. Bharmoria, H. Bildirir and K. Moth-Poulsen, *Chem. Soc. Rev.*, 2020, **49**, 6529–6554.

89 M. A. Bryden and E. Zysman-Colman, *Chem. Soc. Rev.*, 2021, **50**, 7587–7680.

90 N. Koga and K. Morokuma, *Chem Phys Lett*, 1985, **119**, 371–374.

91 M. J. Bearpark, M. A. Robb and H. Bernhard Schlegel, *Chem Phys Lett*, 1994, **223**, 269–274.

92 P. Zhang, S. Maeda, K. Morokuma and B. J. Braams, *J Chem Phys*, 2009, **130**, 114304.

93 S. Maeda, K. Ohno and K. Morokuma, *J Phys Chem Lett*, 2010, **1**, 1841–1845.

94 Y. Harabuchi, J. Eng, E. Gindensperger, T. Taketsugu, S. Maeda and C. Daniel, *J Chem Theory Comput*, 2016, **12**, 2335–2345.

95 K. Yamazaki, Y. Miyazaki, Y. Harabuchi, T. Taketsugu, S. Maeda, Y. Inokuchi, S. Kinoshita, M. Sumida, Y. Onitsuka, H. Kohguchi, M. Ehara and T. Ebata, *J Phys Chem Lett*, 2016, **7**, 4001–4007.

96 K. Saita, M. Takagi, Y. Harabuchi, H. Okada and S. Maeda, *J Chem Phys*, 2018, **149**, 072329.

97 N. Aizawa, Y. Harabuchi, S. Maeda and Y.-J. Pu, *Nat Commun*, 2020, **11**, 3909.

98 S. Maeda, K. Ohno and K. Morokuma, *J Chem Theory Comput*, 2010, **6**, 1538–1545.

99 Y. Harabuchi, T. Taketsugu and S. Maeda, *Chem Phys Lett*, 2017, **674**, 141–145.

100 S. Kinoshita, Y. Miyazaki, M. Sumida, Y. Onitsuka, H. Kohguchi, Y. Inokuchi, N. Akai, T. Shiraogawa, M. Ehara, K. Yamazaki, Y. Harabuchi, S. Maeda, T. Taketsugu and T. Ebata, *Physical Chemistry Chemical Physics*, 2018, **20**, 17583–17598.

101 K. Ikemoto, T. Tokuhira, A. Uetani, Y. Harabuchi, S. Sato, S. Maeda and H. Isobe, *J Org Chem*, 2020, **85**, 150–157.

102 Y. Nishimoto, *Chem Phys Lett*, 2020, **744**, 137219.

103 S. Kinoshita, Y. Harabuchi, Y. Inokuchi, S. Maeda, M. Ehara, K. Yamazaki and T. Ebata, *Physical Chemistry Chemical Physics*, 2021, **23**, 834–845.

104 S. Maeda, T. Taketsugu, K. Ohno and K. Morokuma, *J Am Chem Soc*, 2015, **137**, 3433–3445.

105 S. Felicetti, J. Fregoni, T. Schnappinger, S. Reiter, R. de Vivie-Riedle and J. Feist, *J Phys Chem Lett*, 2020, **11**, 8810–8818.

106 B. Gu and S. Mukamel, *Chem. Sci.*, 2020, **11**, 1290–1298.

107 C. Zhu and H. Nakamura, *J Chem Phys*, 1995, **102**, 7448–7461.

108 S. Maeda, Y. Harabuchi, M. Takagi, K. Saita, K. Suzuki, T. Ichino, Y. Sumiya, K. Sugiyama and Y. Ono, *J Comput Chem*, 2018, **39**, 233–251.

109 Y. Harabuchi, M. Hatanaka and S. Maeda, *Chem Phys Lett*, 2019, **737**, 100007.

110 S. Chaudhuri, S. Hedström, D. D. Méndez-Hernández, H. P. Hendrickson, K. A. Jung, J. Ho and V. S. Batista, *J Chem Theory Comput*, 2017, **13**, 6000–6009.

111 J. Ulstrup and J. Jortner, *J Chem Phys*, 1975, **63**, 4358–4368.

112 A. Leo and A. Peluso, *J Phys Chem Lett*, 2022, **13**, 9148–9155.

113 A. Mutsuji, K. Saita and S. Maeda, *RSC Adv*, 2023, **13**, 32097–32103.

114 Y. Harabuchi, T. Taketsugu and S. Maeda, *Phys. Chem. Chem. Phys.*, 2015, **17**, 22561–22565.

115 Y. Harabuchi, H. Hayashi, H. Takano, T. Mita and S. Maeda, *Angewandte Chemie International Edition*, 2023, **62**, e202211936.

116 Y. Harabuchi, J. Eng, E. Gindensperger, T. Taketsugu, S. Maeda and C. Daniel, *J Chem Theory Comput*, 2016, **12**, 2335–2345.

117 P. G. Szalay, T. Müller, G. Gidofalvi, H. Lischka and R. Shepard, *Chem Rev*, 2012, **112**, 108–181.

118 J. Blumberger and M. Sprik, *J Phys Chem B*, 2005, **109**, 6793–6804.

119 P. H.-L. Sit, M. Cococcioni and N. Marzari, *Phys Rev Lett*, 2006, **97**, 28303.

120 H. Oberhofer and J. Blumberger, *J Chem Phys*, 2009, **131**, 64101.

121 H. Oberhofer and J. Blumberger, *Angewandte Chemie International Edition*, 2010, **49**, 3631–3634.

122 R. L. Kenion and N. Ananth, *Phys. Chem. Chem. Phys.*, 2016, **18**, 26117–26124.

123 C. A. Rumble and E. Vauthey, *J Phys Chem B*, 2021, **125**, 10527–10537.

124 C. S. Ahart, K. M. Rosso and J. Blumberger, *J Chem Theory Comput*, 2022, **18**, 4438–4446.

125 Q. Cui, *J Chem Phys*, 2002, **117**, 4720–4728.

126 T. Vreven, B. Mennucci, C. O. da Silva, K. Morokuma and J. Tomasi, *J Chem Phys*, 2001,

115, 62–72.

127 J. G. Kirkwood, *J Chem Phys*, 1934, **2**, 351–361.

128 L. Onsager, *J Am Chem Soc*, 1936, **58**, 1486–1493.

129 J. Tomasi, B. Mennucci and R. Cammi, *Chem Rev*, 2005, **105**, 2999–3094.

130 M. Cossi, N. Rega, G. Scalmani and V. Barone, *J Comput Chem*, 2003, **24**, 669–681.

131 V. Barone and M. Cossi, *J Phys Chem A*, 1998, **102**, 1995–2001.

132 A. V Marenich, C. J. Cramer and D. G. Truhlar, *J Phys Chem B*, 2009, **113**, 6378–6396.

133 A. Kovalenko and F. Hirata, *J Chem Phys*, 1999, **110**, 10095–10112.

134 C. Yang, Y. Watanabe, N. Yoshida and H. Nakano, *J Phys Chem A*, 2019, **123**, 3344–3354.

Chapter 2

Computational Methods for This Thesis

2.1 GRRM Program

The Global Reaction Route Mapping (GRRM) program[1,2] is a computer program for molecular geometry optimization and automated reaction path search on PESs. GRRM itself does not have a function of ab initio calculation such as density functional theory. GRRM is used by being combined with an arbitral ab initio program for quantum mechanical calculation. In this thesis, the Gaussian16 program[3] was employed as ab initio program. In addition to common methods such as normal mode analysis (FREQ), minimum point optimization (MIN), and saddle-point optimization (SADDLE), various unique computational methods are implemented in GRRM. One of them is Anharmonic Downward Distortion Following (ADDF) method.[4–6] In the ADDF method, reaction paths are searched automatically by detecting and following the anharmonic downward distortions (ADD) on the PESs. The other unique method is the Artificial Force Induced Reaction (AFIR) method.[7,8] In the AFIR method, reaction paths are searched automatically by applying the artificial force onto the fragments of the target system. The crossing point optimization (OptX with MIN)[9,10] is an important method for this study of electron transfer reaction.

2.1.1 Geometry Optimization

Molecular geometries are optimized using information of the PES; energy itself and gradient of the PES, or the first derivatives of the energy. The second derivatives of the energy, called hessian, are also frequently used. The energy, gradients, and hessians are calculated by an ab initio program. Information flow between GRRM and an ab initio program is presented in Fig. 2.1. GRRM reads

the input information (type of optimization, selection of ab initio program, charge and spin multiplicity of the input system, initial geometry, and other computational options) from the input file named xxx.com (xxx is an arbitral string called “job name”). The initial geometry is given to the ab initio program. Then the ab initio program computes energy, gradients (and hessians if required) of the given geometry, and returns these values to GRRM. GRRM updates the geometry based on the received energy and gradients. Again, GRRM lets the ab initio program compute the energy and gradients of the updated geometry. This cycle repeats until the gradients and geometry update get smaller than the threshold. Normal mode analysis is often performed after the cycle to confirm the optimized geometry is EQ (, or TS in SADDLE calculation).

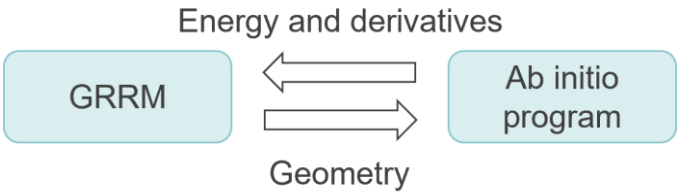

Fig. 2.1 The GRRM program and ab initio program.

2.1.2 AFIR Method

The AFIR method applies artificial forces between two atoms A and B of the input structure.[7,8] The artificial forces push together or pull apart the atoms and induce chemical reactions in virtual space. This corresponds to modifying the original PES by adding the AFIR function so that the reaction barrier is erased, and geometry is optimized from one EQ to another EQ by usual local minimum optimization algorithm (Fig. 2.2). The obtained reaction path from this optimization is called AFIR path and is usually a good approximation of the true reaction path. Approximate TS, or path top (PT), can be also detected on the AFIR path from the raw energies (energies before adding AFIR function) on the AFIR path.

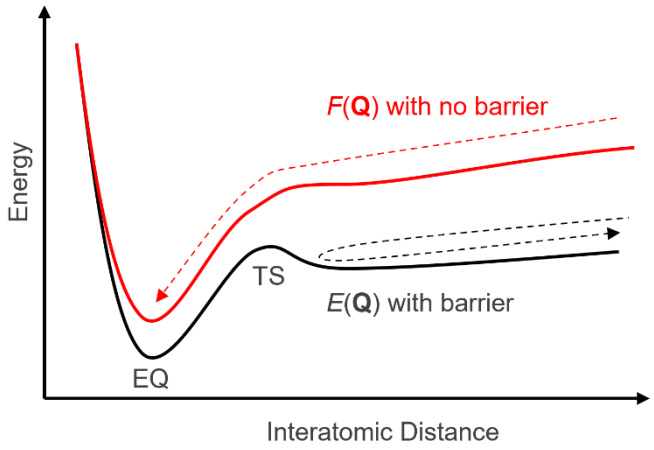

Fig. 2.2 Schematic AFIR function (red) and original potential energy surface (black) of collision between two atoms.

The AFIR function $F(\mathbf{Q})$ defined for fragments A and B is presented in eqn (2.1).[7,8]

$$F(\mathbf{Q}) = E(\mathbf{Q}) + \rho\alpha \frac{\sum_{i\in A}\sum_{j\in B}\omega_{ij}r_{ij}}{\sum_{i\in A}\sum_{j\in B}\omega_{ij}} \tag{2.1}$$

The first term $E(\mathbf{Q})$ is the raw energy at the geometry $\mathbf{Q}$. The second term is the artificial force term and contains four parameters. Coefficient α determines the strength of the force. Coefficient ρ is constant value 1.0 or -1.0. The rest part is sum of the interatomic distance r_{ij} between atoms i and j, weighted by parameter ω_{ij}. The weight ω_{ij} is defined in eqn (2.2) with the covalent radii R_i and R_j for atoms i and j, respectively.

$$\omega_{ij} = \left[\frac{R_i + R_j}{r_{ij}}\right]^6 \tag{2.2}$$

Coefficient α is calculated from eqn (2.3) and obtained as the mean force that a pair of two argon atoms feels in the collision with collision energy γ. Parameters R_0 and ε are the standard value of Lennard-Jones potential for the interaction between two argon atoms.

$$a = \frac{\gamma}{\left[2^{-\frac{1}{6}} - \left(1 + \sqrt{1 + \frac{\gamma}{\varepsilon}}\right)^{-\frac{1}{6}}\right] R_0} \tag{2.3}$$

By specifying larger γ value, larger area on the PES is searched by getting over higher barriers. This corresponds to increasing the temperature of the reaction system in actual experiments.

There are three varieties of the AFIR methods: the manually applied AFIR method, the multi-component algorithm (MC-AFIR)[8,11], and the single-component algorithm (SC-AFIR)[12,13]. The AFIR method gives a huge reaction path network. The rate constant matrix contraction (RCMC) method developed by Sumiya et al. realized kinetic simulation on the network.[14,15] Also, the SC-AFIR method can be combined with kinetic-based navigation.[16,17] In this thesis, the SC-AFIR was employed for conformation search with relatively weak artificial force and 'EQOnly' option. The SC-AFIR automatically assigns fragments and optimized the geometry with AFIR function. By repeating the process from obtained EQs, network connecting EQs called reaction network is obtained. 'EQOnly' option makes GRRM optimize only EQs and reduces computational cost.

2.1.3 OptX

The OptX calculation with MIN optimizes a local minimum on crossing region (MESX or MECI) between two PESs.[9,10] Choice of MESX optimization or MECI optimization must be given in the input file. In this calculation, the energies and gradients of the two PESs at a geometry are needed. Therefore, the GRRM program lets the ab initio program compute these values two times with the same geometry and different electronic states. The gradient projection (GP) method[9,18] is the algorithm used for crossing region optimization in this study. In the GP method, the gradient $\mathbf{g}^{GP}$ is calculated by the following equations.

$$\mathbf{g}^{\mathrm{GP}} = 2[E^{\mathrm{X}}(\mathbf{Q}) - E^{\mathrm{Y}}(\mathbf{Q})]\frac{\mathbf{v}^{\mathrm{DGV}}}{|\mathbf{v}^{\mathrm{DGV}}|} + \mathbf{P}\frac{1}{2}\left[\frac{dE^{\mathrm{X}}(\mathbf{Q})}{d\mathbf{Q}} + \frac{dE^{\mathrm{Y}}(\mathbf{Q})}{d\mathbf{Q}}\right] \tag{2.4}$$

$$\mathbf{v}^{\mathrm{DGV}} = \frac{dE^{\mathrm{X}}(\mathbf{Q})}{d\mathbf{Q}} - \frac{dE^{\mathrm{Y}}(\mathbf{Q})}{d\mathbf{Q}} \tag{2.5}$$

The gradient $\mathbf{g}^{\mathrm{GP}}$ consists of two terms. The first term is for minimizing the energy difference between two PESs, in which $E^{\mathrm{X}}(\mathbf{Q})$ and $E^{\mathrm{Y}}(\mathbf{Q})$ are the energies of two states X and Y at the same geometry $\mathbf{Q}$. The vector $\mathbf{v}^{\mathrm{DGV}}$ is the difference gradient vector (DGV) between the two PESs. The matrix P is the projection matrix $\mathbf{P}$, and different definitions of P are used for MESX optimization and MECI optimization, respectively. For MESX optimization, the following definition of $\mathbf{P}$ is used.

$$\mathbf{P} = \mathbf{1} - \frac{\mathbf{v}^{\mathrm{DGV}}\left(\mathbf{v}^{\mathrm{DGV}}\right)^{T}}{|\mathbf{v}^{\mathrm{DGV}}|^{2}} \tag{2.6}$$

For MECI optimization, the following definition of $\mathbf{P}$ is used. The third term is added to the $\mathbf{P}$ for MESX optimization. Another vector $\mathbf{v}$' is a vector non-parallel to $\mathbf{v}^{\mathrm{DGV}}$ on the blanching plane of CI. In the OptX calculation, $\mathbf{v}$' is calculated by the branching plane updating method.

$$\mathbf{P} = \mathbf{1} - \frac{\mathbf{v}^{\mathrm{DGV}}\left(\mathbf{v}^{\mathrm{DGV}}\right)^{T}}{|\mathbf{v}^{\mathrm{DGV}}|^{2}} - \frac{\mathbf{v}'(\mathbf{v}')^{T}}{|\mathbf{v}'|^{2}} \tag{2.7}$$

The $\mathbf{P}$ removes the gradient elements that solve the degeneracy from the averaged gradient of the two potentials in the second term of $\mathbf{g}^{\mathrm{GP}}$. A penalty function method[19,20] is also available in the OptX calculation as the alternative algorithm but not employed in this study.

2.2 General Interface for Diabatization

The general interface feature is implemented in the GRRM program for the use of arbitral ab initio programs with an external program in addition to the officially supported ab initio programs.

This feature also allows the user to modify energy and its derivatives with methods implemented in the external program. In the calculation with the general interface, the GRRM program creates the file named xxx_INP4GEN.rrm (xxx is the job name). This is the input file for the external program and includes the following information.

1. Tasks that the external program is supposed to perform such as calculation of energy, gradient, and hessian.
2. Choice of initial guess in the quantum chemical calculation.
3. The state to be calculated. Only the number “1” is written for the calculation on single PES. The number “1” or “2” is written alternately in the OptX calculation.
4. The number of atoms and the geometry of the target system to be calculated.

Then, the external program is executed by the command “aaa xxx”. “aaa” is the name of the external program specified with the option line “sublink = aaa” in the input file. The external program is required to create one or multiple input files for an arbitral ab initio program. The external program executes the ab initio program and lets the program calculate energy, gradient (, and hessian if requested in the xxx_INP4GEN.rrm). After the energy calculation, the external program reads requested values from the output files of the ab initio program. Then, the external program creates the file named xxx_OUT4GEN.rrm. This is the output file to be read by the GRRM program and must include the following information in the specific format.

1. The geometry same as the one in xxx_INP4GEN.rrm
2. Calculated energy, gradient (, and hessian if requested).

When the hessian is not requested, the values should be filled with zero. Other information such as spin multiplicity, dipole moment, dipole derivatives, and polarizability are also required to be written in the output. However, these values are not used for geometry optimization and can be filled with zero.

In the OptX calculation, the process of reading xxx_INP4GEN.rrm and creating xxx_OUT4GEN.rrm is repeated twice for state 1 and 2. The point of coding an external program for the OptX calculation is letting the external program calculate both two states when the first state is requested. This gives more flexibility to the method implemented in the external program, allowing the external program to add corrections to the energy of the first state using the information of the two states. The EDEEL methods[21] in chapter 2.3 were implemented as an external program for the general interface calculation.

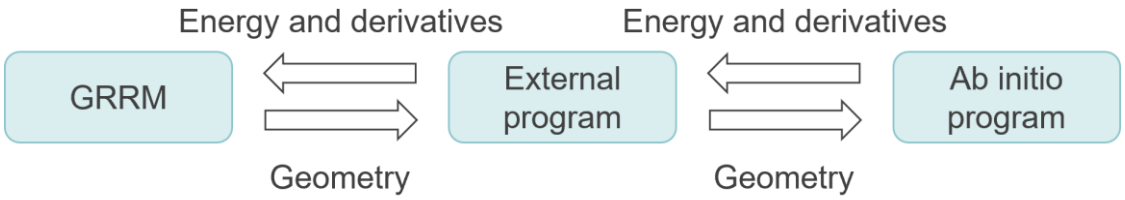

Fig. 2.3 Workflow with general interface feature of the GRRM program.

2.3 The EDEEL Method and The ONIOM Method

In this thesis, an energy extrapolation method called "energy decomposition and extrapolation-based electron localization (EDEEL)" method[21] has been developed and used for selective calculation of the initial and final states of electron transfer reactions. The EDEEL method was developed based on the extrapolation concept of another energy extrapolation method called "our own N-layered integrated molecular orbital and molecular mechanics (ONIOM)" method[22,23]. The ONIOM method was developed by Dr. Keiji Morokuma for calculation of large systems. Balancing both computational cost and accuracy is an important task in computational chemistry, especially for large systems. Various energy extrapolation methods have been developed for this purpose, and the ONIOM method is one of such approaches. The ONIOM method has been frequently used to analyze chemical reactions in large systems such as proteins and catalysts. The

system is divided into two or more regions (Fig. 2.4). Usually, the most important reaction center is assigned to the "model" region. The energy of the model region is calculated at the high computational level of quantum mechanics ($E_{\text{model}}^{\text{high}}$) and at a lower level such as molecular mechanics ($E_{\text{model}}^{\text{low}}$). The energy of the entire system, or "real" system, is also calculated at the low level ($E_{\text{real}}^{\text{low}}$). The energy of the real system ($E_{\text{real}}^{\text{high}}$) is extrapolated by the following equation.

$$E_{\text{real}}^{\text{high}} = E_{\text{real}}^{\text{low}} - E_{\text{model}}^{\text{low}} + E_{\text{model}}^{\text{high}} \tag{2.8}$$

When atoms in the model region have covalent bonds with atoms in other regions, the bonds are cut, and the bond of the model region is capped with hydrogen atoms. These capping atoms are also called link atoms.

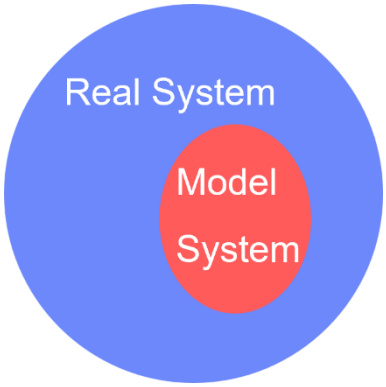

Fig. 2.4 Schematic representation of real system and model system in ONIOM method. The model system is a part of the real system.

Two types of the EDEEL methods have been developed for diabatization. One is for intermolecular electron transfer between separated donor and acceptor species[21], and the other one is for intramolecular electron transfer between bridged donor and acceptor species. The EDDEL methods use energy extrapolation schemes similar to the ONIOM method. The EDEEL

methods were implemented as an external program to be used with general interface feature of the GRRM program. Theoretical details of the EDDEL methods are described in chapter 3 and 4 for intermolecular and intramolecular electron transfer, respectively. In short, the EDEEL methods need the following input in addition to the input for the GRRM program.

1. Choice of the EDEEL method for intermolecular or intramolecular electron transfer.
2. Definition of the donor, acceptor, (and linker if exists) region.
3. Charge and spin multiplicity of each calculation.
4. Computational level including the SCRF method.
5. Choice of energy correction method if needed.

The procedure of the geometry optimization using the GRRM program, the EDEEL method, and the Gaussian 16 is shown in the following Fig. 2.5.

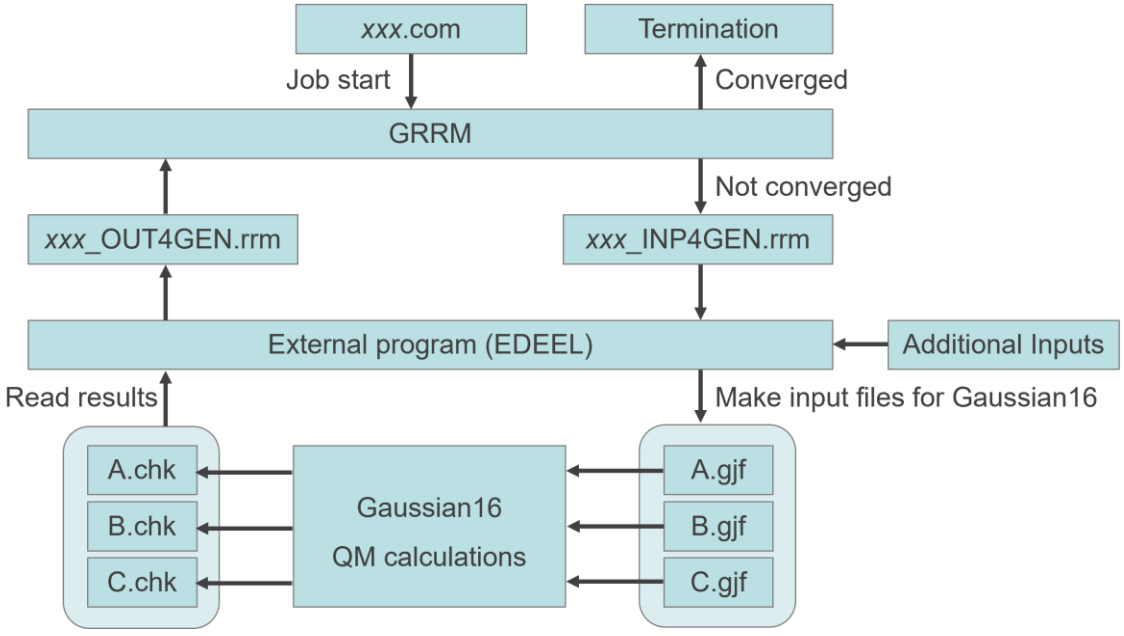

Fig. 2.5 Procedure of the GRRM program, EDEEL method, and Gaussian16. The optimization job starts from an input file "*xxx*.com" and repeats the cycle of geometry optimization by the GRRM program and quantum mechanical (QM) calculation by Gaussian16 mediated by the EDEEL method program. Once the optimization gets converged, the job is terminated.

2.4 The Marcus Theory for Electron Transfer Rate Constant Calculation

A basic form of the electron transfer rate constant by the Marcus theory[24] is presented in the following equation,

$$k_{\mathrm{ET}} = \Gamma_{\mathrm{n}} \frac{2|V_{12}|^2}{h} \left(\frac{\pi^3}{\lambda k_B T}\right)^{1/2} \exp\left(-\frac{\Delta G_{\mathrm{na}}^{\ddagger}}{RT}\right) \tag{2.9}$$

where h is the Planck constant, k_{B} is the Boltzmann constant, T is the temperature, and R is the gas constant. For the evaluation of the electron transfer rate constants by the Marcus theory, the three parameters, the coupling constant V_{12}, the reorganization energy λ, and is the Gibbs free energy of activation $\Delta G_{\mathrm{na}}^{\ddagger}$ (subscript "na" indicates "non-adiabatic") are necessary. Nuclear tunneling factor Γ_{n} is often treated as unity in the Marcus normal region. The coupling constant expresses interaction between the initial (before electron transfer) and final (after electron transfer) states. The reorganization energy corresponds to the curvature of the two harmonic energy potentials. Though the different versions of the rate constant equation are used in chapters 3 and 4 respectively, these three parameters are still the key factors of the rate constants.

2.5 Self-Consistent Reaction Field and Dielectric Constants

In this thesis, C-PCM[25,26], one of the self-consistent reaction field (SCRF) methods, was used for consideration of the solvent effect in the reaction. In the C-PCM, solvent is approximated as the continuum model surrounding the solute molecules within the cavity formed of over-lapping spheres. Each sphere is usually put at the nuclei coordinate of each atom. There are several methods to determine the radii of the spheres[27], and the most straight forward way may be to scale the van der Waals radii of the atoms with a certain constant. Users can specify the scale value, and the common choices are from 1.1 to 1.4.[27] A larger scale value leads to less electrostatic

interaction between the solvent and solute. Therefore, proper scale value may depend on the combination of the solvent and solute, especially solvent polarity and solute charge. The cavity surface is divided into multiple small triangle-shaped areas, called “tesserae”, with point charges on each center of the triangles.[26]

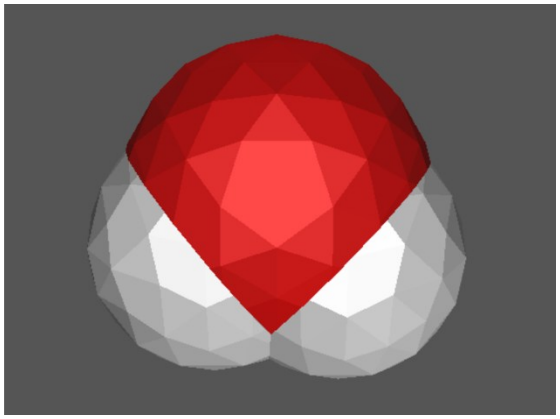

Fig. 2.6 Tesserae of C-PCM (water solvent) cavity for a single water molecule. The red sphere corresponds to the oxygen atom and white spheres correspond to hydrogen atoms. The cavity surfaces consist of small triangles called “tesserae”. The point charges are located at the center of each tessera (not shown in Fig. 2.6). The tesserae data file was created by the Gaussian16 program and visualized by the Geomview program[28].

In the SCRF methods, polarization of the solvent is expressed as distribution of the point charges, which is controlled by two solvent dielectric constants, the static dielectric constant and the optical dielectric constant. Both constants are dimensionless quantities, and each solvent has different values. The static dielectric constant ε_s, or relative permittivity in other words, is defined in the following equation as the ratio of the absolute permittivity of the solvent ε and the permittivity of vacuum ε_0.

$$\varepsilon_s = \frac{\varepsilon}{\varepsilon_0} \tag{2.10}$$

Non-polar solvents have small static dielectric constants, and polar solvents have large static dielectric constants. For example, the static dielectric constants used in Gaussian 16 program for water is 78.355300, and for benzene is 2.270600. On the other hand, the optical dielectric constant ε_∞ is related with the refractive index n as the following.[26]

$$\varepsilon_\infty = n^2 \tag{2.11}$$

Unlike the static dielectric constants, the range of optical dielectric constants is much narrower. Moreover, the optical dielectric constants of non-polar solvent can be larger than that of polar solvent. For example, the optical dielectric constants used in Gaussian 16 program for water is 1.777849, and for benzene is 2.253301. The optical dielectric constants can be considered as the mobility of electrons in the solvent molecules. These two dielectric constants represent the flexibility of charge redistribution on the tesserae. The larger value means larger flexibility. The static and optical dielectric constants correspond to the slow and fast charge redistribution, or relaxation of the solvent in long- time and short-time scales, respectively.[26,29] The slow charge redistribution, which is controlled by the static dielectric constants, corresponds to the orientation change of the solvent molecules or the movement of the nuclei.

It is also possible to save the relaxed point charges on tesserae (corresponding to equilibrium solvation) and use them in other calculations with exactly the same geometry of solute but different electronic states such as different charge or excited state without orientation change of the solvent molecules (corresponding to non-equilibrium solvation). This allows us to calculate the Franck-Condon states of vertical transitions such as photoexcitation and emission.[26,30] In this case, only the electron distribution of solvent molecules is relaxed to the new electronic state immediately, and the nuclei of the solvent molecules are still fixed. This situation is expressed

with the optical dielectric constant. In the solvent activation energy shift method described in chapter 2.6, the C-PCM are relaxed including the orientation to the initial and final state, respectively.

2.6 C-PCM and Point Charges on Tesserae

In the C-PCM, point charges on the tesserae are obtained as solution of the following equation[26],

$$\mathbf{Sq} = -f(\varepsilon)\mathbf{V} \tag{2.12}$$

, in which matrix **S** consists of the following elements of tesserae.

$$\begin{cases} S_{ii} = 1.0694\sqrt{\dfrac{4\pi}{a_i}} \\ S_{ij} = \dfrac{1}{|r_i - r_j|} \end{cases} \tag{2.13}$$

The area and center coordinate of *i*-th tessera are expressed as a_i and r_i, respectively. Vectors **q** and **V** have the point charges and the total electrostatic potential created by solute molecules, respectively, as their elements. The function $f(\varepsilon)$ is shown below.

$$f(\varepsilon) = \frac{\varepsilon - 1}{\varepsilon + X} \tag{2.14}$$

The dielectric constant ε is the static or optical one depending on the calculation, and X is an adjusted parameter. In the non-polar limit, both static and optical dielectric constants are the same as the ones of vacuum, namely $\varepsilon_s = \varepsilon_\infty = 1$. In this case, $f(\varepsilon)$ becomes 0, leading to **q**=**0**. This means all the point charges are 0 (neutral), and there is no electrostatic interaction between the C-PCM and solute molecules. Therefore, the obtained energy, except non-electrostatic interactions, should be the same as one in vacuum. This hypothesis was confirmed for the case of equilibrium solvation ($\varepsilon_s = 1$) in Gaussian16. However, in the case of non-equilibrium solvation ($\varepsilon_\infty = 1$), the

self-consistent field calculation failed with energy of “NaN (not a number)”. It is likely that this type of calculation is unexpected.

2.7 Energy Shift Methods for Crossing Region Optimization

Energy shift methods, which simply add a constant value to the electronic energy obtained by ab initio calculation, have been developed for optimization of potential crossing regions.[31–33] There are two purposes of using the energy shift methods. One is as a convenient way of incorporating a specific contribution to the energy difference between the two potentials which is often difficult or computationally demanding to calculate explicitly in quantum mechanical calculation.[31,33] The other purpose is to avoid the rather technical problems in potential energy surface calculation.[32] The first energy shift method was developed by Hatanaka and Morokuma for the reaction coordinate exploration of emission and quenching of the Lanthanide complexes.[31] In this method, the energy of electronic excitation between 4f orbitals is added to the energy of the electronic ground state. This treatment is based on the fact that electrons in 4f orbitals in the lanthanide complexes are shielded from the environment by the outer 5s and 5p electrons, implying the excitation energies are almost constant regardless of the ligands. Excitation states of the lanthanide complexes are extremely complicated and difficult to calculate selectively, and this energy shift method allows to approximate the excited states. Another example is the method developed by Harabuchi et al. in 2019 for exploration of the MECI geometry.[32] This method made it possible to obtain the approximated MECI geometry by avoiding the discontinuities of potential energy surfaces calculated by TD-DFT around the conical intersection between S_0 and S_1 states. One last example is the method developed by Harabuchi et al. in 2023 for the reaction path exploration of Knowles hydroamination using the photoredox-catalyzed radical reaction.[33] In this method, the experimentally measured redox potentials of a photocatalyst were added to potential

energy surface of the substrate to avoid the quantum mechanical calculation of the large catalyst and its counter anion.

In this thesis, the solvent activation energy shift (SAES) method was developed for consideration of the thermal activation or orientation change of the solvent molecules surrounding the donor and acceptor species. This method makes it possible to optimize the crossing region geometry of donor and acceptor species with contributions of the solvent activation without the explicit solvent molecules into the calculation, resulting in the drastic reduction of the computational cost due to the explicit solvents. This method also allows systematic SX scanning by adjusting the solvent orientation coordinate, or the balance of the solvent activation by orientation change and donor-and-acceptor activation by deformation. The details of the SAES method are described in chapter 4, but one unique feature is that the SAES method has the coordinate of solvent orientation in the energy shift value while other energy shift methods do not. In other words, the SAES method also can be seen as the penalty energies to unify the solvent orientation coordinate between the two potential energy surfaces. Strictly speaking, the coordinate of solvent molecules, even if implicit model, should be the same between the two states when optimizing the crossing region geometry. Otherwise, the solvent geometries may be practically different between the two states at the obtained crossing point even though the solute geometries are the same.

2.8 Scher-Holstein Method for Nuclear Tunneling Effect

As mentioned in chapter 1.2.6, the nuclear tunneling effect can be critical in the electron transfer in the inverted region due to the thinner reaction barrier. In chapter 4, the method proposed by Scher and Holstein[34,35] is used for incorporating the nuclear tunneling effect into the

intramolecular electron transfer rate constants. The origin of this Scher-Holstein method was developed for electron transfer reactions in molecular crystal models.[36–39] Afterwards, it has been also applied to the intermolecular electron transfer reaction in solution for considering the nuclear tunneling effect.[35,40,41] This method takes account of not only the reaction energy but also the effect of temperature.

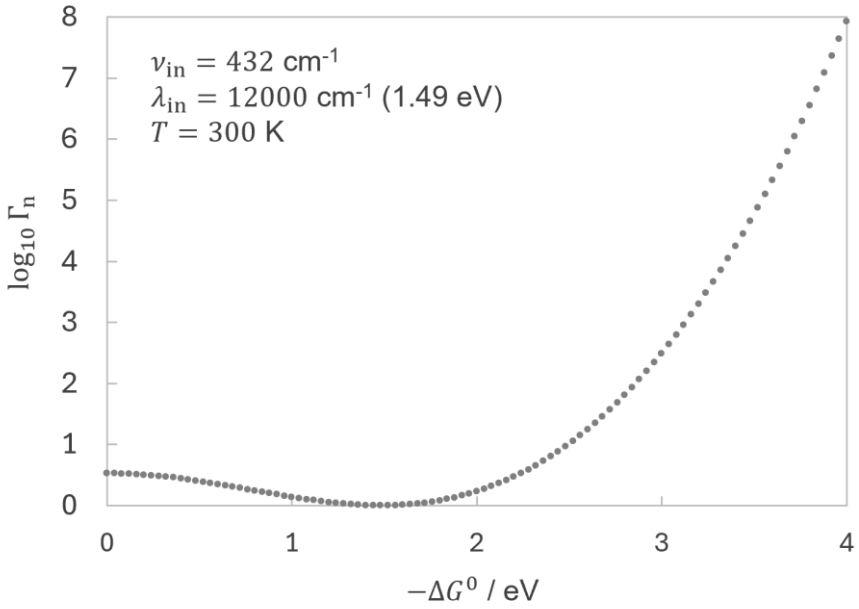

Fig. 2.7 Model tunneling behavior of Scher-Holstein method against the reaction energy from the Marcus normal to the inverted region. Tunneling factor Γ_n becomes unity, namely $\log_{10}\Gamma_n = 0$, at the top region because there is no barrier for tunneling. The plots were reproduced using the parameters given in the reference[35]. Formulars are given in chapter 4.

2.9 Rate Constant Maximization in Crossing Region

In chapters 3 and 4, the rate constants of electron transfer reactions are maximized in the crossing region along a parameter. Herein, its basic concept is explained. In the transition state theory, the dividing surface, which defines the reactant region and product region of the potential energy

surface, is defined at the first-order saddle point (transition state).[42] Then the rate constant is evaluated by the reaction barrier from the equilibrium geometry to the first-order saddle-point with eqn (1.2). This is because the reaching probability is highest at the saddle-point in the dividing surface. In this study, SX is considered as the dividing surface. The reaching probability is highest at the minimum energy seam of crossing (MESX). However, the rate constant of electron transfer is strongly affected not only by the reaction barrier, but also the nuclear tunneling effect and the electronic coupling energy as presented in eqn (2.9). Therefore, the rate constant is not always maximum at the MESX, and the maximization in the crossing region is performed.

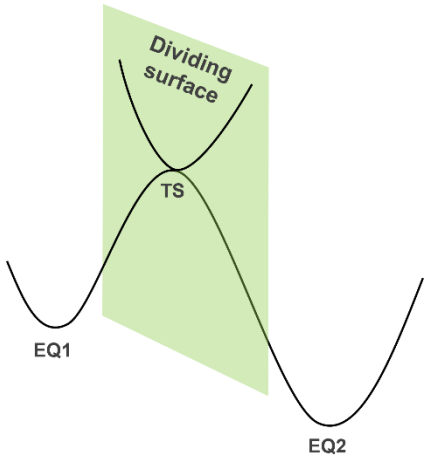

Fig. 2.8 Transition state (TS) and the dividing surface (green) on an adiabatic potential.

2.10 Energy Decomposition Analysis

In chapter 3, the activation strain model (ASM)[43–45], was employed for prevailing the details of the activation process of the electron self-exchange reactions between the transition metal complexes with charge 3+ and 2+ (Fig 2.9). The ASM decomposes the activation energy into the interaction energy between the reactant molecules and strain energies of each reactant along the reaction coordinate. The analysis details are presented in chapter 3.

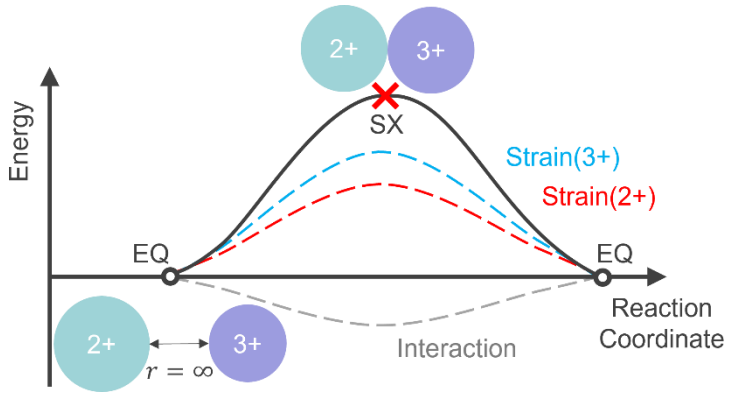

Fig. 2.9 Illustration of energy decomposition analysis along the reaction coordinate of the electron self-exchange reactions between the transition metal complexes. The shrink and expansion from left side EQ (the two complexes are infinitely distant) to SX (the two complexes are close) correspond to the deformation (shortening and stretching of coordination bond between the central metal atom and ligands) of the complexes. The grey, blue, and red dashed lines represent the energetic change of the interaction between complexes, the strain energy of the complex with charge 3+, and the strain energy of the complex with charge 2+, respectively.

In chapter 4, the breakdowns of reaction energies are presented too. In this case of radical anions, donor and acceptor are fixed on a rigid spacer structure, and the distance between donor and acceptor is constant. Therefore, the change of interaction energy is ignored, and focusing on the activation energies coming from solvent orientation change and donor-acceptor deformation.

References for Chapter 2

1 S. Maeda, K. Ohno and K. Morokuma, *Phys. Chem. Chem. Phys.*, 2013, **15**, 3683–3701.

2 S. Maeda, Y. Harabuchi, M. Takagi, K. Saita, K. Suzuki, T. Ichino, Y. Sumiya, K.

Sugiyama and Y. Ono, *J Comput Chem*, 2018, **39**, 233–251.

3 M. J. Frisch, G. W. Trucks, H. B. Schlegel, G. E. Scuseria, M. A. Robb, J. R. Cheeseman, G. Scalmani, V. Barone, G. A. Petersson, H. Nakatsuji, X. Li, M. Caricato, A. V. Marenich, J. Bloino, B. G. Janesko, R. Gomperts, B. Mennucci, H. P. Hratchian, J. V. Ortiz, A. F. Izmaylov, J. L. Sonnenberg, D. Williams-Young, F. Ding, F. Lipparini, F. Egidi, J. Goings, B. Peng, A. Petrone, T. Henderson, D. Ranasinghe, V. G. Zakrzewski, J. Gao, N. Rega, G. Zheng, W. Liang, M. Hada, M. Ehara, K. Toyota, R. Fukuda, J. Hasegawa, M. Ishida, T. Nakajima, Y. Honda, O. Kitao, H. Nakai, T. Vreven, K. Throssell, J. A. Montgomery, Jr., J. E. Peralta, F. Ogliaro, M. J. Bearpark, J. J. Heyd, E. N. Brothers, K. N. Kudin, V. N. Staroverov, T. A. Keith, R. Kobayashi, J. Normand, K. Raghavachari, A. P. Rendell, J. C. Burant, S. S. Iyengar, J. Tomasi, M. Cossi, J. M. Millam, M. Klene, C. Adamo, R. Cammi, J. W. Ochterski, R. L. Martin, K. Morokuma, O. Farkas, J. B. Foresman, and D. J. Fox, Gaussian 16, Revision C.02, Gaussian, Inc., Wallingford CT, 2019.

4 K. Ohno and S. Maeda, *Chem Phys Lett*, 2004, **384**, 277–282.

5 S. Maeda and K. Ohno, *J Phys Chem A*, 2005, **109**, 5742–5753.

6 K. Ohno and S. Maeda, *J Phys Chem A*, 2006, **110**, 8933–8941.

7 S. Maeda and Y. Harabuchi, *WIREs Computational Molecular Science*, 2021, **11**, e1538.

8 S. Maeda and K. Morokuma, *J Chem Phys*, 2010, **132**, 241102.

9 M. J. Bearpark, M. A. Robb and H. Bernhard Schlegel, *Chem Phys Lett*, 1994, **223**, 269–274.

10 S. Maeda, K. Ohno and K. Morokuma, *J Chem Theory Comput*, 2010, **6**, 1538–1545.

11 S. Maeda and K. Morokuma, *J Chem Theory Comput*, 2011, **7**, 2335–2345.

12 S. Maeda, T. Taketsugu and K. Morokuma, *J Comput Chem*, 2014, **35**, 166–173.

13 S. Maeda, Y. Harabuchi, M. Takagi, T. Taketsugu and K. Morokuma, *The Chemical Record*, 2016, **16**, 2232–2248.

14 Y. Sumiya, Y. Nagahata, T. Komatsuzaki, T. Taketsugu and S. Maeda, *J Phys Chem A*, 2015, **119**, 11641–11649.

15 Y. Sumiya and S. Maeda, *Chem Lett*, 2020, **49**, 553–564.

16 Y. Sumiya and S. Maeda, *Chem Lett*, 2019, **48**, 47–50.

17 S. Maeda, Y. Harabuchi, H. Hayashi and T. Mita, *Annu Rev Phys Chem*, 2023, **74**, 287–311.

18 Y. Harabuchi, T. Taketsugu and S. Maeda, *Chem Phys Lett*, 2017, **674**, 141–145.

19 S. Maeda, K. Ohno and K. Morokuma, *J Phys Chem A*, 2009, **113**, 1704–1710.

20 S. Maeda, T. Taketsugu, K. Ohno and K. Morokuma, *J Am Chem Soc*, 2015, **137**, 3433–3445.

21 A. Mutsuji, K. Saita and S. Maeda, *RSC Adv*, 2023, **13**, 32097–32103.

22 S. Dapprich, I. Komáromi, K. S. Byun, K. Morokuma and M. J. Frisch, *Journal of Molecular Structure: THEOCHEM*, 1999, **461–462**, 1–21.

23 L. W. Chung, W. M. C. Sameera, R. Ramozzi, A. J. Page, M. Hatanaka, G. P. Petrova, T. V Harris, X. Li, Z. Ke, F. Liu, H.-B. Li, L. Ding and K. Morokuma, *Chem Rev*, 2015, **115**, 5678–5796.

24 R. A. Marcus and N. Sutin, *Biochimica et Biophysica Acta (BBA) - Reviews on Bioenergetics*, 1985, **811**, 265–322.

25 V. Barone and M. Cossi, *J Phys Chem A*, 1998, **102**, 1995–2001.

26 M. Cossi, N. Rega, G. Scalmani and V. Barone, *J Comput Chem*, 2003, **24**, 669–681.

27 J. M. Herbert, *WIREs Computational Molecular Science*, 2021, **11**, e1519.

28 N. Amenta, S. Levy, T. Munzner and M. Phillips, in *Proceedings of the Eleventh Annual Symposium on Computational Geometry*, Association for Computing Machinery, New York, NY, USA, 1995, pp. 412–413.

29 R. Improta, G. Scalmani, M. J. Frisch and V. Barone, *J Chem Phys*, 2007, **127**, 74504.

30 M. Cossi and V. Barone, *J Chem Phys*, 2000, **112**, 2427–2435.

31 M. Hatanaka and K. Morokuma, *J Chem Theory Comput*, 2014, **10**, 4184–4188.

32 Y. Harabuchi, M. Hatanaka and S. Maeda, *Chem Phys Lett*, 2019, **737**, 100007.

33 Y. Harabuchi, H. Hayashi, H. Takano, T. Mita and S. Maeda, *Angewandte Chemie International Edition*, 2023, **62**, e202211936.

34 H. Scher and T. Holstein, *Philosophical Magazine B*, 1981, **44**, 343–356.

35 N. Sutin, in *Progress in Inorganic Chemistry*, John Wiley & Sons, Ltd, 1983, pp. 441–498.

36 T. Holstein, *Ann Phys (N Y)*, 1959, **8**, 325–342.

37 T. Holstein, *Ann Phys (N Y)*, 1959, **8**, 343–389.

38 T. Holstein, *Philosophical Magazine B*, 1978, **37**, 49–62.

39 T. Holstein, *Philosophical Magazine B*, 1978, **37**, 499–526.

40 B. S. Brunschwig, J. Logan, M. D. Newton and N. Sutin, *J Am Chem Soc*, 1980, **102**, 5798–5809.

41 D. K. Phelps and M. J. Weaver, *J Phys Chem*, 1992, **96**, 7187–7193.

42 P. Hänggi, P. Talkner and M. Borkovec, *Rev Mod Phys*, 1990, **62**, 251–341.

43 F. M. Bickelhaupt, *J Comput Chem*, 1999, **20**, 114–128.

44 L. P. Wolters and F. M. Bickelhaupt, *WIREs Computational Molecular Science*, 2015, **5**, 324–343.

45 F. M. Bickelhaupt and K. N. Houk, *Angewandte Chemie International Edition*, 2017, **56**, 10070–10086.

Chapter 3

The EDEEL method for intermolecular electron transfer: a case study of electron self-exchange reactions between transition metal complexes

3.1 Introduction

Electron transfer (ET) plays a fundamental role in various chemical systems, including artificial photosynthesis, photocatalysis, electrocatalysis, and electronic devices.[1–6] Theoretical tools are needed to elucidate and design novel reactivities and functions triggered by ET.[7–10] The ET rate constant is given by eqn (3.1).[9, 11–12]

$$k_{\mathrm{ET}} = \left(\frac{RT}{p^0}\right)^q \kappa_{\mathrm{el}} \nu_{\mathrm{n}} \exp\left(-\frac{\Delta G^{\ddagger}}{RT}\right) \tag{3.1}$$

Where R is the gas constant, T is the temperature, p^0 is the standard atmosphere, q is either 1 or 0 for intermolecular or intramolecular ET, κ_{el} is the electronic transmission coefficient, ν_{n} is an effective nuclear frequency along the reaction coordinate, and $\Delta G^{\ddagger}$ is the Gibbs energy of activation on the adiabatic potential energy surface (PES). κ_{el} is given by eqn (3.2)-(3.4).

$$\kappa_{\mathrm{el}} = \begin{cases} \dfrac{2P_{\mathrm{LZ}}}{1+P_{\mathrm{LZ}}} \ (\text{If } \Delta G^0 \geq -\lambda) \\ 2P_{\mathrm{LZ}}(1-P_{\mathrm{LZ}}) \ (\text{If } \Delta G^0 < -\lambda) \end{cases} \tag{3.2}$$

$$P_{\mathrm{LZ}} = 1 - \exp(-2\pi\gamma) \tag{3.3}$$

$$2\pi\gamma = \frac{\pi^{3/2}|V_{12}|^2}{h\nu_{\mathrm{n}}\sqrt{\lambda k_B T}} \tag{3.4}$$

Where P_{LZ} is the Landau-Zener transition probability, k_{B} is the Boltzmann constant, h is the Planck constant, V_{12} is the coupling constant, and λ is the reorganization energy (Fig. 3.1). When

V_{12} is relatively small and $2\pi\gamma << 1$, the Marcus theory equation[13] eqn (3.5) is obtained from Taylor series of eqn (3.3).

$$k_{\mathrm{ET}} = \left(\frac{RT}{p^0}\right)^q \frac{2|V_{12}|^2}{h}\left(\frac{\pi^3}{\lambda k_B T}\right)^{1/2} \exp\left(-\frac{\Delta G^{\ddagger}_{\mathrm{na}}}{RT}\right) \tag{3.5}$$

The harmonic approximation is often used to describe the diabatic PESs of the initial and final states, which allows one to estimate the Gibbs energy of activation $\Delta G_{\mathrm{na}}^{\ddagger}$ (subscript "na" means "non-adiabatic") by the following eqn (3.6) without explicitly locating the intersection between the two diabatic PESs on the multidimensional coordinate space. Note that the reaction barrier in eqn (3.1) is $\Delta G^{\ddagger}$, not $\Delta G^{\ddagger}_{\mathrm{na}}$ (Fig. 1).

$$\Delta G^{\ddagger}_{\mathrm{na}} = \frac{(\lambda + \Delta G^0)^2}{4\lambda} \tag{3.6}$$

Since the diabatization required to obtain the diabatic PESs and their coupling V_{12} is not unique, different approaches have been proposed depending on the purpose.[14–23] For example, the generalized Mulliken-Hush (GMH) theory is for ET and generates diabatic states based on the assumption that the initial and final diabatic states are charge-localized states at different centers of the donor and acceptor.[24,25] Constrained density functional theory (CDFT) is also useful for ET and forms diabatic states by imposing constraints on the partial charge (or spin) of arbitrary molecules or fragments using the Lagrange multiplier.[26,27]

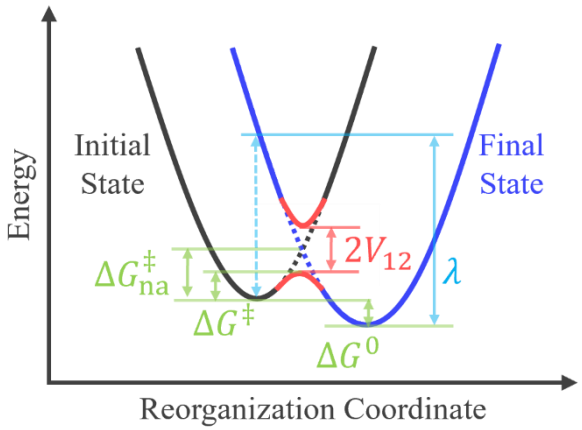

Fig. 3.1 Crossing of two diabatic potential energy surfaces and the relations among V_{12}, λ, ΔG^0, $\Delta G^{\ddagger}$, and $\Delta G_{na}{}^{\ddagger}$ in the rate constant expressions.

To go beyond the framework based on the harmonic approximation, it is necessary to consider the anharmonic effect on the reaction coordinate. This requires explicit evaluations of PESs at around the non-adiabatic transition takes place. Molecular dynamics simulations can be performed to obtain accurate transition probabilities by calculating a large number of trajectories passing through such a region.[9,28–31] A computationally less demanding alternative approach is to identify the seam-of-crossing (SX) or conical intersection (CI) geometry within the full-dimensional coordinate space.[32–38] Simulations of non-adiabatic events based on SX or CI geometries have become increasingly common in recent years.[39–45] In this approach, $\Delta G_{na}{}^{\ddagger}$ is estimated as the energy gap between the SX/CI geometry and the initial state equilibrium (EQ) geometry.

This study presents a semi-quantitative yet efficient algorithm for predicting the ET rate constant based eqn (3.1)-(3.4) rather than eqn (3.5) because the present scheme tends to give relatively large coupling values as discussed in Results and Discussion. The present method

directly identifies the SX geometry. A simple diabatization based on energy decomposition and extrapolation schemes[46–48] allows one to optimize an SX geometry and evaluate $\Delta G^{\ddagger}$, $\Delta G_{na}^{\ddagger}$, V_{12}, and λ. Rate constants for thirteen electron self-exchange reactions were calculated and compared with experimental[49–59] and calculated[60–66] values reported in the literature to investigate the performance of the present method. The calculated rate constants showed a good correlation with the experimental values. The energy decomposition scheme provided interpretations of the factors determining the magnitudes of the ET rate constants based on the activation strain model (ASM).[67–69]

3.2 Method

In this study, a simple diabatization scheme called energy decomposition and extrapolation-based electron localization (EDEEL) is proposed. In EDEEL, the diabatic energies for the initial and final states V_{11} and V_{22} are given by eqn (3.7) and (3.8), respectively.

$$V_{11}(\mathbf{R}) = E_{n+m}^{\mathrm{C}}(\mathbf{R}) - E_{n}^{\mathrm{D}}(\mathbf{R}^{\mathrm{D}}) + E_{n+1}^{\mathrm{D}}(\mathbf{R}^{\mathbf{D}}) \tag{3.7}$$

$$V_{22}(\mathbf{R}) = E_{n+m}^{\mathrm{C}}(\mathbf{R}) - E_{m}^{\mathrm{A}}(\mathbf{R}^{\mathbf{A}}) + E_{m+1}^{\mathrm{A}}(\mathbf{R}^{\mathbf{A}}) \tag{3.8}$$

Where $\mathbf{R}$ is the geometry of the donor-acceptor complex system, and $\mathbf{R}^{\mathrm{D}}$ and $\mathbf{R}^{\mathrm{A}}$ are its donor and acceptor components, respectively. The subscript for each E corresponds to the number of electrons in the corresponding system ($n = m$ in the electron self-exchange reactions). $E_{n+m}^{\mathrm{C}}(\mathbf{R})$ is the adiabatic energy of the donor-acceptor complex without the moving electron. $E_{n}^{\mathrm{D}}(\mathbf{R})$ and $E_{n+1}^{\mathrm{D}}(\mathbf{R})$ are the adiabatic energies of the donor species without and with the moving electron, respectively. $E_{m}^{\mathrm{A}}(\mathbf{R})$ and $E_{m+1}^{\mathrm{A}}(\mathbf{R})$ are the adiabatic energies of the acceptor species without and with the moving electron, respectively. This scheme assumes that the moving electron is

localized on either the donor or acceptor species and does not interact with the corresponding counterpart. In other words, this scheme sets these assumptions as the conditions for diabatization. In the EDEEL scheme, an SX geometry between V_{11} and V_{22} is the critical point at which k_{ET} is evaluated.

$\Delta G^{\ddagger}_{\mathrm{na}}(= G_{\mathrm{SX}} - G_{\mathrm{Initial-EQ}})$ is the Gibbs energy gap between the SX and the initial state EQ geometries. Gibbs energy corrections at the EQ and SX are calculated by the normal mode analysis. The coupling V_{12} is computed as the energy difference $V_{12} = V_{11} - E^{\mathrm{C}}_{n+m+1}$, where E^{C}_{n+m+1} is the lower adiabatic energy between those for the two states that contain the contributions of the two diabatic states the most. Thus, at the SX between V_{11} and V_{22}, i.e., when $V_{11} = V_{22}$, the EDEEL scheme reproduces the diabatic-adiabatic relation of the two-state model in eqn (3.9).

$$E^{\mathrm{C}}_{n+m+1} = \frac{1}{2}(V_{11} + V_{22}) - \frac{1}{2}\sqrt{(V_{11} - V_{22})^2 + 4V_{12}^2} \tag{3.9}$$

In the electron self-exchange reactions, E^{C}_{n+m+1} is the adiabatic energy of the donor-acceptor complex in its electronic ground state. The parameter λ is obtained as eqn (3.10) based on eqn (3.6).

$$\lambda = 2G_{\mathrm{SX}} - G_{\mathrm{Initial-EQ}} - G_{\mathrm{Final-EQ}} + 2\sqrt{\left(G_{\mathrm{SX}} - G_{\mathrm{Initial-EQ}}\right)\left(G_{\mathrm{SX}} - G_{\mathrm{Final-EQ}}\right)} \tag{3.10}$$

Where relations $\Delta G^{\ddagger}_{\mathrm{na}} = G_{\mathrm{SX}} - G_{\mathrm{Initial-EQ}}$ and $\Delta G^{0} = G_{\mathrm{Final-EQ}} - G_{\mathrm{Initial-EQ}}$ are used, $G_{\mathrm{Final-EQ}}$ is Gibbs energy of the final state EQ, and eqn (3.6) gives $\lambda = 4\Delta G^{\ddagger}_{\mathrm{na}}$ for electron self-exchange reactions.[70]

The distance dependence of the ET reaction rate may have a distinct peak.[60] This study regards adiabatic ground state at the SX geometry between V_{11} and V_{22} as the approximate transition state and maximizes the ET rate constant k_{ET} within the SX region to obtain the final

k_{ET} (= k_{calc}). This is done by taking the donor-acceptor distance r_{DA} (the metal-metal distance in the transition metal examples below) as the reaction coordinate, evaluating the k_{ET} at various r_{DA}, and maximizing the k_{ET} along r_{DA}. Details of how the initial r_{DA}(ini) is systematically determined and how the k_{ET} is maximized are described in the Supplementary Material.

As shown in Fig. 2, the entire k_{calc} evaluation workflow consists of the following four steps.

1. Systematic search for monomer conformations using the SC-AFIR[71,72] method implemented in the Global Reaction Route Mapping (GRRM) program.[73]

2. Optimization of a minimum energy SX (MESX) geometry[74,75] within the SX hypersurface between V_{11} and V_{22} while maintaining the donor-acceptor distance to r_{DA}(ini).

3. k_{ET} maximization along r_{DA} by calculating k_{ET} for five r_{DA} values near r_{DA}(ini), where line search is done by simple quadratic curve fitting using three k_{ET} values in this study. In the calculation of k_{ET} with eqn (3.1)-(3.4), the Gibbs energies are extrapolated by the electronic energies obtained from single point calculations with larger basis set.

4. ASM analysis at the geometry of the largest k_{ET} (= k_{calc}) obtained in step 3 (optional).

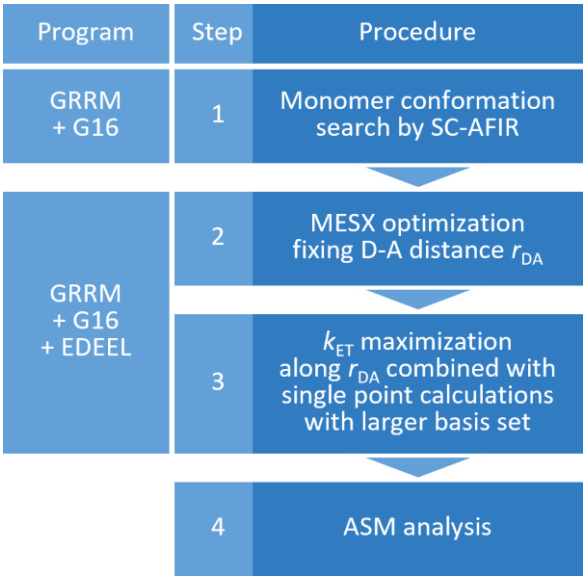

Fig. 3.2 The entire workflow for obtaining an electron transfer rate constant by EDEEL and the calculation programs used in each procedure.

3.3 Results and Discussion

The workflow in Fig. 3.2 was applied to the electron self-exchange reactions of thirteen transition metal complexes listed in Table 3.1. Electronic structure calculations were performed with the Gaussian16 program[76] and geometry optimization was performed with the GRRM program at the UωB97X-D/Def2-SV(P)[77,78] level taking into account the solvent effect of water by the conductor-like polarizable continuum model (C-PCM).[79,80], where UωB97X-D stands for a spin unrestricted DFT calculation using the ωB97X-D functional. k_{ET} was maximized using the electronic energy calculated at the UωB97X-D/Def2-TZVP[81] level and the Gibbs energy correction at the UωB97X-D/Def2-SV(P) level; the calculation level is represented as UωB97X-D/Def2-TZVP//Def2-SV(P). In the calculation of k_{ET}, ν_n in eqn (1) was approximated as $k_B T/h$, the coefficient of transition state theory rate constant equation. The spin multiplicity was chosen to stabilize each state as much as possible and was set to the values listed in Table 3.1. The reaction

set in Table 3.1 covers reactions of different timescales with rate constants in the wide range of 10^{-7} to 10^{9} dm^3 mol^{-1} s^{-1}, and thus would be suitable as a test set. It was assumed that both 3+ and 2+ charged complexes were in the electronic ground state at SX, although there were possibilities for ET via metal-to-ligand-charge transfer (MLCT) or electronic excited states of each complex.[82] Further computational details are presented in Computational Section.

Table 3.1 Spin multiplicity used in the calculations, experimental rate constants k_{expt} of the thirteen electron self-exchange reactions of transition metal complexes, and their data sources.

Redox couple	Spin multiplicity (3+/2+)	Experimental Values		Reference
		k_{expt} / dm^3 mol^{-1} s^{-1}	$\log_{10}k_{expt}$	
$[V(H_2O)_6]^{3+/2+}$	3/4	3×10^{-3}, 1×10^{-2}	−2.0	49,50
$[Cr(H_2O)_6]^{3+/2+}$	4/5	$< 2 \times 10^{-5}$	−4.7	51
$[Fe(H_2O)_6]^{3+/2+}$	6/5	1.1	0.0	51
$[Co(H_2O)_6]^{3+/2+}$	5/4	5	0.7	49,52
$[Ru(H_2O)_6]^{3+/2+}$	2/1	$(6 \pm 4) \times 10^{1}$	1.8	53
$[Co(NH_3)_6]^{3+/2+}$	1/4	$>10^{-7}$	−7.0	51
$[Ru(NH_3)_6]^{3+/2+}$	2/1	4.3×10^{3}	3.6	49,54
$[Ru(NH_3)_5py]^{3+/2+}$	2/1	4.7×10^{5}	5.7	55
$[Co(en)_3]^{3+/2+}$	1/4	7.7×10^{-5}	−4.1	56

$[Ru(en)_3]^{3+/2+}$	2/1	2.8×10^4	4.4	51
$[Fe(bpy)_3]^{3+/2+}$	2/1	3×10^8	8.5	57,58
$[Co(bpy)_3]^{3+/2+}$	1/4 (1/2) [a]	18	1.3	51
$[Ru(bpy)_3]^{3+/2+}$	2/1	1.2×10^9	9.1	59

[a] Values for monomer and SX are shown outside and inside the parentheses, respectively.

Table 3.2 lists the $\log_{10}k_{calc}$, $\Delta G^{\ddagger}$, λ, V_{12}, κ_{el}, and r_{DA} values obtained by the present calculations at the UωB97X-D/Def2-TZVP//Def2-SV(P) level. Fig. 3.3 shows the correlation between the calculated $\log_{10}k_{calc}$ and the experimental $\log_{10}k_{expt}$,[49–59] and that the present calculation reproduces the experimental trend well. Fig. 3.3 also compares the $\log_{10}k_{calc}$ values with those obtained by the other theoretical methods.[60–66] Despite the simplicity of the algorithm, which does not include a complex diabatization scheme or any empirical factors, the present method provides an accuracy comparable to the other theoretical methods, making EDEEL promising for the semi-quantitative estimation of ET rate constants.

Table 3.2 $\log_{10}k_{calc}$, Gibbs energies of activation $\Delta G^{\ddagger}$, reorganization energy λ, diabatic coupling V_{12}, electronic transmission coefficient κ_{el}, and donor-acceptor distance r_{DA} by EDEEL at the UωB97X-D/Def2-TZVP//Def2-SV(P) level.

Redox couple	$\log_{10}k_{calc}$	$\Delta G^{\ddagger}$ / eV	λ / eV	V_{12} / eV	κ_{el}	r_{DA} / Å
$[V(H_2O)_6]^{3+/2+}$	1.1	0.77	4.02	0.23	1.00	5.76

$[Cr(H_2O)_6]^{3+/2+}$	-4.3	1.09	5.45	0.27	1.00	5.74
$[Fe(H_2O)_6]^{3+/2+}$	0.2	0.83	4.29	0.24	1.00	5.72
$[Co(H_2O)_6]^{3+/2+}$	1.0	0.78	4.10	0.24	1.00	5.53
$[Ru(H_2O)_6]^{3+/2+}$	1.1	0.77	4.01	0.23	1.00	5.78
$[Co(NH_3)_6]^{3+/2+}$	-6.9	1.25	5.26	0.07	0.96	7.68
$[Ru(NH_3)_6]^{3+/2+}$	6.9	0.43	2.01	0.07	0.99	7.39
$[Ru(NH_3)_5py]^{3+/2+}$	8.6	0.33	1.65	0.08	1.00	9.51
$[Co(en)_3]^{3+/2+}$	-5.5	1.16	4.86	0.05	0.91	7.96
$[Ru(en)_3]^{3+/2+}$	7.1	0.42	1.90	0.06	0.98	8.02
$[Fe(bpy)_3]^{3+/2+}$	11.9	0.08	0.87	0.13	1.00	9.08
$[Co(bpy)_3]^{3+/2+}$	2.2	0.71	3.24	0.10	1.00	8.75
$[Ru(bpy)_3]^{3+/2+}$	11.8	0.14	0.97	0.10	1.00	8.91

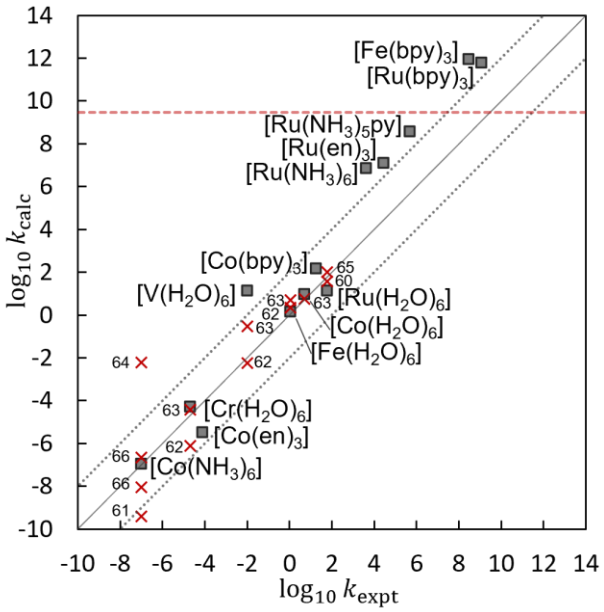

Fig. 3.3 A correlation between experimental $\log_{10}k_{\mathrm{expt}}$ and calculated $\log_{10}k_{\mathrm{calc}}$ by EDEEL at the UωB97X-D/Def2-TZVP//Def2-SV(P) level (filled squares) or by the other method[60-66] (red crosses). The red dotted line represents the diffusion-controlled rate constant.[49]

In Table 3.2, the coupling values are relatively large, making κ_{el} almost unity. This is because the present diabatization constraint assumes that there is no interaction between the electron to be transferred and the acceptor molecule. In other words, present constraint pushes the strong attraction between the negative charge on the moving electron and the 3+ positive charge on the acceptor molecule into the coupling value, making the coupling values large. As for the non-adiabaticity, electron transfer reactions in $[M(H_2O)_6]^{3+/2+}$, which showed the largest coupling values among the systems in the present calculation, are known as non-adiabatic process with smaller actual coupling values (< 100 cm^{-1}).[83] The $\log_{10}k_{\mathrm{calc}}$ does not include the diffusion-controlled rate constant, which is estimated to be $k_{\mathrm{diff}} = 3 \times 10^9$ dm^3 mol^{-1} s^{-1} for these reactions.[49] In other words, k_{diff} would be a source of the large error seen for fast reactions such as $[Fe(bpy)_3]^{3+/2+}$ and $[Ru(bpy)_3]^{3+/2+}$. In the present scheme, the C-PCM environments of the initial

and final states are relaxed independently, which does not satisfy the Franck-Condon principle. This would have led to the underestimation of reaction barriers. For example, the outer-sphere reorganization energy of $[Ru(H_2O)_6]^{3+/2+}$ was estimated to be 0.68 eV based on dielectric continuum theory.[13] This implies additional reaction barrier of 0.17 eV, reducing its $\log_{10}k_{ET}$ from 1.1 to -1.7, which is three-order of magnitude smaller than the experimental value. The simple addition of the outer-sphere reorganization energy correction is not sufficient in the present scheme. The better treatment of outer-sphere reorganization in the present scheme needs further study in the future. Many other factors such as explicit solvation, dynamic and quantum motion of the atoms, and higher order (or static) electron correlation would contribute to the error. However, further improvement of the accuracy considering these factors is beyond the scope of this study.

Thanks to the energy decomposition and extrapolation scheme of EDEEL, the ASM analysis[67–69] can be performed using the energy components, i.e., E_{n+m}^{C}, E_{n}^{D}, E_{n+1}^{D}, E_{m}^{A}, and E_{m+1}^{A}, calculated during the EDEEL calculations, without any additional calculations. Note that the ASM analysis was performed using electronic energies rather than Gibbs energies for the SX geometry with the highest k_{ET} value. In the ASM/EDEEL analysis, the strain energies in donor $\Delta E_{\mathrm{Strain(D)}}^{\ddagger}$ and acceptor $\Delta E_{\mathrm{Strain(A)}}^{\ddagger}$ and their interaction energy $\Delta E_{\mathrm{Interaction(C)}}^{\ddagger}$ are represented as follows.

$$\Delta E_{\mathrm{Strain(D)}}^{\ddagger} = E_{n+1}^{\mathrm{D(SX)}} - E_{n+1}^{\mathrm{D(Initial-EQ)}} \tag{3.11}$$

$$\Delta E_{\mathrm{Strain(A)}}^{\ddagger} = E_{m}^{\mathrm{A(SX)}} - E_{m}^{\mathrm{A(Initial-EQ)}} \tag{3.12}$$

$$\Delta E_{\mathrm{Interaction(C)}}^{\ddagger} = E_{n+m}^{\mathrm{C(SX)}} - E_{n}^{\mathrm{D(SX)}} - E_{m}^{\mathrm{A(SX)}} \tag{3.13}$$

Where $E_{n+1}^{\mathrm{D(SX)}}$, $E_{n}^{\mathrm{D(SX)}}$, $E_{m}^{\mathrm{A(SX)}}$ and $E_{n+m}^{\mathrm{C(SX)}}$ are the electronic energies at the SX geometry of

the donor with the moving electron, that of the donor without the moving electron, that of the acceptor without the moving electron, and that of the donor-acceptor complex without the moving electron, and $E_{n+1}^{\mathrm{D(Initial-EQ)}}$ and $E_{m}^{\mathrm{A(Initial-EQ)}}$ are the electronic energies at the initial state EQ geometry of the donor with the moving electron and of the acceptor without the moving electron. The donor and acceptor in the initial EQ geometry are assumed to be infinitely far apart and not interacting. Fig. 3.4 and 3.5 show the results of the ASM/EDEEL analysis at the UωB97X-D/Def2-TZVP level. The magnitudes of the strain energies of the aqua and cobalt complexes are large as shown in Fig. 3.4, reflecting the large oxidation/redox potentials of their 2+/3+ species. In these systems, to compensate for the large energy gaps between the 2+ and 3+ species, large structural deformations ($\Delta l_{\mathrm{Strain(D)}}^{\ddagger}$ and $\Delta l_{\mathrm{Strain(A)}}^{\ddagger}$, changes in mean coordination bond length in donor and acceptor, respectively) are seen in the SXs around their central metal, as shown in Fig. 3.5. From another perspective, among the complexes of the same ligands, the complexes with chromium and cobalt centers required large deformation during the activation process. In these complexes, one transferring electron moves into the e_g antibonding orbital of the acceptor, causing the large elongation of coordinate bond.[63] In pyridine and bipyridine complexes, attractive interactions are seen due to π-stacking between pyridine moieties and π-stacking between bipyridine molecules, respectively.[13,49] On the other hand, aqua, ammonia, and ethylenediamine complexes show repulsive interactions, even though aqua complexes formed hydrogen bonding between water molecules. These interpretations by ASM/EDEEL would be beneficial in understanding ET rate constants quantitatively.

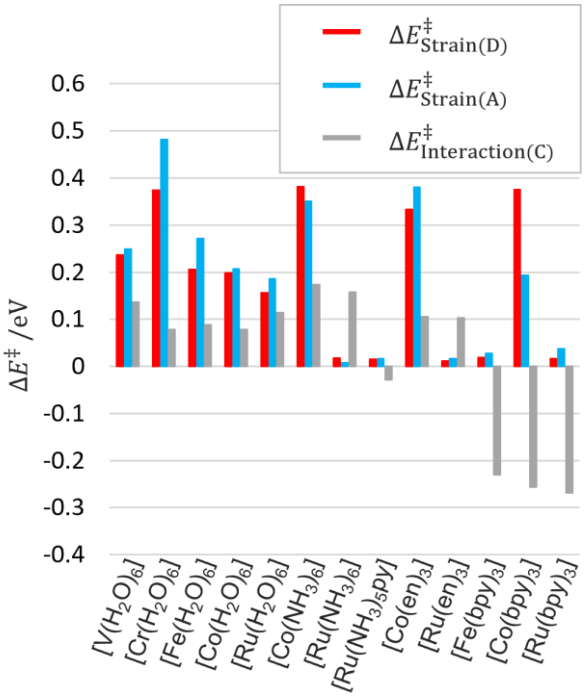

Fig. 3.4 Strain energies and interaction energies by ASM analysis at UωB97X-D/Def2-TZVP.

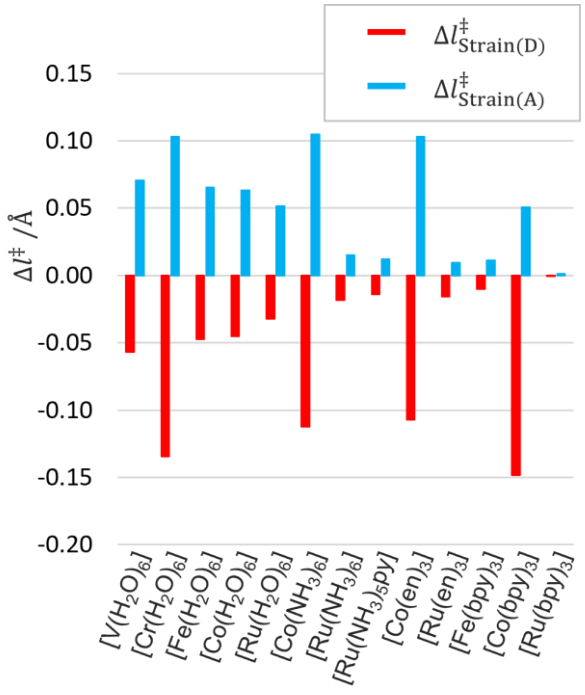

Fig. 3.5 Changes in mean coordination bond length.

3.4 Conclusion

In this article, I have proposed a simple diabatization scheme called EDEEL for the analysis of ET reactions. EDEEL represents the diabatic energies, V_{11} and V_{22}, by combining the adiabatic energies of the donor, acceptor, and their complex. Such a simple representation allows us to easily optimize the SX geometries between the two diabatic potentials. A scheme for estimating the ET rate constants at the SX geometries has also been introduced. The diabatic coupling V_{12} is also estimated by using the adiabatic energy of the donor-acceptor complex. In other words, the present scheme allows one to obtain all the parameters necessary to estimate ET rate constants using only the adiabatic energies. Numerical tests with electron self-exchange reactions of thirteen transition metal complexes have shown that EDEEL reproduces the trend of the experimental rate constants well and is semi-quantitative.

Two advantages of using EDEEL can be suggested. One is that EDEEL can be combined with any *ab initio* method and program without touching their codes. This is because all diabatic potential elements, i.e., V_{11}, V_{22} and V_{12}, are represented by the adiabatic energies. The other is that EDEEL provides all the energy components and SX geometries needed in the ASM analysis. The latter is helpful in interpreting the ET efficiency and further designing a system with higher ET efficiency. In the present applications, the EDEEL-based ASM analysis successfully provided rational explanations for the variation of the magnitudes of the ET rate constants depending on the transition metal complexes.

3.5 Computational Section

The above procedures were implemented in an in-house Python script as an interface program between the GRRM program and the Gaussian16 program.[73,76] The script takes a geometry from GRRM, performs the necessary electronic structure calculations to obtain the EDEEL PES at the geometry using Gaussian 16, and returns the energy and gradient (and Hessian if necessary) of the EDEEL PES at the geometry to GRRM. Geometry optimizations were performed by a developer version of the GRRM program at the UωB97X-D/Def2-SV(P) level. The "Stable=Opt" option was also used to identify the electronic ground state configuration of a given spin multiplicity. The "Int(Grid=99590)" option was used in DFT calculations. Although some of the aqua-complexes are highly acidic and may not prevail as simple $[M(H_2O)_6]^{3+/2+}$ complexes in actual aqueous solution, the metal centers were assumed to be hexa-coordinated in this study as previous reports.[60,62,63,65] Solvent water was modeled by the conductor-like polarizable continuum model (C-PCM).[79,80] Gibbs energy corrections were obtained from the standard normal mode analysis of $3N-8$ dimensions (one direction orthogonal to SX and one direction along the vector between two metal atoms were removed from the full $3N-6$ dimensions) at $T = 298.15$ K and $p^0 = 1$ atm, with normal mode frequencies smaller than 100 cm^{-1} replaced by 100 cm^{-1} as suggested in the literature.[84] The bases of Gibbs activation energies were calculated as the sum of the extrapolated Gibbs energies of the most stable donor and acceptor monomers, where the most stable structures were identified by a systematic conformation search using SC-AFIR with possible spin multiplicities. An entropy correction −4.3 kcal/mol was added to the Gibbs energy of the dimer complex in the activation energy calculation to account for the restriction of their mobility in the water solvent, following the previous studies.[85–87] The rate constant maximization was done at the UωB97X-D/Def2-TZVP//Def2-SV(P) level.

References for Chapter 3

1 D. Gust, T. A. Moore and A. L. Moore, *Acc. Chem. Res.*, 2009, **42**, 1890.

2 M. H. Shaw, J. Twilton and D. W. C. MacMillan, *J. Org. Chem.*, 2016, **81**, 6898.

3 N. A. Romero and D. A. Nicewicz, *Chem. Rev.*, 2016, **116**, 10075.

4 N. T. Suen, S. F. Hung, Q. Quan, N. Zhang, Y. J. Xu and H. M. Chen, *Chem. Soc. Rev.*, 2017, **46**, 337.

5 K. Tvrdy, P. A. Frantsuzov and P. V. Kamat, *Proc. Natl. Acad. Sci. USA*, 2010, **108**, 29.

6 A. Hagfeldt, G. Boschloo, L. Sun, L. Kloo and H. Pettersson, *Chem. Rev.*, 2010, **110**, 6595.

7 N. Sutin, *Prog. Inorg. Chem.*, 1983, **30**, 441.

8 R. Borrelli and A. Peluso, *WIREs Comput. Mol. Sci.*, 2013, **3**, 542.

9 J. Blumberger, *Chem. Rev.*, 2015, **115**, 11191.

10 S. Fletcher, *J. Solid State Electrochem.*, 2010, **14**, 705.

11 M. D. Newton and N. Sutin, *Ann. Rev. Phys. Chem.*, 1984, **35**, 437.

12 J. C. Tully, *J. Chem. Phys.*, 2012, **137**, 22A301.

13 R. A. Marcus and N. Sutin, *Biochim. Biophys. Acta*, 1985, **811**, 265.

14 C. A. Mead and D. G. Truhlar, *J. Chem. Phys.*, 1982, **77**, 6090.

15 C. E. Hoyer, X. Xu, D. Ma, L. Gagliardi and D. G. Truhlar, *J. Chem. Phys.*, 2014, **141**, 114104.

16 C. E. Hoyer, K. Parker, L. Gagliardi and D. G. Truhlar, *J. Chem. Phys.*, 2016, **144**, 194101.

17 H. Nakamura and D. G. Truhlar, *J. Chem. Phys.*, 2001, **115**, 10353.

18 H. Nakamura and D. G. Truhlar, *J. Chem. Phys.*, 2002, **117**, 5576.

19 T. Lenzen and U. Manthe, *J. Chem. Phys.*, 2017, **147**, 084105.

20 D. M. G. Williams, A. Viel and W. Eisfeld, *J. Chem. Phys.*, 2019, **151**, 164118.

21 D. M. G. Williams and W. Eisfeld, *J. Chem. Phys.*, 2018, **149**, 204106.

22 Y. Shu and D. G. Truhlar, *J. Chem. Theory Comput.*, 2020, **16**, 6456.

23 Y. Shu, Z. Varga, A. G. S. de O. Filho and D. G. Truhlar, *J. Chem. Theory Comput.*, 2021, **17**, 1106.

24 R. J. Cave and M. D. Newton, *Chem. Phys. Lett.*, 1996, **249**, 15.

25 R. J. Cave and M. D. Newton, *J. Chem. Phys.*, 1997, **106**, 9213.

26 B. Kaduk, T. Kowalczyk and T. V. Voorhis, *Chem. Rev.*, 2012, **112**, 321.

27 F. Ding, H. Wang, Q. Wu, T. V. Voorhis, S. Chen and J. P. Konopelski, *J. Phys. Chem. A*, 2010, **114**, 6039.

28 J. C. Tully, *J. Chem. Phys.*, 1990, **93**, 1061.

29 A. V. Akimov, A. J. Neukirch and O. V. Prezhdo, *Chem. Rev.*, 2013, **113**, 4496.

30 Z. Futera, K. Sodeyama, J. V. Burda, Y. Einaga and Y. Tateyama, *Phys. Chem. Chem. Phys.*, 2014, **16**, 19530.

31 H. Nakano and H. Sato, *J. Chem. Phys.*, 2017, **146**, 154101.

32 N. Koga and K. Morokuma, *Chem. Phys. Lett.*, 1985, **119**, 371.

33 M. R. Manaa and D. R. Yarkony, *J. Chem. Phys.*, 1993, **99**, 5251.

34 F. Bernardi, M. Olivucci and M. A. Robb, *Chem. Soc. Rev.*, 1996, **25**, 321.

35 R. Poli and J. N. Harvey, *Chem. Soc. Rev.*, 2003, **32**, 1.

36 B. G. Levine and T. J. Martínez, *Annu. Rev. Phys. Chem.*, 2007, **58**, 613.

37 D. R. Yarkony, *Chem. Rev.*, 2012, **112**, 481.

38 J. N. Harvey, *WIREs Comput. Mol. Sci.*, 2014, **4**, 1.

39 S. Maeda, T. Taketsugu, K. Ohno and K. Morokuma, *J. Am. Chem. Soc.*, 2015, **137**, 3433.

40 Y. Harabuchi, T. Taketsugu and S. Maeda, *Phys. Chem. Chem. Phys.*, 2015, **17**, 22561.

41 M. Hatanaka, Y. Hirai, Y. Kitagawa, T. Nakanishi, Y. Hasegawa and K. Morokuma, *Chem. Sci.*, 2017, **8**, 423.

42 N. Aizawa, Y. Harabuchi, S. Maeda and Y. J. Pu, *Nat. Commun.*, 2020, **11**, 3909.

43 S. Suzuki, S. Sasaki, A. S. Sairi, R. Iwai, B. Z. Tang and G. Konishi, *Angew. Chem. Int. Ed.*, 2020, **59**, 9856.

44 E. Pieri, D. Lahana, A. M. Chang, C. R. Aldaz, K. C. Thompson and T. J. Martínez, *Chem. Sci.*, 2021, **12**, 7294.

45 Y. Harabuchi, H. Hayashi, H. Takano, T. Mita and S. Maeda, *Angew. Chem. Int. Ed.*, 2023, **62**, e202211936.

46 F. Maseras and K. Morokuma, *J. Comput. Chem.*, 1995, **16**, 1170.

47 L. W. Chung, H. Hirao, X. Li and K. Morokuma, *WIREs Comput. Mol. Sci.*, 2012, **2**, 327.

48 L. W. Chung, W. M. C. Sameera, R. Ramozzi, A. J. Page, M. Hatanaka, G. P. Petrova, T.

V. Harris, X. Li, Z. Ke, F. Liu, H. B. Li, L. Ding and K. Morokuma, *Chem. Rev.*, 2015, **115**, 5678.

49 M. Chou, C. Creutz and N. Sutin, *J. Am. Chem. Soc.*, 1977, **99**, 5615.

50 K. V. Krishnamurty and A. C. Waiil, *J. Am. Chem. Soc.*, 1958, **80**, 5921.

51 B. S. Brunschwig, C. Creutz, D. H. Macartney, T. K. Sham and N. Sutin, *Faraday Discuss. Chem. Soc.*, 1982, **74**, 113.

52 N. A. Bonner and J. P. Hunt, *J. Am. Chem. Soc.*, 1960, **82**, 3826.

53 W. Bottcher, G. M. Brown and N. Sutin, *Inorg. Chem.*, 1979, **18**, 1447.

54 T. J. Meyer and H. Taube, *Inorg. Chem.*, 1968, **7**, 2369.

55 G. M. Brown, H. J. Krentzien, M. Abe and H. Taube, *Inorg. Chem.*, 1979, **18**, 3374.

56 F. P. Dwyer and A. M. Sargeson, *J. Phys. Chem.*, 1961, **65**, 1892.

57 I. Ruff and M. Zimonyi, *Electrochimica Acta*, 1973, **18**, 515.

58 D. H. Macartney and N. Sutin, *Inorg. Chem.*, 1983, **22**, 3530.

59 R. C. Young, F. R. Keene and T. J. Meyer, *J. Am. Chem. Soc.*, 1977, **99**, 2468.

60 H. Oberhofer and J. Blumberger, *Angew. Chem. Int. Ed.*, 2010, **49**, 3631.

61 M. D. Newton, *J. Phys. Chem.*, 1991, **95**, 30.

62 D. Zhang, B. Zhuang, D. Feng and C. Liu, *Int. J. Quant. Chem.*, 2000, **78**, 32.

63 K. M. Rosso and J. R. Rustad, *J. Phys. Chem. A*, 2000, **104**, 6718.

64 R. G. Endres, M. X. LaBute and D. L. Cox, *J. Chem. Phys.*, 2003, **118** 8706.

65 X. Zeng, X. Hu and W. Yang, *J. Chem. Theory. Comput.*, 2012, **8**, 4960.

66 R. L. Kenion and N. Ananth, *Phys. Chem. Chem. Phys.*, 2016, **18**, 26117.

67 F. M. Bickelhaupt, *J. Comput. Chem.*, 1999, **20**, 114.

68 L. P. Wolters and F. M. Bickelhaupt, *WIREs Comput. Mol. Sci.*, 2015, **5**, 324.

69 F. M. Bickelhaupt and K. N. Houk, *Angew. Chem. Int. Ed.*, 2017, **56**, 10070.

70 F. P. Rotzinger, *Inorg. Chem.*, 2015, **54**, 10450.

71 S. Maeda, Y. Harabuchi, M. Takagi, K. Saita, K. Suzuki, T. Ichino, Y. Sumiya, K. Sugiyama and Y. Ono, *J. Comput. Chem.*, 2018, **39**, 233.

72 S. Maeda, Y. Harabuchi, M. Takagi, T. Taketsugu and K. Morokuma, *Chem. Rec.*, 2016, **16**, 2232.

73 S. Maeda, K. Ohno and K. Morokuma, *Phys. Chem. Chem. Phys.*, 2013, **15**, 3683.

74 M. J. Bearpark, M. A. Robb and H. B. Schlegel, *Chem. Phys. Lett.*, 1994, **223**, 269.

75 S. Maeda, K. Ohno and K. Morokuma, *J. Chem. Theory Comput.*, 2010, **6**, 1538.

76 M. J. Frisch, G. W. Trucks, H. B. Schlegel, G. E. Scuseria, M. A. Robb, J. R. Cheeseman, G. Scalmani, V. Barone, G. A. Petersson, H. Nakatsuji, X. Li, M. Caricato, A. V. Marenich, J. Bloino, B. G. Janesko, R. Gomperts, B. Mennucci, H. P. Hratchian, J. V. Ortiz, A. F. Izmaylov, J. L. Sonnenberg, D. Williams-Young, F. Ding, F. Lipparini, F. Egidi, J. Goings, B. Peng, A. Petrone, T. Henderson, D. Ranasinghe, V. G. Zakrzewski, J. Gao, N. Rega, G. Zheng, W. Liang, M. Hada, M. Ehara, K. Toyota, R. Fukuda, J. Hasegawa, M. Ishida, T. Nakajima, Y. Honda, O. Kitao, H. Nakai, T. Vreven, K. Throssell, J. A. Montgomery, Jr., J. E. Peralta, F. Ogliaro, M. J. Bearpark, J. J. Heyd, E. N. Brothers, K. N. Kudin, V. N.

Staroverov, T. A. Keith, R. Kobayashi, J. Normand, K. Raghavachari, A. P. Rendell, J. C. Burant, S. S. Iyengar, J. Tomasi, M. Cossi, J. M. Millam, M. Klene, C. Adamo, R. Cammi, J. W. Ochterski, R. L. Martin, K. Morokuma, O. Farkas, J. B. Foresman, and D. J. Fox, Gaussian 16, Revision C.02, Gaussian, Inc., Wallingford CT, 2019.

77 J. D. Chai and M. H. Gordon, *Phys. Chem. Chem. Phys.*, 2008, **10**, 6615.

78 F. Weigend and R. Ahlrichs, *Phys. Chem. Chem. Phys.*, 2005, **7**, 3297.

79 V. Barone and M. Cossi, *J. Phys. Chem. A*, 1998, **102**, 1995.

80 M. Cossi, N. Rega, G. Scalmani and V. Barone, *J. Comput. Chem.*, 2003, **24**, 669.

81 F. Weigend, *Phys. Chem. Chem. Phys.*, 2006, **8**, 1057.

82 C. Daniel, *Phys. Chem. Chem. Phys.*, 2021, **23**, 43.

83 Y. Bu, Y. Wang, F. Xu, and C. Deng, *J. Mol. Struct.*, 1998, **453**, 43.

84 R. F. Ribeiro, A. V. Marenich, C. J. Cramer and D. G. Truhlar, *J. Phys. Chem. B*, 2011, **115**, 14556.

85 R. L. Martin, P. J. Hay and L. R. Pratt, *J. Phys. Chem. A*, 1998, **102**, 3565.

86 Y. Liu, Y. Tang, Y. Y. Jiang, X. Zhang, P. Li and S. Bi, *ACS Catal.*, 2017, **7**, 1886.

87 Z. Xu, Y. Yang, J. Jiang and Y. Fu, *Organometallics*, 2018, **37**, 1114.

Chapter 4

The EDEEL method and the SAES method: a case study of intramolecular electron transfer reactions in radical anions

4.1 Introduction

Electron transfer (ET) is becoming more important as a fundamental process in chemistry.[1–6] According to the Marcus theory, ET proceeds through the crossing region of two potential energy surfaces (PESs) corresponding to initial and final electronic states of the system.[7] In recent years, analyses of non-adiabatic processes based on the crossing region geometries, seam of crossing (SX) and conical intersection (CI), have been getting more common.[8–14] In my previous study, "the energy decomposition and extrapolation-based electron localization" (EDEEL) method[15] was developed as an energy extrapolation scheme[16–18] for analysis of ET process by geometry optimization on PESs. The crossing region optimization allows detailed analysis of the phenomena taking place at SX or CI beyond harmonic approximation with moderate computational cost, and clear reaction coordinates are obtained for intuitive understanding. It is expected that establishment of a simple scheme to analyze ET process by SX region optimization will help our understanding of reaction mechanisms and designing novel reactions.

The first-order rate constant of electron transfer k_{ET} for weakly-coupled system is expressed as eqn (4.1) by the Marcus theory.[7,19]

$$k_{\mathrm{ET}} = \Gamma_{\mathrm{n}} \frac{2|V_{12}|^2}{h} \left(\frac{\pi^3}{\lambda k_{\mathrm{B}} T} \right)^{1/2} \exp\left(-\frac{\Delta G_{\mathrm{na}}^{\ddagger}}{RT} \right) \tag{4.1}$$

In eqn (4.1), Γ_n is the nuclear tunneling factor, V_{12} is the coupling constant, h is the Planck constant, λ is the reorganization energy, k_B is the Boltzmann constant, T is the temperature, $\Delta G_{na}^{\ddagger}$ is the Gibbs free energy of activation (subscript "na" denotes "non-adiabatic"), and R is the gas constant

(Fig. 4.1). By applying the harmonic approximation to the initial and final state diabatic PESs, $\Delta G_{\mathrm{na}}^{\ddagger}$ is expressed with λ and the reaction free energy ΔG^{0} as eqn (4.2).[7,19]

$$\Delta G_{\mathrm{na}}^{\ddagger} = \frac{(\lambda + \Delta G^{0})^{2}}{4\lambda} \tag{4.2}$$

Eqn (4.2) allows to estimate the $\Delta G_{\mathrm{na}}^{\ddagger}$ without the information of crossing region. In my scheme, $\Delta G_{\mathrm{na}}^{\ddagger}$ is obtained directly from crossing-region optimization as the energy difference between the SX and the equilibrium geometry (EQ) of initial state.

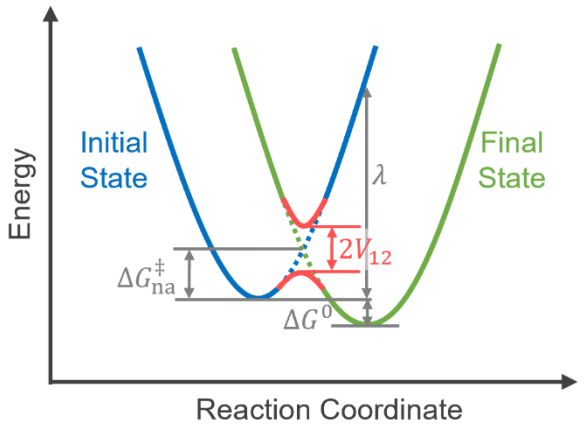

Fig. 4.1 Diabatic potentials (blue and green) and crossing region. The red curves in the crossing region are the corresponding adiabatic potentials. Relations among the parameters in eqn (4.1) are also shown.

One of the important conclusions of the Marcus theory is the existence of the Marucs inverted region, where ET becomes slower in extremely exothermic process (Fig. 4.2).[7,20] This inverted region behavior is especially important in photochemistry such as solar energy conversion[21,22] and other chemical reactions too[23,24]. Moreover, the nuclear tunneling effect often plays a key role in the inverted region[7,19], making theoretical analysis even more complicated. Therefore, a simple scheme which can analyze ET from the Marcus normal region to the inverted region with the

nuclear tunneling effect is desired. The Franck-Condon (FC) factor calculation is one of them. The FC factor incorporates the nuclear tunneling effect by calculating the overlap of vibrational wavefunctions of initial and final state.[7,19]

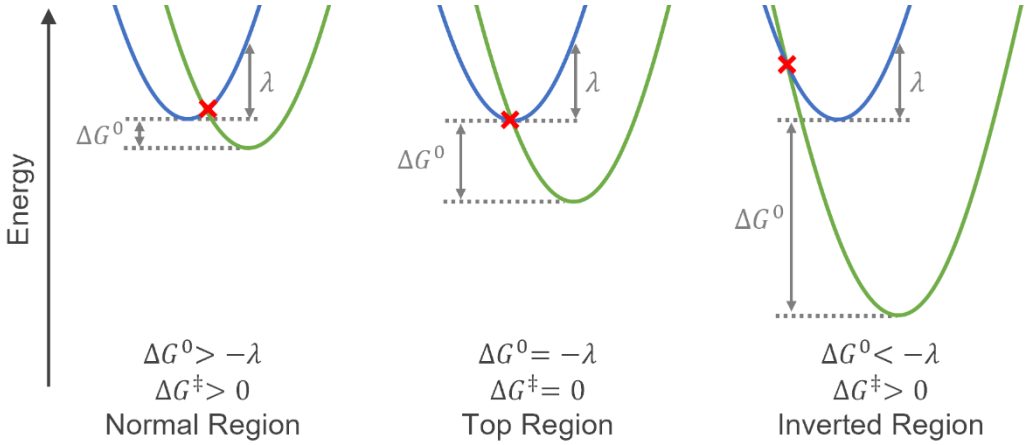

Fig. 4.2 Illustrations of the Marcus normal region, the top region, and the inverted region. Blue and green curves are the initial and final state potentials, respectively

For ET in a polar solvent, orientations of solvent molecules are critically important.[7,19,25,26] The ET is activated by both donor and acceptor (inner-sphere) deformation and the solvent orientation (outer-sphere) change. However, it is not always feasible in computation to optimize geometries with explicit solvent molecules due to the exhaustive computational cost. For long years, implicit solvent models such as self-consistent reaction field (SCRF) have been widely used in computational chemistry.[27–32] Though these models allow to reduce the computational cost drastically, they do not express the solvent activation of ET reaction in diabatic states. Therefore, a simple method to incorporate the solvent activation into the crossing geometry optimization is needed. In this paper, I propose such a method as one of energy shift methods. [13,33,34] The nuclear

tunneling effect is also considered in ET rate constant evaluation using expressions proposed by Scher and Holstein.[19,35]

4.2 Method

In my previous study, the EDEEL method for intermolecular ET was developed and applied to the electron self-exchange reactions between transition metal complexes.[15] In the present study, the EDEEL method is extended for intramolecular ET within a bridged molecular D-B-A (D: Donor, B: Bridge, A: Acceptor). In this method, the diabatic energies for the initial and final states V_{11} and V_{22} are given by eqn (4.3)-(4.4).

$$V_{11}(\mathbf{R}) = E_{n+m}^{\mathrm{DBA}}(\mathbf{R}) - E_{n}^{\mathrm{DB}}(\mathbf{R}^{\mathrm{DB}}) + E_{n+1}^{\mathrm{DB}}(\mathbf{R}^{\mathbf{DB}}) \tag{4.3}$$

$$V_{22}(\mathbf{R}) = E_{n+m}^{\mathrm{DBA}}(\mathbf{R}) - E_{m}^{\mathrm{BA}}(\mathbf{R}^{\mathrm{BA}}) + E_{m+1}^{\mathrm{BA}}(\mathbf{R}^{\mathrm{BA}}) \tag{4.4}$$

Vector $\boldsymbol{R}$ is the geometry of the D-B-A system, and $\boldsymbol{R}^{\mathrm{DB}}$ and $\boldsymbol{R}^{\mathrm{DA}}$ are its DB and BA components, respectively. The subscript of each adiabatic energy E denotes the number of electrons in the corresponding system. In diabatic states calculated by the eqn (4.3)-(4.4), the moving electron is localized on either donor or acceptor species, and the moving electron does not interact with the corresponding counterpart species. The difference from the EDEEL equations for intermolecular ET is the existence of the bridge structure denoted as “B”. The valence bond between bridge and acceptor or donor and bridge is cut and capped by a hydrogen atom for V_{11} and V_{22}, respectively. The EDEEL method also allows easy calculation of an “excited state with desired localization of transferring electron” by applying time dependent-density functional theory (TD-DFT) to the calculation of $E_{n+1}^{\mathrm{DB}}(\mathbf{R}^{\mathbf{DB}})$ or $E_{m+1}^{\mathrm{BA}}(\mathbf{R}^{\mathrm{BA}})$, and this feature works in some ET process such as ET in *n*-octane solvent in the case study.

In this study, activation by solvent molecules surrounding solute is incorporated into the crossing geometry optimization as an energy shift method[13,33,34] using harmonic functions of the Marcus

theory eqn (4.5)-(4.6) for initial and final state, respectively.[36] I call this energy shift method as "solvent activation energy shift" (SAES).

$$G_{\mathrm{SA}}^{\mathrm{i}}(x;\alpha_{\mathrm{SA}}) = \lambda_{\mathrm{s}}^{\mathrm{i}} x^2 \tag{4.5}$$

$$G_{\mathrm{SA}}^{\mathrm{f}}(x;\alpha_{\mathrm{SA}}) = \lambda_{\mathrm{s}}^{\mathrm{f}} (1-x)^2 \tag{4.6}$$

Parameters $\lambda_{\mathrm{s}}^{\mathrm{i}}$ and $\lambda_{\mathrm{s}}^{\mathrm{f}}$ are the solvent reorganization energies of initial and final state. Variable x is the dimensionless solvent orientation coordinate where the solvent orientation relaxed to initial and final state are zero and one, respectively. Coordinate x in eqn (4.7) is composed of two parameters α_{SA} and $x_{\mathrm{s}}^{\ddagger}$. The subscript "SA" is the abbreviation of "Solvent Activation".

$$x = \alpha_{\mathrm{SA}} x_{\mathrm{s}}^{\ddagger} \tag{4.7}$$

$$x_{\mathrm{s}}^{\ddagger} = \frac{\lambda_{\mathrm{s}}^{\mathrm{f}} - \sqrt{\lambda_{\mathrm{s}}^{\mathrm{i}}\lambda_{\mathrm{s}}^{\mathrm{f}} - \left(\lambda_{\mathrm{s}}^{\mathrm{f}} - \lambda_{\mathrm{s}}^{\mathrm{i}}\right)\Delta G_{\mathrm{s}}^{0}}}{\lambda_{\mathrm{s}}^{\mathrm{f}} - \lambda_{\mathrm{s}}^{\mathrm{i}}} \tag{4.8}$$

When $\lambda_{\mathrm{s}}^{\mathrm{i}} = \lambda_{\mathrm{s}}^{\mathrm{f}} = \lambda_{\mathrm{s}}$ holds, eq8 is replaced by eqn (4.9).[19]

$$x_{\mathrm{s}}^{\ddagger} = \frac{1}{2}\left(1 + \frac{\Delta G_{\mathrm{s}}^{0}}{\lambda_{\mathrm{s}}}\right) \tag{4.9}$$

The parameter $x_{\mathrm{s}}^{\ddagger}$ is the solvent orientation coordinate when the ET is activated only by the solvent orientation change without activation of donor and acceptor. Activation of solvent is adjusted by modifying the scaling parameter α_{SA} within 0 and 1. In the case of $\alpha_{\mathrm{SA}} = 0$, ET is activated only by deformation of donor and acceptor. In the case of $\alpha_{\mathrm{SA}} = 1$, ET is activated only by orientation change of the surrounding solvent molecules. In the case of $0 < \alpha_{\mathrm{SA}} < 1$, ET is activated by both deformation of the donor and acceptor and the solvent molecules orientation change. In other words, α_{SA} controls the balance of inner-sphere and outer-sphere activation. Outside of $0 \leq \alpha_{\mathrm{SA}} \leq 1$ can be also calculated, which may be needed when variation of the electronic coupling and the nuclear tunneling are considered. It is important that the SAES method is constructed to be used with an SCRF method such as the polarizable continuum model (PCM)[28], conductor-like PCM (C-PCM)[29,30] or solvation model density (SMD)[31]. Moreover, the SCRF must

be relaxed to the initial and final state, respectively. This is because eqn (4.5) and eqn (4.6) are the energies needed to reach a certain solvent coordinate x from the bottom of the initial and final state solvent potential, respectively. Note that when $G_{\mathrm{SA}}^{\mathrm{i}}(x;\alpha_{\mathrm{SA}})$ and $G_{\mathrm{SA}}^{\mathrm{f}}(x;\alpha_{\mathrm{SA}})$ are added to V_{11} and V_{22}, the orientation of solvent molecules is virtually the same in the initial and final state since eqn (4.5) and eqn (4.6) share the same coordinate x. The SAES method can be combined with an arbitral diabatization method.

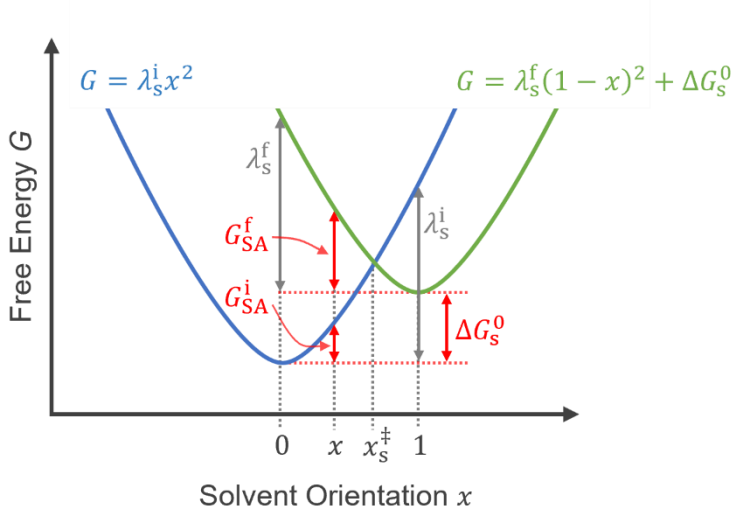

Fig. 4.3 Harmonic approximated free energy surfaces of initial (blue) and final (green) states along the solvent orientation axis at a fixed donor and acceptor coordinate. Solvent reorganization energies $\lambda_{\mathrm{s}}^{\mathrm{i}}$ and $\lambda_{\mathrm{s}}^{\mathrm{f}}$, solvent activation energies $G_{\mathrm{SA}}^{\mathrm{i}}$ and $G_{\mathrm{SA}}^{\mathrm{f}}$, and solvent reaction energy G_{s}^{0} for the SAES method are also shown.

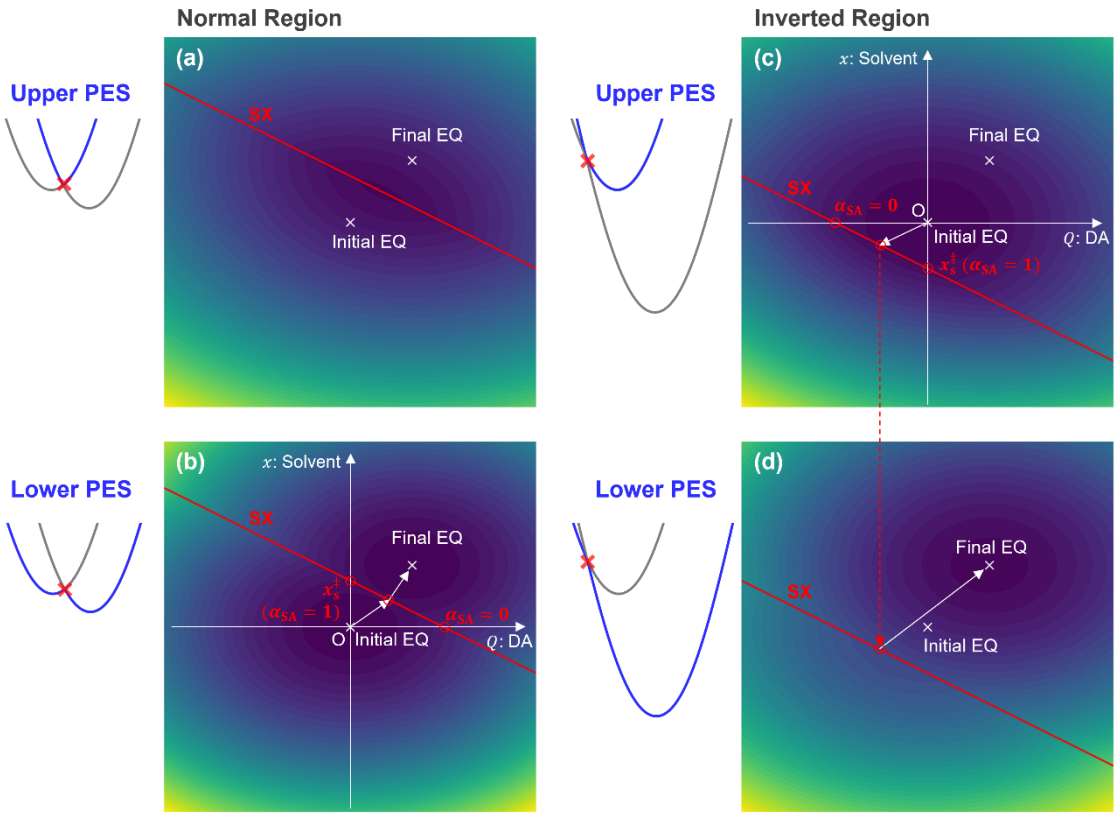

Fig. 4.4 Graphical images of sequential seam of crossing (SX) optimization with reducing α_{SA} on model diabatic PESs. (a) Upper diabatic PES of the normal region. (b) Lower diabatic PES of the normal region. (c) Upper diabatic PES of the inverted region. (d) Lower diabatic PES of the inverted region. Red solid lines across the PESs represent the SX.

Parameters λ_s^i and λ_s^f are evaluated by eqn (4.10)-(4.11) at the initial state EQ with C-PCM using NonEquilibrium=Save and NonEquilibrium=Read options in Gaussian 16.[30,37] ε_0, ε_s, and ε_s are the dielectric constant of gas phase, optical dielectric constant, and static dielectric constant, respectively. e is the absolute quantity of the transferred charge and R_{DA} is the distance between the centroids of donor and acceptor. λ_s^i and λ_s^f are the energy differences shown in Fig 4.3. It was found that λ_s^i and λ_s^f are sensitive to the cavity size scaling of C-PCM. Therefore, the proper cavity scaling factor should be determined for each case.[32] On the other hand, reaction

energies are insensitive to the scaling for the target radical anions. Besides, λ_s^i and λ_s^f are insensitive to geometrical change of donor and acceptor along the geometry optimization.

$$\lambda_s^i = E_{n+1}^{DB(NonEq)} + E_m^{BA(NonEq)} - E_{n+1}^{DB(Eq)} - E_m^{BA(Eq)} - \frac{e^2}{4\pi\varepsilon_0}\left(\frac{1}{\varepsilon_\infty} - \frac{1}{\varepsilon_s}\right)\frac{1}{R_{DA}} \quad (4.10)$$

$$\lambda_s^f = E_n^{DB(NonEq)} + E_{m+1}^{BA(NonEq)} - E_n^{DB(Eq)} - E_{m+1}^{BA(Eq)} - \frac{e^2}{4\pi\varepsilon_0}\left(\frac{1}{\varepsilon_\infty} - \frac{1}{\varepsilon_s}\right)\frac{1}{R_{DA}} \quad (4.11)$$

In the nonpolar limit of $\varepsilon_\infty = 1$ and $\varepsilon_s = 1$, namely the dielectric constant of vacuum, λ_s^i and λ_s^f ideally become 0. In this case, $G_{SA}^i(x;\alpha_{SA})$ and $G_{SA}^f(x;\alpha_{SA})$ are also 0, consisting with the fact that no solvent activation takes place in vacuum.

The contribution of the nuclear tunneling effect to the k_{ET} will be larger for the Marcus inverted region due to the thinner reaction barrier compared to the normal region (Fig. 4.2). A convenient expression of Γ_n for electron transfer was derived by Scher and Holstein as eqn (4.12)-(4.16).[19,35] In the calculation of Γ_n, it is assumed that the nuclear tunneling takes place only for the reaction barrier of inner-sphere deformation. This is based on the difference of vibrational frequencies between the high-frequency inner-sphere vibration and the low-frequency outer-sphere vibration corresponding to the solvent orientation change.[19] Therefore, Γ_n is calculated for the barrier of donor-acceptor activation in a certain solvent orientation.

$$\Gamma_n = \frac{\kappa_n}{(\kappa_n)_\infty} \quad (4.12)$$

$$\Delta G_{na}^{\ddagger}(T) = \frac{\Delta E_{in}^0}{2} + \frac{\lambda_{in} k_B T}{h\nu_{in}}\left\{\coth\left(\frac{h\nu_{in}}{2k_B T}\right) - \left[\frac{{\Delta E_{in}^0}^2}{\lambda_{in}^2} + \operatorname{csch}^2\left(\frac{h\nu_{in}}{2k_B T}\right)\right]^{1/2} + \left(\frac{\Delta E_{in}^0}{\lambda_{in}}\right)\sinh^{-1}\left[\left(\frac{\Delta E_{in}^0}{\lambda_{in}}\right)\sinh\left(\frac{h\nu_{in}}{2k_B T}\right)\right]\right\} \quad (4.13)$$

$$\kappa_n = \exp\left(-\frac{\Delta E_{in}^0}{2RT} + \frac{\lambda_{in}}{h\nu}\left\{\coth\left(\frac{h\nu_{in}}{2k_B T}\right) - \left[\frac{{\Delta E_{in}^0}^2}{\lambda_{in}^2} + \operatorname{csch}^2\left(\frac{h\nu_{in}}{2k_B T}\right)\right]^{1/2} + \left(\frac{\Delta E_{in}^0}{\lambda_{in}}\right)\sinh^{-1}\left[\left(\frac{\Delta E_{in}^0}{\lambda_{in}}\right)\sinh\left(\frac{h\nu_{in}}{2k_B T}\right)\right]\right\}\right) \quad (4.14)$$

$$\Delta G_{\mathrm{na}}^{\ddagger}(T \to \infty) = \frac{\left(\lambda_{\mathrm{in}} + \Delta E_{\mathrm{in}}^{0}\right)^{2}}{4\lambda_{\mathrm{in}}} \tag{4.15}$$

$$(\kappa_{\mathrm{n}})_{\infty} = \exp\left(-\frac{\left(\lambda_{\mathrm{in}} + \Delta E_{\mathrm{in}}^{0}\right)^{2}}{4\lambda_{\mathrm{in}} RT}\right) \tag{4.16}$$

In which three required parameters ν_{in}, $\Delta E_{\mathrm{in}}^{0}$, and λ_{in} are single mode vibrational frequency of donor and acceptor, reaction energy of inner-sphere, and inner-sphere reorganization in electronic energy, respectively. These parameters are calculated from harmonic approximation of initial and final state PES at the SX. See chapter 4.7 for details of the parameter calculation. The total reorganization energy by eqn (4.17) is used for rate constant calculation with eqn (4.1).

$$\lambda = \lambda_{\mathrm{in}} + \frac{\left(\lambda_{\mathrm{s}}^{\mathrm{i}} + \lambda_{\mathrm{s}}^{\mathrm{f}}\right)}{2} \tag{4.17}$$

The electronic coupling V_{12} is necessary for k_{ET} evaluation with eqn (4.1). In this study, the Mulliken-Hush method[38–40] was employed for the coupling calculation, where V_{12} is calculated by the following equation.

$$V_{12} = \frac{E_{\mathrm{ex}}}{e r_{\mathrm{ab}}} \left|\mu_{\mathrm{ge}}\right| \tag{4.18}$$

E_{ex} is the excitation energy from the adiabatic ground state to the adiabatic excited state corresponding to the ET, or the reverse ET, r_{ab} is the distance of the electron transferred, and μ_{ge} is the transition dipole moement of the excitation. The parameters E_{ex}, r_{ab}, and μ_{ge} were obtained from the TD-DFT calculation at the SX. The lowest adiabatic excited state corresponding to the ET was identified by the option “Pop=dCT” in Gaussian 16, which provides absolute value of the transferred charge and distance of the transfer for each excited state.[41,42] In this study, threshold of charge transfer magnitude more than 0.985 was set empiricaly for selection of the excited state. The mean value of the accepted couplings were used for the SX between initial ground state and final excited state. If propoer excited state is not obtained at an SX, the mean coupling value of other SXs with different α_{SA} is used for the SX. This case is caused by mixing of the ET excited state and other near excited states.[43]

The intramolecular thermal ET reactions in bridged radical anions in Fig. 4.5 were employed for the benchmark calculation. These radical anions with different acceptor species cover from the Marcus normal region to the inverted region.[44–46] As for the experimental data of ET rate constants, the k_{ET} in three different solvents (methyltetrahydrofuran, di-*n*-butylether, and isooctane) are available. There are several computaional studies on these radical anions with molecular vibration calulations and molecular dynamics simulations, evaluating k_{ET} with great accuracy.[47–55]

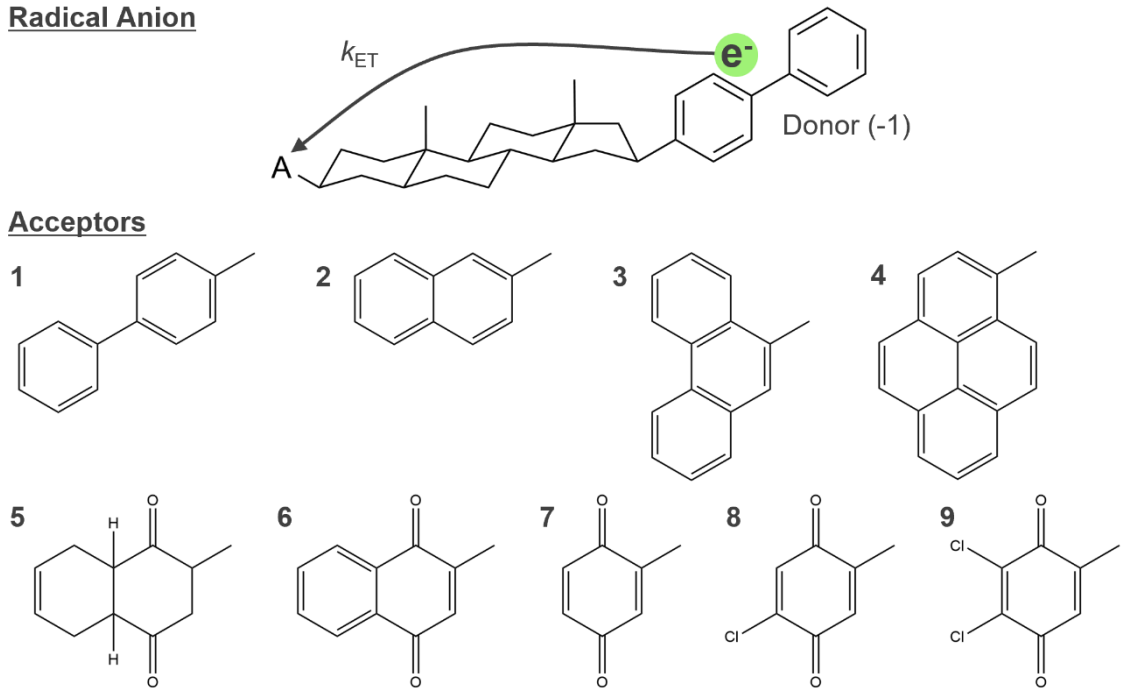

Fig. 4.5 Structure of the radical anion. "A" in the upper structure represents the acceptor moiety. The acceptor moieties are numbered from one to nine.

The procedure of k_{calc} evaluation consists of the following six steps (Fig. 4.6). See the computational section for the details.

(Step 1) Systematic search for equilibrium conformations (EQs) of initial and final state by the EDEEL method at a lower computational level using the SC-AFIR method[56,57] implemented in

the Global Reaction Route Mapping (GRRM) program[58]. Obtained EQs are refined[59] at a higher computational level. The most stable EQs of initial and final states are used in the following steps.

(Step 2) Computation of λ_s^i and λ_s^f and determination of C-PCM cavity scale. The determined cavity scale is used through the following steps.

(Step 3) Refinement optimization of the most stable initial and final state EQs obtained in step 1 with the cavity scale determined in step 2.

(Step 4) Optimization of the SX geometry[60,61] with the SAES method. Start from optimization with $\alpha_{SA} = 1$. Repeat the SX geometry optimization by taking over the optimized geometry and reducing α_{SA} by 0.1 until $\alpha_{SA} = 0$.

(Step 5) TD-DFT single point calculations at the SXs optimized in step 4 for electronic coupling calculation with eqn (4.18) and inner-sphere vibrational frequency calculation for the nuclear tunneling factor calculation.

(Step 6) k_{ET} calculation for each SX with eqn (4.1) and k_{ET} maximization along α_{SA}.

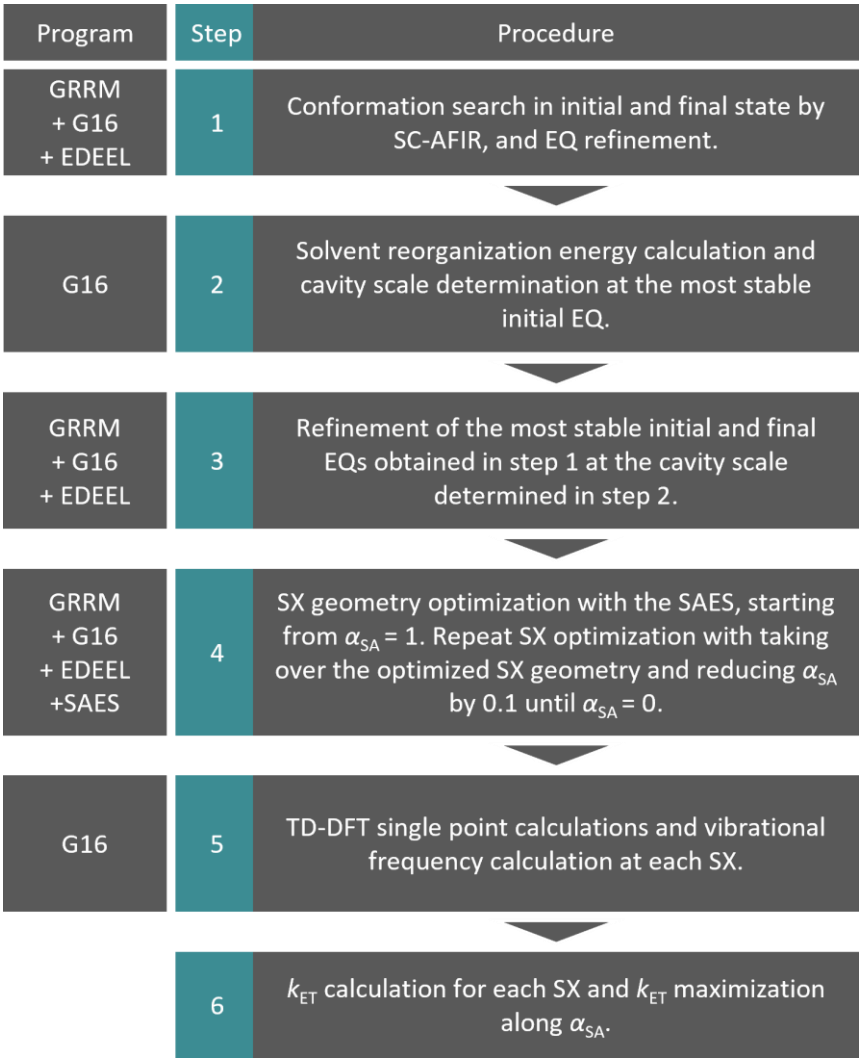

Fig. 4.6 Computational procedure of the sequential SX optimization using the EDEEL method and the SAES method.

4.3 Results and Discussion

The above procedure in Fig. 4.6 was applied to the intramolecular ET in bridged radical anions with nine acceptor species[44–46] shown in Fig. 4.5. Temperature 296 K was used throughout. Calculations with C-PCM of three different solvents, tetrahydrofuran (THF), dibutyl ether (DBE), and *n*-octane, were employed for each acceptor species. Their dielectric constants are ε_∞ = 1.974025 and ε_s = 7.425700 for THF, ε_∞ = 1.957761 and ε_s = 3.047300 for DBE, and ε_∞ = 1.952727

and ε_s = 1.940600 for *n*-octane, which are the default values in Gaussian16 program[62]. An exception was *n*-octane solvent, the least polar solvent among the three. Eqn (4.10)-(4.11) provided negligibly small negative values for *n*-octane regardless of acceptor species, meaning that orientaion of solvent mlecules had little effect to the energy. Therefore, the SX optimization was carried out without the SAES method for *n*-octane. The cavity scaling factors 1.40, which was in the range of common choice[32], was adopted for all the three solvents. Geometry optimization was performed by the GRRM program developer version[58]. Electronic structure calculations were performed by the Gaussian 16 program using density functional theory with level of UωB97X-D/6-31+G(d)[63–75]. The charges and spin multiplicities for the EDEEL method are listed in Table 4.1. Solvent reorganization energies employed in the SAES methods are listed in Table 4.2. SX geometries were optimized for the crossing of ground initial state and ground final state. The crossing of ground initial state and first excited final state were also optimized. Electronic energies were used for all the calculation instead of Gibbs free energies. This treatment assumed that entropic contribution was small because donor and acceptor moieties were fixed on the rigid spacer[52]. Maximized rate constants and other parameters in THF are listed in the Table 4.3. See chapter 4.8 for DBE and *n*-octane. The plots of rate constants are shown in Fig. 4.7. Breakdown of activation energies are shown in Fig 4.8. The rate constants in DBE are not given in table in the reference, and values were extracted from the graph[44] by WebPlotDizitizer[76]. The plot for acceptor 1 and 4 in DBE were not in the graph and the values were estimated from the fitting curve.

Table 4.1 Charges and spin multiplicities of each system calculated in the EDEEL method.

Initial state			Final state		
System	Charge	Spin multiplicity	System	Charge	Spin multiplicity

DBA(n+m)	0	1	DBA(n+m)	0	1
DB(n)	0	1	DA(m)	0	1
DB(n+1)	-1	2	DA(m+1)	-1	2

Table 4.2 Solvent reorganization energies in THF and DBE used for SAES method. Values for the first-excited final state are in parenthesis. Values for *n*-octane are not in the table but approximately -7×10^{-3} eV regardless of acceptor species.

	THF		DBE	
Acceptor	λ_s^i / eV	λ_s^f / eV	λ_s^i / eV	λ_s^f / eV
1	0.83	0.83 (0.86)	0.40	0.40 (0.41)
2	0.84	0.84 (0.84)	0.41	0.41 (0.41)
3	0.78	0.78 (0.80)	0.38	0.38 (0.39)
4	0.79	0.79 (0.79)	0.39	0.39 (0.39)
5	0.84	0.84 (0.86)	0.41	0.41 (0.42)
6	0.83	0.83 (0.83)	0.40	0.40 (0.40)
7	0.87	0.87 (0.88)	0.42	0.42 (0.43)
8	0.85	0.85 (0.86)	0.41	0.41 (0.42)
9	0.83	0.83 (0.84)	0.40	0.40 (0.41)

Table 4.3 $\log_{10}k_{calc}$ and parameters of the SX with maximized k_{ET} in THF.

Acceptor	$\log_{10}k_{calc}$	α_{SA}	V_{12} / eV	λ / eV	$\Delta E^{\ddagger}$ / eV	$\log_{10}\Gamma_n$
1	4.5	0.64	1.5×10^{-3}	1.39	0.40	0.9
2	6.0	0.60	1.4×10^{-3}	1.31	0.31	0.7
3	6.9	0.60	2.3×10^{-3}	1.17	0.27	0.6

4	9.3	0.60	1.1×10^{-3}	1.13	0.08	0.4
5	11.3	0.40	3.9×10^{-3}	1.43	0.00	0.0
6	8.7	0.80	3.3×10^{-3}	1.28	0.16	0.2
7	8.6	0.20	1.1×10^{-3}	1.52	0.35	4.4
8	7.7	0.30	9.6×10^{-4}	1.57	0.42	4.8
9	7.0	0.20	9.5×10^{-4}	1.73	0.58	6.8

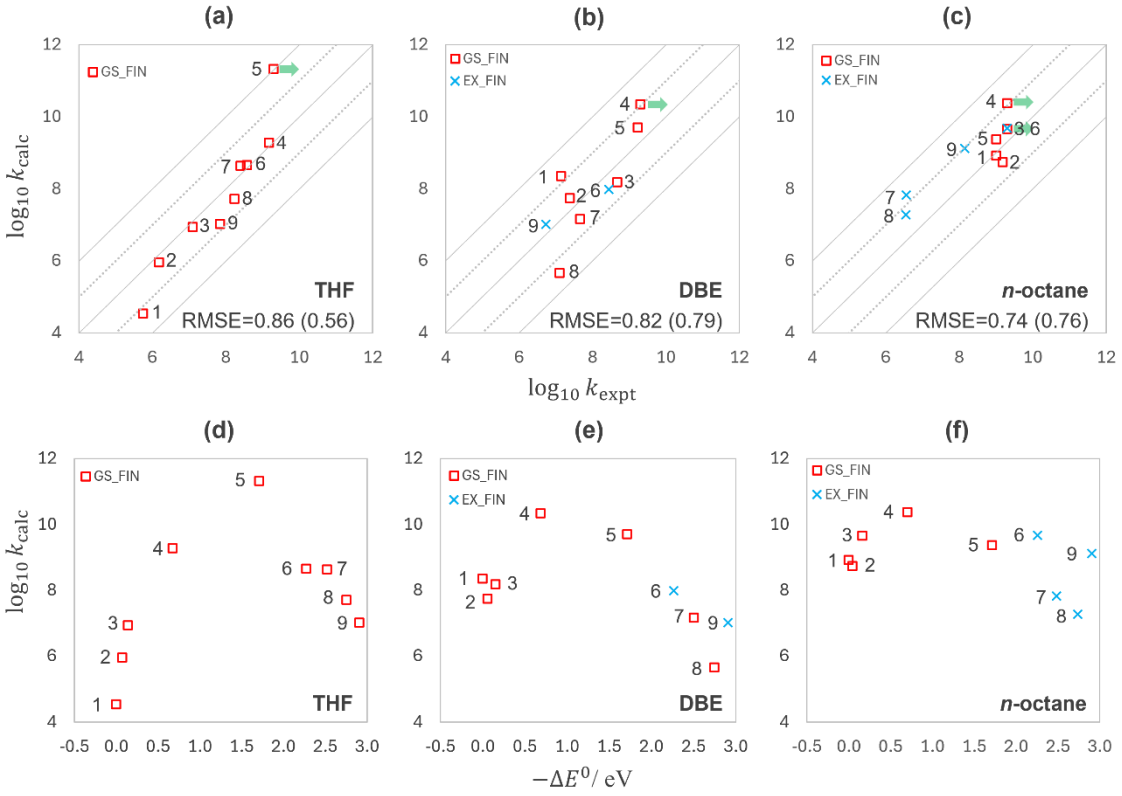

Fig. 4.7 Correlations between experimental $\log_{10}k_{expt}$ and calculated $\log_{10}k_{calc}$ by EDEEL and SAES in (a) THF, (b) DBE, and (c) *n*-octane. The green arrows represent the upper limit of the experimental observation. Red squares represent SX with ground final state. Blue crosses represent SX with the first-excite final state. RMSE in parentheses were calculated by excluding acceptors whose k_{expt} were beyond observation upper limit. Plots of $\log_{10}k_{calc}$ against calculated reaction energies are shown in (d) THF, (e) DBE, and (f) *n*-octane.

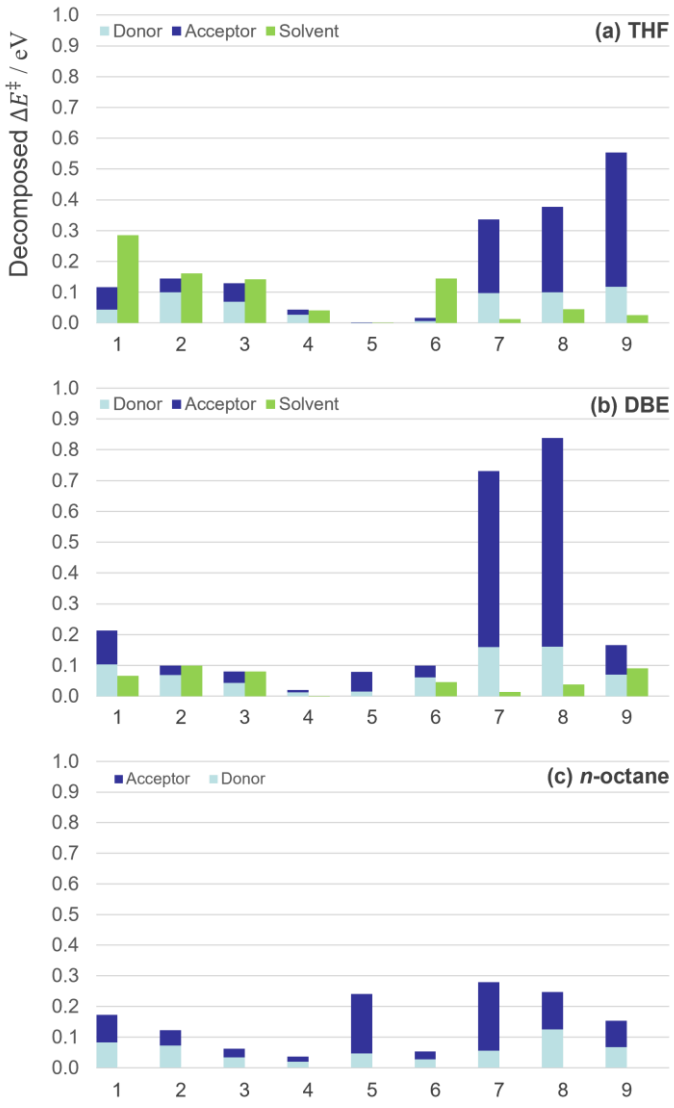

Fig. 4.8 Breakdown of the reaction barriers in (a) THF, (b) DBE, and (c) *n*-octane. See chapter 4.6 for calculation details.

The calculated k_{ET}, from the normal region to the inverted region, showed nice correlations with the experimental values for all the three solvents and reflected the solvent dependency. The breakdowns of the reaction barrier in THF (Fig. 4.8 (a)) show a clear trend. In the normal region, activation by solvent orientation change has a large contribution. In the inverted region, on the

other hand, solvent activation is negligible. This trend came from the nuclear tunneling effect. In the normal region, the nuclear tunneling effect is small due to the thick barrier. Therefore, lowering the total barrier, by balancing the inner-sphere and outer-sphere activation, leads to the large k_{ET}. In the inverted region, the nuclear tunneling effect is much larger due to the thinner barrier. Therefore, enhancing the nuclear tunneling effect by increasing the inner-sphere activation, rather than balancing the inner-sphere and outer-sphere activation, resulted in a larger k_{ET}. In the inverted region in DBE, SX with the first excited final states of acceptors 6 and 9 are faster paths than ground final states. In *n*-octane, this trend is more prominent. This is because in a less polar solvent, meaning smaller solvent reorganization energy, the peak of the Marcus parabola shifts to a less exothermic region. Fine tuning of cavity scale and solvent reorganization energies may improve the results to some extent. Still, there may be several factors contributing to the error such as missing anharmonicity in the solvent potentials, dynamics of solute and solvent molecules, and adaptation of the largest k_{ET}. Better treatment of these factors requires further study in the future.

This sequential SX optimization revealed anharmonicity of the inner-sphere deformation. Fig. 4.9 (a)-(b) show that the vibrational frequencies are decreasing with smaller α_{SA} or larger deformation. These vibrational frequencies, smaller than typical vibrational frequency 1500 cm^{-1} of a conjugated system, corresponds to the previous report[47] though the values range is wider in this present study. Another prominent effect of anharmonicity lies in the inner-sphere reorganization energies λ_{in} (Fig. 4.9 (c)-(d)). λ_{in} calculated at SX with large α_{SA} shows good agreement with previously reported values[48]. On the other hand, λ_{in} at SX with small α_{SA} are much larger, especially in the inverted region. Decrease of ν_{in} and increase of λ_{in} may seem contradicted but it is not. The increase of λ_{in} is due to the shift of final state EQ (minimum point)

of the harmonic potential. (See chapter 4.7.) These results imply that the reaction coordinate is curved due to the anharmonicity or increasing contribution of lower frequency vibrational modes.

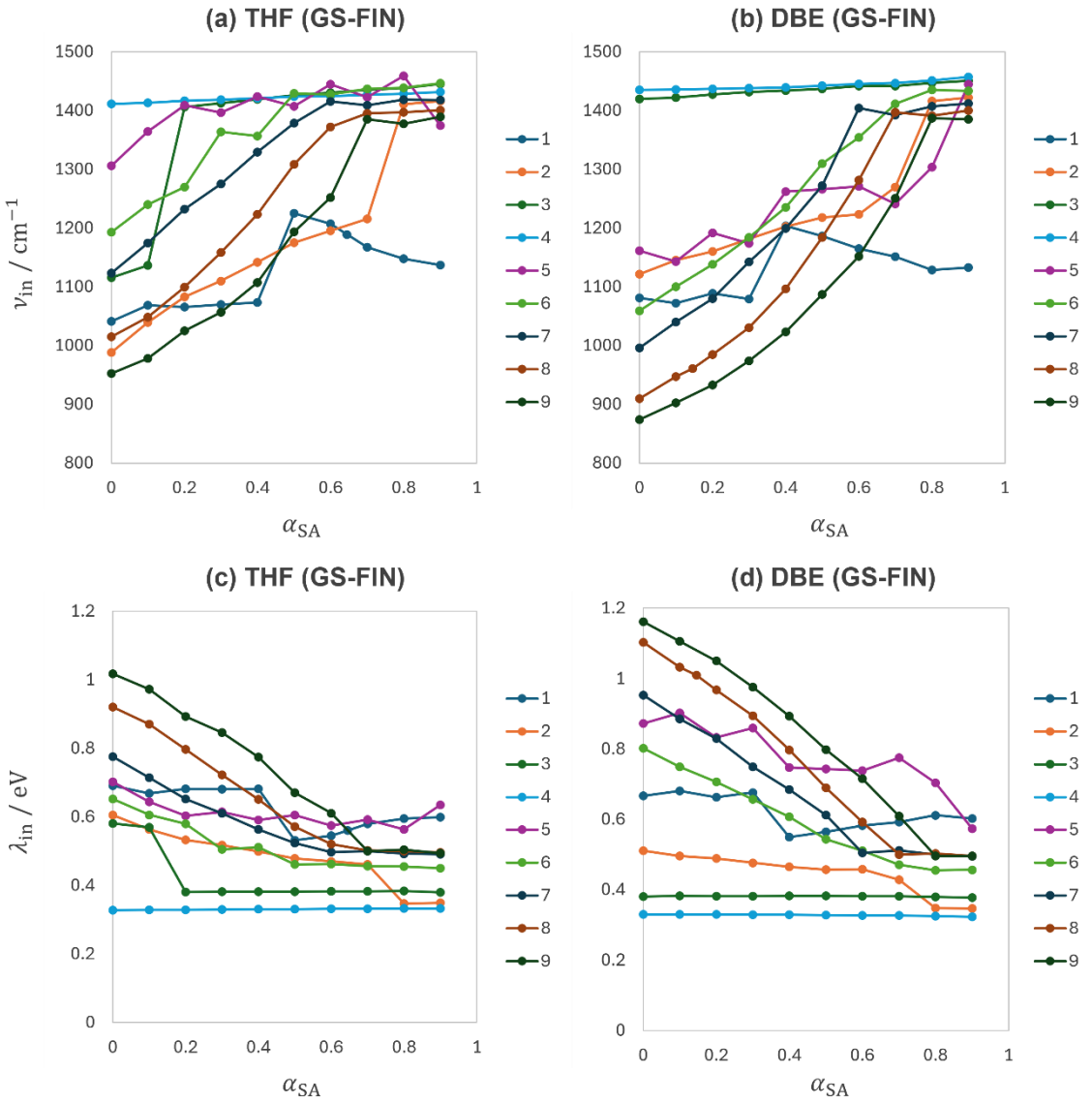

Fig. 4.9 Inner-sphere vibrational frequencies ν_{in} in (a) THF and (b) DBE and inner-sphere reorganization energies λ_{in} in (c) THF and (d) DBE for nine acceptors by harmonic approximation at the SX with ground final state. Values are not available for SX with α_{SA}=1. (See chapter 4.7)

4.4 Conclusion

In this work, the EDEEL method was extended to intramolecular electron transfer reactions. Moreover, the SAES method and the total analysis procedure were developed and applied to the intramolecular electron transfer reactions in radical anions, including the SX with the excited final state. The sequential SX optimization with the SAES method gave qualitative rate constants comparable to the values reported from the experiments. Besides, SX optimization provided breakdowns of the activation energies, prevailing the different trends of the activation in the Marcus normal region and the inverted regions due to the nuclear tunneling effect.

4.5 Computational Section

The EDEEL method and the SAES method were implemented in python script as an interface program between the GRRM program[58] and the Gaussian16 program[62]. The script is executed by the GRRM and takes a geometry from a geometry from GRRM. The script performs multiple electronic structure calculations to obtain the EDEEL PES with the SAES at the geometry using the Gaussian16. Then the script returns the obtained energy, gradient, (and Hessian if requested by GRRM). Some of the initial input geometries were taken from the reference[47]. All the geometry optimizations were performed by a developer version of the GRRM program. Conformation searches in the initial and final state (step 1 of the procedure in Fig. 4.6) were performed by SC-AFIR method[56,57] at the UB97D/6-31G(d)/Auto level[64–73,77–79] with the EDEEL method. Then all the obtained equilibrium geometries were refined[59] at the UωB97X-D/6-31+G(d) level[63–75]. The most stable geometries in initial and final state were employed for the following steps in the workflow. In the other steps, geometry optimizations were performed at the UωB97X-D/6-31+G(d) level. The relaxed orientations of the solvents were expressed by the conductor-like

polarizable continuum model (C-PCM)[29,30]. Reaction energies and reaction barriers were calculated using electronic energies with the SAES method.

4.6 Appendix: Energy Decomposition Analysis

Here explains the procedure of energy decomposition analysis[80–82]. Solvent activation energy is $G_{\mathrm{SA}}^{\mathrm{i}}(x;\alpha_{\mathrm{SA}})$ itself of the SX. The activation energy of the donor $\Delta E_{\mathrm{D}}^{\ddagger}$ is calculated with the following equation.

$$\Delta E_{\mathrm{D}}^{\ddagger} = E_{n+1}^{\mathrm{DB}}\left(\mathbf{R}_{\mathbf{SX}}^{\mathbf{DB}}\right) - E_{n+1}^{\mathrm{DB}}\left(\mathbf{R}_{\mathbf{Initial\ EQ}}^{\mathbf{DB}}\right) \quad (4.\mathrm{S1})$$

$\Delta E_{\mathrm{D}}^{\ddagger}$ contains the deformation energy of the bridge structure, which is assumed to be negligible compared to the donor moiety. Then, the activation energy of the acceptor $\Delta E_{\mathrm{A}}^{\ddagger}$ is calculated using $\Delta E_{\mathrm{D}}^{\ddagger}$ and the inner-sphere activation energy $\Delta E_{\mathrm{in}}^{\ddagger}$.

$$\Delta E_{\mathrm{A}}^{\ddagger} = \Delta E_{\mathrm{in}}^{\ddagger} - \Delta E_{\mathrm{D}}^{\ddagger} \quad (4.\mathrm{S2})$$

Where $\Delta E_{\mathrm{in}}^{\ddagger}$ is calculated with the following eqn (4.S3).

$$\begin{aligned}\Delta E_{\mathrm{in}}^{\ddagger} &= \left\{V_{11}(\mathbf{R}_{\mathbf{SX}}) + G_{\mathrm{SA}}^{\mathrm{i}}(x;\alpha_{\mathrm{SA}})\right\} - \left\{V_{11}\left(\mathbf{R}_{\mathbf{Initial\ EQ}}\right) + G_{\mathrm{SA}}^{\mathrm{i}}(x;\alpha_{\mathrm{SA}})\right\} \\ &= V_{11}(\mathbf{R}_{\mathbf{SX}}) - V_{11}\left(\mathbf{R}_{\mathbf{Initial\ EQ}}\right) \quad (4.\mathrm{S3})\end{aligned}$$

4.7 Appendix: Tunneling Parameters Calculation

Parameters ν_{in}, $\Delta E_{\mathrm{in}}^{0}$, and λ_{in} for the Scher-Holstein method are calculated as follows. In this calculation, energies of the initial EQ and SX are corrected by SAES so that the solvent orientation is virtually the same and fixed by α_{SA}. Moreover, this procedure does not require the optimization of final EQ. This procedure cannot be applied to SX with $\alpha_{\mathrm{SA}} = 1$, in which $\Delta E_{\mathrm{in}}^{\ddagger} = 0$ and tunneling does not occur.

1. Define the harmonic potentials of initial and final state along the DGV direction as eqn (4.S4)-(4.S5), respectively, using the same coefficient a. $q = 0$ corresponds to the initial EQ.

$$V_{11}^{\mathrm{Harmonic}}(q) = aq^2 \tag{4.S4}$$

$$V_{22}^{\mathrm{Harmonic}}(q) = aq^2 + bq + c \tag{4.S5}$$

2. Calculate the mass-weighted difference gradient vector (DGV)[60,61], the direction in which degeneracy of the two states is solved, as eqn (4.S3).

$$\mathbf{v}_{\mathrm{sx}}^{\mathrm{DGV}} = \mathbf{g}_{\mathrm{sx}}^{\mathrm{i}} - \mathbf{g}_{\mathrm{sx}}^{\mathrm{f}} \tag{4.S6}$$

Vectors $\mathbf{g}_{\mathrm{sx}}^{\mathrm{i}}$ and $\mathbf{g}_{\mathrm{sx}}^{\mathrm{f}}$ are the mass-weighted (each element is divided by square root of the atomic mass) first derivatives of the initial and final state at the SX. Then $g_{\mathrm{sx}}^{\mathrm{i}}$ and $g_{\mathrm{sx}}^{\mathrm{f}}$, the gradients of DGV direction at the SX, are obtained from the following equations.

$$g_{\mathrm{sx}}^{\mathrm{i}} = \mathbf{g}_{\mathrm{sx}}^{\mathrm{i}} \cdot \frac{\mathbf{v}_{\mathrm{sx}}^{\mathrm{DGV}}}{\left|\mathbf{v}_{\mathrm{sx}}^{\mathrm{DGV}}\right|} \tag{4.S7}$$

$$g_{\mathrm{sx}}^{\mathrm{f}} = \mathbf{g}_{\mathrm{sx}}^{\mathrm{f}} \cdot \frac{\mathbf{v}_{\mathrm{sx}}^{\mathrm{DGV}}}{\left|\mathbf{v}_{\mathrm{sx}}^{\mathrm{DGV}}\right|} \tag{4.S8}$$

3. Determine the coefficient a from $a = \frac{{g_{\mathrm{sx}}^{\mathrm{i}}}^2}{4\Delta E_{\mathrm{in}}^{\ddagger}}$, in which $\Delta E_{\mathrm{in}}^{\ddagger}$ is the inner-sphere activation energy. Note that when $\alpha_{\mathrm{SA}} = 1$, namely $\Delta E_{\mathrm{in}}^{\ddagger} = 0$, coefficient a cannot be determined. Gradient $g_{\mathrm{sx}}^{\mathrm{i}}$ corresponds to the first derivative of eqn (4.S4) at the SX, namely $g_{\mathrm{sx}}^{\mathrm{i}} = 2aq_{\mathrm{SX}}$. Therefore, the SX coordinate is obtained from $q_{\mathrm{SX}} = \frac{2\Delta E_{\mathrm{in}}^{\ddagger}}{g_{\mathrm{sx}}^{\mathrm{i}}}$. The mass-weighted spring constant k is obtained from $k=2a$, and ν_{in} is obtained from eqn (4.S9).

$$\nu_{\mathrm{in}} = \frac{1}{2\pi}\sqrt{k} \tag{4.S9}$$

4. Coefficient b is obtained as $b = g_{\mathrm{sx}}^{\mathrm{f}} - g_{\mathrm{sx}}^{\mathrm{i}}$ by substituting a, q_{SX}, and $g_{\mathrm{sx}}^{\mathrm{f}}$ into the first derivative of eqn (4.S5), namely $g_{\mathrm{sx}}^{\mathrm{f}} = 2aq_{\mathrm{SX}} + b$.

5. Constant term c is determined by substituting $\Delta E_{\mathrm{in}}^{\ddagger}$, a, b, and q_{SX} into (4.S5).

6. At $q_{\mathrm{EQ}}^{\mathrm{f}}$, the minimum point coordinate of $V_{22}^{\mathrm{Harmonic}}(q)$, first derivative of eqn (4.S5) is zero. Therefore, $q_{\mathrm{EQ}}^{\mathrm{f}}$ is obtained from $q_{\mathrm{EQ}}^{\mathrm{f}} = -\frac{b}{2a}$.

7. Finally, $\Delta E_{\mathrm{in}}^{0}$ is obtained as $\Delta E_{\mathrm{in}}^{0} = a{q_{\mathrm{EQ}}^{\mathrm{f}}}^2 + bq_{\mathrm{EQ}}^{\mathrm{f}} + c$. λ_{in} is obtained as $\lambda_{\mathrm{in}} = a{q_{\mathrm{EQ}}^{\mathrm{f}}}^2$.

When anharmonicity decreases coefficient a, $q_{\mathrm{EQ}}^{\mathrm{f}}$ and λ_{in} may increase.

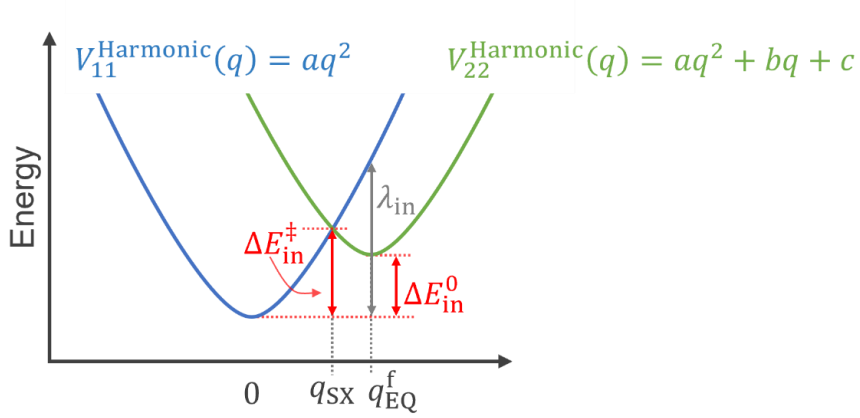

Fig. 4.S1 Illustration of harmonic approximation for nuclear tunneling parameter cauculation.

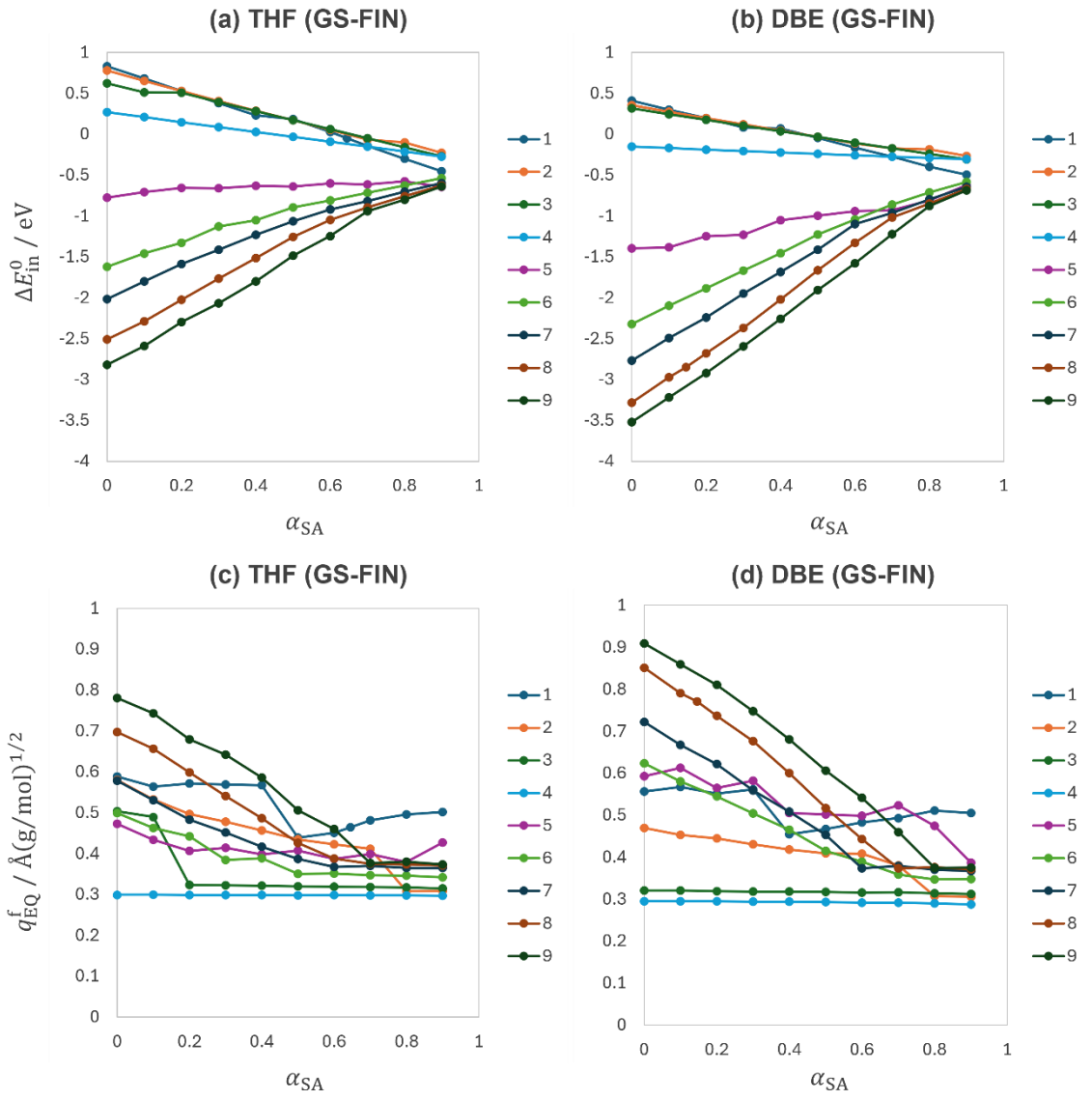

Fig. 4.S2 Inner-sphere reaction energies ΔE^0_{in} in (a) THF and (b) DBE and $q^{\mathrm{f}}_{\mathrm{EQ}}$, the minimum point coordinate of $V_{22}^{\mathrm{Harmonic}}(q)$, in (c) THF and (d) DBE for nine acceptors by harmonic approximation at the SX with ground final state. Values are not available for SX with α_{SA}=1. Note that ΔE^0_{in} is a reaction energy of donor and acceptor in a solvent orientation fixed with α_{SA}.

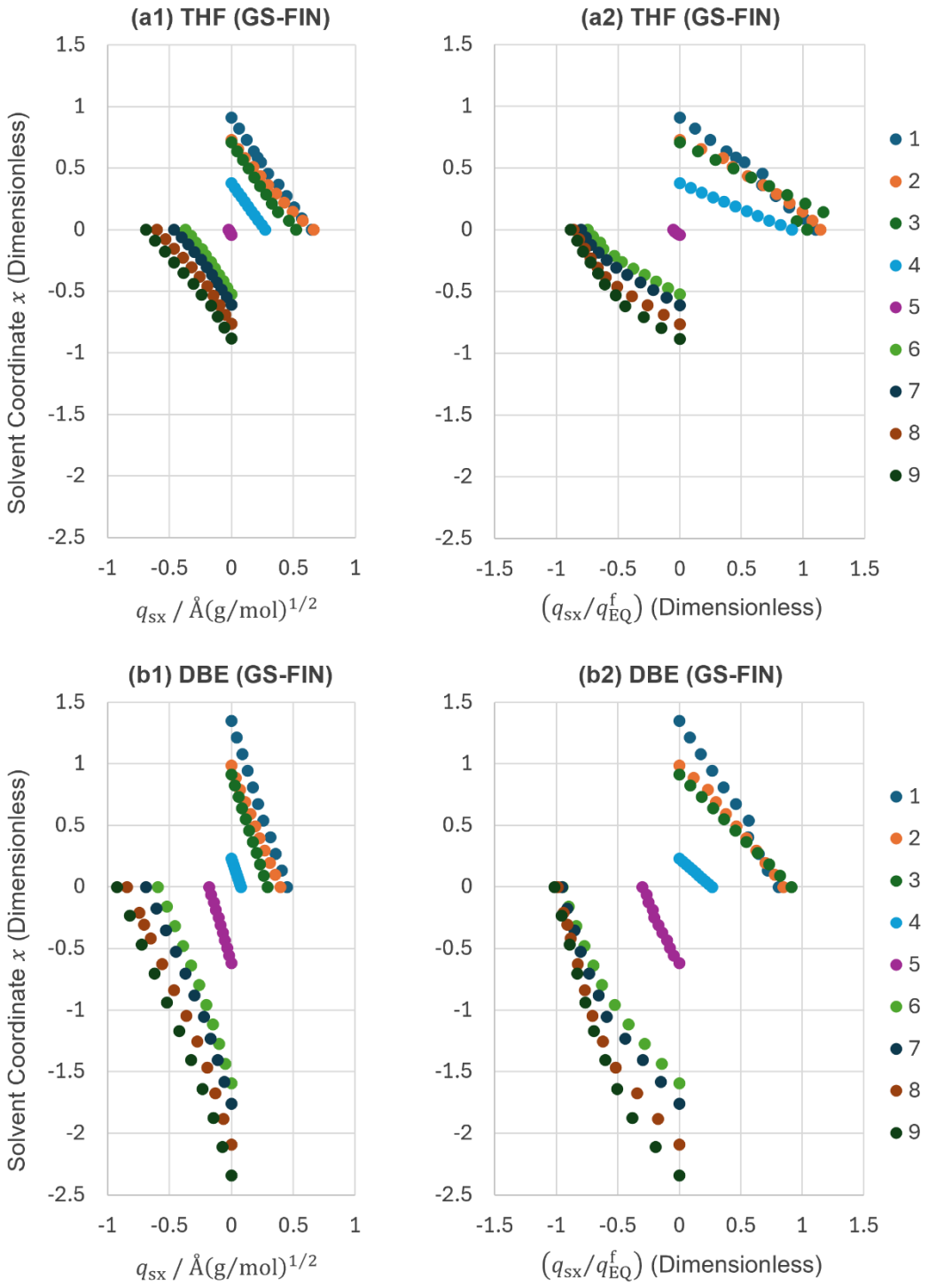

Fig. 4.S3 Relations between the solvent coordinate of the SAES method and (a1) inner-sphere SX mass-weighted coordinates q_{SX} in THF and (a2) the dimensionless inner-sphere SX

coordinates $\frac{q_{SX}}{q_{EQ}^{f}}$ in THF. (b1) and (b2) are coordinates in DBE. In (a2) and (b2), coordinates (0, 0) and (1, 1) correspond to the initial EQ and final EQ, respectively, for all the acceptors.

4.8 Appendix: Rate Constants and Parameters

Table 4.S1 Experimental $\log_{10}k_{expt}$ in MTHF, DBE, and isooctane used in Fig. 4.7 (a)-(c). [44–46]

Acceptor	$\log_{10}k_{expt}$ (MTHF)	$\log_{10}k_{expt}$ (DBE)	$\log_{10}k_{expt}$ (isooctane)
1	5.7	7.1	9.0
2	6.2	7.4	9.2
3	7.1	8.7	9.3
4	9.2	9.3	9.3
5	9.3	9.2	9.0
6	8.6	8.4	9.3
7	8.4	7.7	6.6
8	8.2	7.1	6.5
9	7.8	6.7	8.1

Table 4.S2 Calculated reaction energies in THF, DBE, and *n*-octane used in Fig 4.7 (d)-(e).

Acceptor	ΔE^0 / eV (THF)	ΔE^0 / eV (DBE)	ΔE^0 / eV (*n*-octane)
1	0.003	0.004	0.004
2	-0.073	-0.058	-0.045
3	-0.136	-0.150	-0.163
4	-0.673	-0.688	-0.700
5	-1.706	-1.709	-1.711

6	-2.271	-2.263	-2.256
7	-2.521	-2.502	-2.481
8	-2.751	-2.743	-2.734
9	-2.906	-2.906	-2.904

Table 4.S3 $\log_{10}k_{calc}$ and parameters of the SX with maximized k_{ET} in THF (SX with first-excited final state).

Acceptor	$\log_{10}k_{calc}$	α_{SA}	V_{12} / eV	λ / eV	$\Delta E^{\ddagger}$ / eV	$\log_{10}\Gamma_n$
1	1.3	0.6	1.6×10^{-3}	1.51	0.57	0.5
2	-2.9	0.7	1.6×10^{-3}	1.32	0.82	0.4
3	1.7	1.0	2.3×10^{-3}	0.80	0.55	0.0
4	4.9	0.0	1.1×10^{-3}	1.28	0.32	0.2
5	1.6	0.5	3.4×10^{-3}	1.91	0.64	1.2
6	6.8	0.6	1.1×10^{-3}	1.31	0.25	0.8
7	3.8	0.5	1.1×10^{-3}	1.84	0.49	1.8
8	3.8	0.6	2.1×10^{-3}	1.42	0.45	0.8
9	5.8	0.6	3.2×10^{-3}	1.57	0.37	1.0

Table 4.S4 $\log_{10}k_{calc}$ and parameters of the SX with maximized k_{ET} in DBE (SX with ground final state).

Acceptor	$\log_{10}k_{calc}$	α_{SA}	V_{12} / eV	λ / eV	$\Delta E^{\ddagger}$ / eV	$\log_{10}\Gamma_n$
1	8.4	0.30	9.7×10^{-3}	1.08	0.28	0.9
2	7.7	0.50	1.2×10^{-3}	0.87	0.20	0.7

3	8.2	0.50	9.0×10^{-4}	0.76	0.16	0.7
4	10.3	0.10	1.2×10^{-3}	0.72	0.02	0.2
5	9.7	0.00	9.2×10^{-4}	1.28	0.08	0.9
6	6.9	0.00	8.2×10^{-4}	1.20	0.72	9.2
7	7.2	0.10	1.7×10^{-3}	1.31	0.74	9.2
8	5.7	0.15	1.3×10^{-3}	1.42	0.88	10.3
9	4.1	0.00	1.1×10^{-3}	1.57	1.20	14.3

Table 4.S5 $\log_{10}k_{calc}$ and parameters of the SX with maximized k_{ET} in DBE (SX with first-excited final state).

Acceptor	$\log_{10}k_{calc}$	α_{SA}	V_{12} / eV	λ / eV	$\Delta E^{\ddagger}$ / eV	$\log_{10}\Gamma_n$
1	-2.9	0.40	4.6×10^{-3}	0.97	0.85	0.0
2	-2.0	0.50	2.0×10^{-3}	0.91	0.76	0.1
3	7.2	0.50	9.8×10^{-4}	0.83	0.23	0.8
4	3.6	0.40	8.1×10^{-4}	0.87	0.40	0.3
5	1.8	0.30	6.9×10^{-4}	1.52	0.54	1.1
6	8.0	0.40	5.1×10^{-4}	0.88	0.14	0.8
7	5.5	0.30	1.1×10^{-3}	1.43	0.38	1.9
8	5.1	0.50	9.8×10^{-4}	0.97	0.35	0.9
9	7.0	0.40	1.3×10^{-3}	1.15	0.26	1.0

Table 4.S6 $\log_{10}k_{calc}$ and parameters of the SX in *n*-octane (SX with ground final state).

Acceptor	$\log_{10}k_{calc}$	α_{SA}	V_{12} / eV	λ / eV	$\Delta E^{\ddagger}$ / eV	$\log_{10}\Gamma_n$
1	8.9	-	1.9×10^{-3}	0.68	0.17	1.0

2	8.7	-	8.3×10^{-4}	0.34	0.12	0.5
3	9.7	-	6.9×10^{-4}	0.38	0.06	0.6
4	10.4	-	1.1×10^{-3}	0.33	0.04	0.5
5	9.4	-	1.5×10^{-3}	0.97	0.24	2.9
6	4.7	-	6.3×10^{-4}	0.94	1.13	14.1
7	4.5	-	1.5×10^{-3}	1.07	1.27	15.6
8	3.1	-	1.8×10^{-3}	1.21	1.50	17.9
9	2.2	-	1.8×10^{-3}	1.26	1.62	19.2

Table 4.S7 $\log_{10}k_{calc}$ and parameters of the SX in *n*-octane (SX with first-excited final state).

Acceptor	$\log_{10}k_{calc}$	α_{SA}	V_{12} / eV	λ / eV	$\Delta E^{\ddagger}$ / eV	$\log_{10}\Gamma_n$
1	Not Converged	-	-	-	-	-
2	Not Converged	-	-	-	-	-
3	8.7	-	6.9×10^{-4}	0.42	0.13	0.8
4	5.3	-	1.1×10^{-3}	0.49	0.31	0.2
5	3.9	-	1.5×10^{-3}	1.15	0.45	1.1
6	9.7	-	6.3×10^{-4}	0.37	0.05	0.5
7	7.8	-	1.5×10^{-3}	1.05	0.28	2.0
8	7.3	-	1.8×10^{-3}	0.59	0.25	0.6
9	9.1	-	1.8×10^{-3}	0.70	0.15	0.9

Plots of rate constant maximization are shown in Fig. 4.S4. Some k_{ET} maximization for SX with the first-excited final state stopped at certain α_{SA} due to the SX geometry optimization

convergence failure. In Fig. 4.S4 (b), k_{ET} of acceptor no.4 got rise abruptly at $\alpha_{SA} = 0$. This is likely due to the switching of the first-excited final state with a higher excited state.

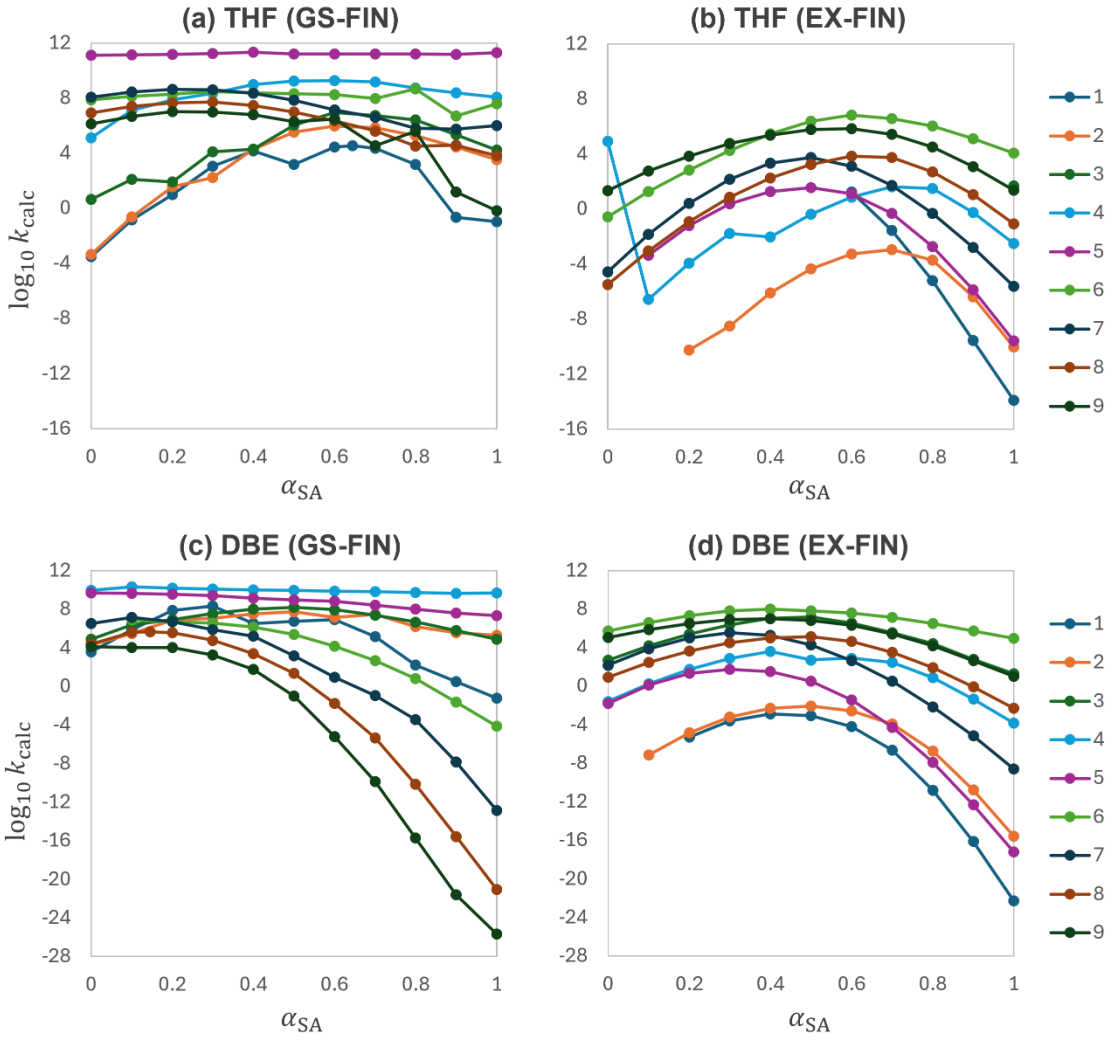

Fig. 4.S4 Rate constant maximization. (a) SX with ground final state in THF, (b) SX with the first-excited final state in THF, (c) SX with ground final state in DBE, and (d) SX with the first-excited final state in DBE.

4.9 Appendix: Geometries

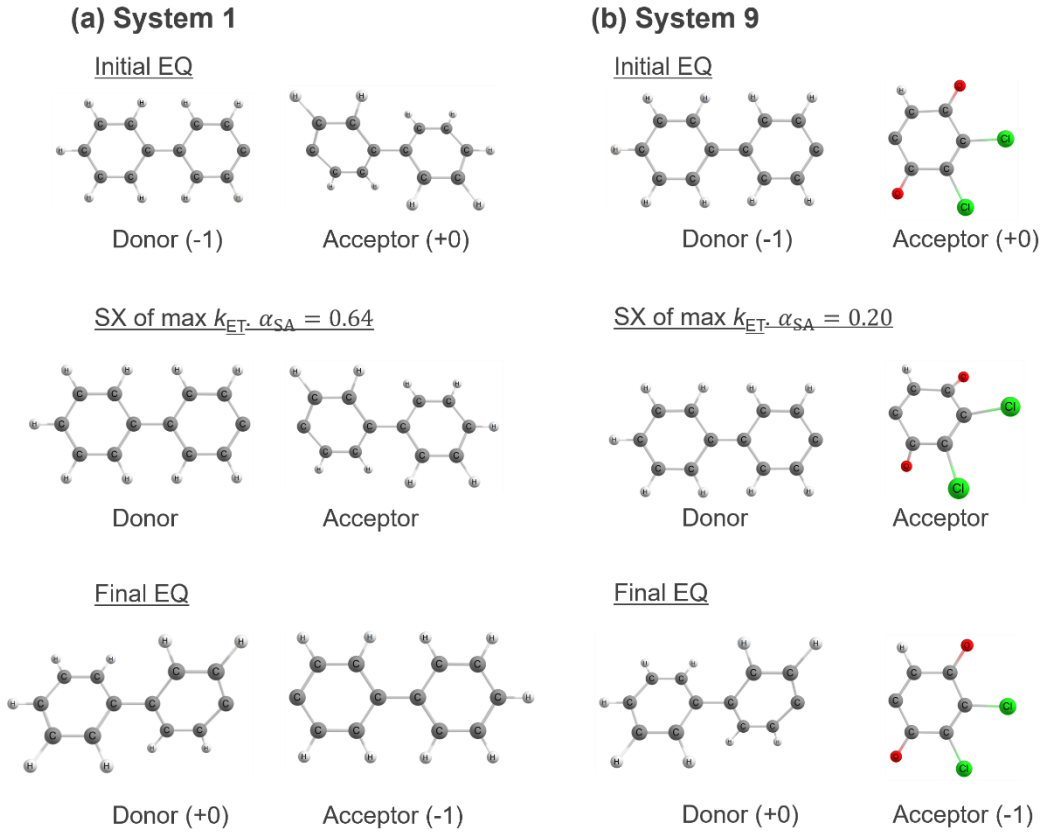

Fig. 4.S5 Geometries of donor and acceptor moieties in THF for system 1 and 9.

References for Chapter 4

1 D. Gust, T. A. Moore and A. L. Moore, *Acc Chem Res*, 2009, **42**, 1890–1898.

2 N. A. Romero and D. A. Nicewicz, *Chem Rev*, 2016, **116**, 10075–10166.

3 N.-T. Suen, S.-F. Hung, Q. Quan, N. Zhang, Y.-J. Xu and H. M. Chen, *Chem. Soc. Rev.*, 2017, **46**, 337–365.

4 A. Mills and S. Le Hunte, *J Photochem Photobiol A Chem*, 1997, **108**, 1–35.

5 A. Hagfeldt, G. Boschloo, L. Sun, L. Kloo and H. Pettersson, *Chem Rev*, 2010, **110**, 6595–6663.

6 D. R. Weinberg, C. J. Gagliardi, J. F. Hull, C. F. Murphy, C. A. Kent, B. C. Westlake, A. Paul, D. H. Ess, D. G. McCafferty and T. J. Meyer, *Chem Rev*, 2012, **112**, 4016–4093.

7 R. A. Marcus and N. Sutin, *Biochimica et Biophysica Acta (BBA) - Reviews on Bioenergetics*, 1985, **811**, 265–322.

8 Y. Harabuchi, T. Taketsugu and S. Maeda, *Phys. Chem. Chem. Phys.*, 2015, **17**, 22561–22565.

9 M. Hatanaka, Y. Hirai, Y. Kitagawa, T. Nakanishi, Y. Hasegawa and K. Morokuma, *Chem. Sci.*, 2017, **8**, 423–429.

10 N. Aizawa, Y. Harabuchi, S. Maeda and Y.-J. Pu, *Nat Commun*, 2020, **11**, 3909.

11 S. Suzuki, S. Sasaki, A. S. Sairi, R. Iwai, B. Z. Tang and G. Konishi, *Angewandte Chemie International Edition*, 2020, **59**, 9856–9867.

12 E. Pieri, D. Lahana, A. M. Chang, C. R. Aldaz, K. C. Thompson and T. J. Martínez, *Chem. Sci.*, 2021, **12**, 7294–7307.

13 Y. Harabuchi, H. Hayashi, H. Takano, T. Mita and S. Maeda, *Angewandte Chemie International Edition*, 2023, **62**, e202211936.

14 Y. Harabuchi, J. Eng, E. Gindensperger, T. Taketsugu, S. Maeda and C. Daniel, *J Chem Theory Comput*, 2016, **12**, 2335–2345.

15 A. Mutsuji, K. Saita and S. Maeda, *RSC Adv*, 2023, **13**, 32097–32103.

16 F. Maseras and K. Morokuma, *J Comput Chem*, 1995, **16**, 1170–1179.

17 L. W. Chung, H. Hirao, X. Li and K. Morokuma, *WIREs Computational Molecular Science*, 2012, **2**, 327–350.

18 L. W. Chung, W. M. C. Sameera, R. Ramozzi, A. J. Page, M. Hatanaka, G. P. Petrova, T. V Harris, X. Li, Z. Ke, F. Liu, H.-B. Li, L. Ding and K. Morokuma, *Chem Rev*, 2015, **115**, 5678–5796.

19 N. Sutin, in *Progress in Inorganic Chemistry*, John Wiley & Sons, Ltd, 1983, pp. 441–498.

20 R. A. Marcus, *Discuss. Faraday Soc.*, 1960, **29**, 21–31.

21 S. Fukuzumi, K. Ohkubo and T. Suenobu, *Acc Chem Res*, 2014, **47**, 1455–1464.

22 H. Makita and G. Hastings, *Proceedings of the National Academy of Sciences*, 2017, **114**, 9267–9272.

23 A. Y. Chan, A. Ghosh, J. T. Yarranton, J. Twilton, J. Jin, D. M. Arias-Rotondo, H. A. Sakai, J. K. McCusker and D. W. C. MacMillan, *Science*, 2023, **382**, 191–197.

24 G. A. Parada, Z. K. Goldsmith, S. Kolmar, B. P. Rimgard, B. Q. Mercado, L. Hammarström, S. Hammes-Schiffer and J. M. Mayer, *Science*, 2019, **364**, 471–475.

25 R. A. Marcus, *J Chem Phys*, 1956, **24**, 966–978.

26 H. Sumi and R. A. Marcus, *J Chem Phys*, 1986, **84**, 4894–4914.

27 L. Onsager, *J Am Chem Soc*, 1936, **58**, 1486–1493.

28 J. Tomasi, B. Mennucci and R. Cammi, *Chem Rev*, 2005, **105**, 2999–3094.

29 V. Barone and M. Cossi, *J Phys Chem A*, 1998, **102**, 1995–2001.

30 M. Cossi, N. Rega, G. Scalmani and V. Barone, *J Comput Chem*, 2003, **24**, 669–681.

31 A. V Marenich, C. J. Cramer and D. G. Truhlar, *J Phys Chem B*, 2009, **113**, 6378–6396.

32 J. M. Herbert, *WIREs Computational Molecular Science*, 2021, **11**, e1519.

33 M. Hatanaka and K. Morokuma, *J Chem Theory Comput*, 2014, **10**, 4184–4188.

34 Y. Harabuchi, M. Hatanaka and S. Maeda, *Chem Phys Lett*, 2019, **737**, 100007.

35 H. Scher and T. Holstein, *Philosophical Magazine B*, 1981, **44**, 343–356.

36 B. S. Brunschwig and N. Sutin, *Coord Chem Rev*, 1999, **187**, 233–254.

37 R. Improta, G. Scalmani, M. J. Frisch and V. Barone, *J Chem Phys*, 2007, **127**, 74504.

38 R. S. Mulliken, *J Am Chem Soc*, 1952, **74**, 811–824.

39 N. S. Hush, *Electrochim Acta*, 1968, **13**, 1005–1023.

40 C. Creutz, M. D. Newton and N. Sutin, *J Photochem Photobiol A Chem*, 1994, **82**, 47–59.

41 T. Le Bahers, C. Adamo and I. Ciofini, *J Chem Theory Comput*, 2011, **7**, 2498–2506.

42 C. Adamo, T. Le Bahers, M. Savarese, L. Wilbraham, G. García, R. Fukuda, M. Ehara, N. Rega and I. Ciofini, *Coord Chem Rev*, 2015, **304–305**, 166–178.

43 M. Rust, J. Lappe and R. J. Cave, *J Phys Chem A*, 2002, **106**, 3930–3940.

44 G. L. Closs and J. R. Miller, *Science*, 1988, **240**, 440–447.

45 J. R. Miller, L. T. Calcaterra and G. L. Closs, *J Am Chem Soc*, 1984, **106**, 3047–3049.

46 G. L. Closs, L. T. Calcaterra, N. J. Green, K. W. Penfield and J. R. Miller, *J Phys Chem*, 1986, **90**, 3673–3683.

47 S. Chaudhuri, S. Hedström, D. D. Méndez-Hernández, H. P. Hendrickson, K. A. Jung, J. Ho and V. S. Batista, *J Chem Theory Comput*, 2017, **13**, 6000–6009.

48 W. W. Parson, *J Phys Chem A*, 2017, **121**, 7297–7306.

49 M. M. Waskasi, M. D. Newton and D. V Matyushov, *J Phys Chem B*, 2017, **121**, 2665–2676.

50 W. W. Parson, *J Phys Chem B*, 2018, **122**, 8824–8833.

51 W. W. Parson, *J Phys Chem B*, 2021, **125**, 7940–7945.

52 A. Leo and A. Peluso, *J Phys Chem Lett*, 2022, **13**, 9148–9155.

53 A. Leo, F. Ambrosio, A. Landi and A. Peluso, *Chemistry (Easton)*, 2023, **5**, 97–105.

54 W. W. Parson and C. Burda, *J Chem Phys*, 2023, **159**, 154505.

55 I. Maqboul, *Int J Biol Macromol*, 2023, **237**, 124065.

56 S. Maeda, T. Taketsugu and K. Morokuma, *J Comput Chem*, 2014, **35**, 166–173.

57 S. Maeda, Y. Harabuchi, M. Takagi, T. Taketsugu and K. Morokuma, *The Chemical Record*, 2016, **16**, 2232–2248.

58 S. Maeda, K. Ohno and K. Morokuma, *Phys. Chem. Chem. Phys.*, 2013, **15**, 3683–3701.

59 A. Banerjee, N. Adams, J. Simons and R. Shepard, *J Phys Chem*, 1985, **89**, 52–57.

60 M. J. Bearpark, M. A. Robb and H. Bernhard Schlegel, *Chem Phys Lett*, 1994, **223**, 269–274.

61 S. Maeda, K. Ohno and K. Morokuma, *J Chem Theory Comput*, 2010, **6**, 1538–1545.

62 M. J. Frisch, G. W. Trucks, H. B. Schlegel, G. E. Scuseria, M. A. Robb, J. R. Cheeseman, G. Scalmani, V. Barone, G. A. Petersson, H. Nakatsuji, X. Li, M. Caricato, A. V. Marenich, J. Bloino, B. G. Janesko, R. Gomperts, B. Mennucci, H. P. Hratchian, J. V. Ortiz, A. F. Izmaylov, J. L. Sonnenberg, D. Williams-Young, F. Ding, F. Lipparini, F. Egidi, J. Goings,

B. Peng, A. Petrone, T. Henderson, D. Ranasinghe, V. G. Zakrzewski, J. Gao, N. Rega, G. Zheng, W. Liang, M. Hada, M. Ehara, K. Toyota, R. Fukuda, J. Hasegawa, M. Ishida, T. Nakajima, Y. Honda, O. Kitao, H. Nakai, T. Vreven, K. Throssell, J. A. Montgomery, Jr., J. E. Peralta, F. Ogliaro, M. J. Bearpark, J. J. Heyd, E. N. Brothers, K. N. Kudin, V. N. Staroverov, T. A. Keith, R. Kobayashi, J. Normand, K. Raghavachari, A. P. Rendell, J. C. Burant, S. S. Iyengar, J. Tomasi, M. Cossi, J. M. Millam, M. Klene, C. Adamo, R. Cammi, J. W. Ochterski, R. L. Martin, K. Morokuma, O. Farkas, J. B. Foresman, and D. J. Fox, Gaussian 16, Revision C.02, Gaussian, Inc., Wallingford CT, 2019.

63 J.-D. Chai and M. Head-Gordon, *Phys. Chem. Chem. Phys.*, 2008, **10**, 6615–6620.

64 R. Ditchfield, W. J. Hehre and J. A. Pople, *J Chem Phys*, 1971, **54**, 724–728.

65 W. J. Hehre, R. Ditchfield and J. A. Pople, *J Chem Phys*, 1972, **56**, 2257–2261.

66 P. C. Hariharan and J. A. Pople, *Theor Chim Acta*, 1973, **28**, 213–222.

67 M. S. Gordon, *Chem Phys Lett*, 1980, **76**, 163–168.

68 P. C. Hariharan and J. A. Pople, *Mol Phys*, 1974, **27**, 209–214.

69 M. M. Francl, W. J. Pietro, W. J. Hehre, J. S. Binkley, M. S. Gordon, D. J. DeFrees and J. A. Pople, *J Chem Phys*, 1982, **77**, 3654–3665.

70 R. C. Binning Jr. and L. A. Curtiss, *J Comput Chem*, 1990, **11**, 1206–1216.

71 V. A. Rassolov, J. A. Pople, M. A. Ratner and T. L. Windus, *J Chem Phys*, 1998, **109**, 1223–1229.

72 J.-P. Blaudeau, M. P. McGrath, L. A. Curtiss and L. Radom, *J Chem Phys*, 1997, **107**, 5016–5021.

73 V. A. Rassolov, M. A. Ratner, J. A. Pople, P. C. Redfern and L. A. Curtiss, *J Comput Chem*, 2001, **22**, 976–984.

74 T. Clark, J. Chandrasekhar, G. W. Spitznagel and P. V. R. Schleyer, *J Comput Chem*, 1983, **4**, 294–301.

75 M. J. Frisch, J. A. Pople and J. S. Binkley, *J Chem Phys*, 1984, **80**, 3265–3269.

76 A. Rohatgi, WebPlotDigitizer, https://automeris.io. Last Access: 2025/02/19.

77 S. Grimme, *J Comput Chem*, 2006, **27**, 1787–1799.

78 B. I. Dunlap, *J Chem Phys*, 1983, **78**, 3140–3142.

79 B. I. Dunlap, *Journal of Molecular Structure: THEOCHEM*, 2000, **529**, 37–40.

80 F. M. Bickelhaupt, *J Comput Chem*, 1999, **20**, 114–128.

81 L. P. Wolters and F. M. Bickelhaupt, *WIREs Computational Molecular Science*, 2015, **5**, 324–343.

82 F. M. Bickelhaupt and K. N. Houk, *Angewandte Chemie International Edition*, 2017, **56**, 10070–10086.

Chapter 5

General Conclusion

In this chapter of the general conclusion, the developed methods and findings in this study are summarized.

In chapter 3, the EDEEL method for intermolecular electron transfer reactions was developed and applied to the electron self-exchange reactions between transition metal complexes.[1] Calculated rate constants of thirteen transition metal complex pairs showed a good correlation with the experimental values, showing the efficiency of the EDEEL method and the analysis scheme with SX optimization. Moreover, the activation strain model (ASM) analysis was performed to clarify the relation of activation energies and deformation of the complexes. Two advantages of the EDEEL method were suggested. One is that the EDEEL can be used with an arbitral ab initio method of any program. The other one is that the EDEEL gives the decomposed energies and the geometries of EQs and SX for the ASM analysis. There were problems to be considered such as the solvent activation and the nuclear tunneling effect, leading to the study in chapter 4.

In chapter 4, the EDEEL method was extended to the intramolecular electron transfer reactions. Moreover, the SAES method was developed to incorporate the activation of solvent molecules around the solute, namely donor and acceptor species, for optimization of the crossing region of electron transfer. The SAES method allows to scan the SX region by adjusting the balance of the activation by solvent molecules orientation change and the activation by deformation of donor and acceptor species. The EDEEL method and the SAES method were applied to the intramolecular electron transfer reactions in nine radical anions[2–4]. The rate constants were calculated in three solvents, THF, DBE, and *n*-octane, with different polarity and

dielectric constants. Not only the parameters in the Marcus theory, the electronic couplings, the reorganization energies, and the reaction barriers, but also the nuclear tunneling effect was also calculated using the Scher-Holstein method. Obtained rate constants showed a good correlation with experimental values (in MTHF, DBE, and isooctane) from the Marcus normal region to the inverted region, reflecting the solvent dependency. Moreover, the breakdowns of the activation energies were calculated, showing a clear trend of activation. In the normal region, the solvent activation has more contribution. On the other hand, the activation by deformation of donor and acceptor is dominant in the inverted region due to the thinner barrier and large magnitude of the nuclear tunneling effect.

There are still problems to be considered. The EDEEL methods do not work well for some electron transfer systems in which charge delocalization occurs in the one-electron oxidized whole system. For example, charge recombination in radical ion pairs[5]. Accuracy of the SAES method may depend on the solvent polarity due to the lack of anharmonicity of the solvent orientation potentials, which is not considered in the current model. The introduction of anharmonicity may affect the results. Besides, dynamics and some specific solvent-solute interactions such as hydrogen bonds cannot be considered by the present SAES method. Further studies to solve these problems will be needed in the future.

There are many other types of electron transfer systems, as Marcus mentioned[6], which have not been dealt with in this study. Some of them are such as electron transfer between a molecule and electrode[7–10], photoinduced electron transfer like photoredox catalysts[11–13], proton coupled electron transfer[14], and electron transfer in protein[15,16]. These systems are also important in both pure and practical research and may need different computation approaches. There are other phenomena related to the potential crossing region such as excitation energy transfer[17,18], singlet fission[19,20], and triplet-triplet annihilation[21,22]. Potential crossing region optimization also has

potential for analyzing these phenomena and leading to the efficient design and discovery of new chemical systems and reactions.

References for Chapter 5

1 A. Mutsuji, K. Saita and S. Maeda, *RSC Adv*, 2023, **13**, 32097–32103.

2 J. R. Miller, L. T. Calcaterra and G. L. Closs, *J Am Chem Soc*, 1984, **106**, 3047–3049.

3 G. L. Closs, L. T. Calcaterra, N. J. Green, K. W. Penfield and J. R. Miller, *J Phys Chem*, 1986, **90**, 3673–3683.

4 G. L. Closs and J. R. Miller, *Science*, 1988, **240**, 440–447.

5 N. Mataga, T. Asahi, Y. Kanda, T. Okada and T. Kakitani, *Chem Phys*, 1988, **127**, 249–261.

6 R. A. Marcus, *Angewandte Chemie International Edition in English*, 1993, **32**, 1111–1121.

7 N.-T. Suen, S.-F. Hung, Q. Quan, N. Zhang, Y.-J. Xu and H. M. Chen, *Chem. Soc. Rev.*, 2017, **46**, 337–365.

8 K. Tvrdy, P. A. Frantsuzov and P. V Kamat, *Proceedings of the National Academy of Sciences*, 2011, **108**, 29–34.

9 A. Hagfeldt, G. Boschloo, L. Sun, L. Kloo and H. Pettersson, *Chem Rev*, 2010, **110**, 6595–6663.

10 C. Zhu, N. W. J. Ang, T. H. Meyer, Y. Qiu and L. Ackermann, *ACS Cent Sci*, 2021, **7**, 415–431.

11 M. H. Shaw, J. Twilton and D. W. C. MacMillan, *Journal of Organic Chemistry*, 2016, **81**, 6898–6926.

12 A. Y. Chan, A. Ghosh, J. T. Yarranton, J. Twilton, J. Jin, D. M. Arias-Rotondo, H. A. Sakai, J. K. McCusker and D. W. C. MacMillan, *Science*, 2023, **382**, 191–197.

13 N. A. Romero and D. A. Nicewicz, *Chem Rev*, 2016, **116**, 10075–10166.

14 G. A. Parada, Z. K. Goldsmith, S. Kolmar, B. P. Rimgard, B. Q. Mercado, L. Hammarström, S. Hammes-Schiffer and J. M. Mayer, *Science*, 2019, **364**, 471–475.

15 H. B. Gray and J. R. Winkler, *Annu Rev Biochem*, 1996, **65**, 537–561.

16 J. Blumberger, *Chem Rev*, 2015, **115**, 11191–11238.

17 J. E. Subotnik, J. Vura-Weis, A. J. Sodt and M. A. Ratner, *J Phys Chem A*, 2010, **114**, 8665–8675.

18 B. P. Rimgard, Z. Tao, G. A. Parada, L. F. Cotter, S. Hammes-Schiffer, J. M. Mayer and L. Hammarström, *Science*, 2022, **377**, 742–747.

19 M. B. Smith and J. Michl, *Chem Rev*, 2010, **110**, 6891–6936.

20 P. M. Zimmerman, C. B. Musgrave and M. Head-Gordon, *Acc Chem Res*, 2013, **46**, 1339–1347.

21 T. N. Singh-Rachford and F. N. Castellano, *Coord Chem Rev*, 2010, **254**, 2560–2573.

22 T. Serevičius, R. Komskis, P. Adomėnas, O. Adomėnienė, G. Kreiza, V. Jankauskas, K. Kazlauskas, A. Miasojedovas, V. Jankus, A. Monkman and S. Juršėnas, *The Journal of Physical Chemistry C*, 2017, **121**, 8515–8524.

Acknowledgement

All the research in this thesis was conducted under Professor Satoshi Maeda. I sincerely appreciate his kind supervision for six years. It was my great honor to be guided by such a talented person. He has managed to make time for our discussions from his precious time. His advice is always on point and provides me with a new perspective. I express my respect for his uncompromising attitude toward research.

I would like to thank Professor Junya Hasegawa, Professor Yasuchika Hasegawa, and Professor Tetsuya Taketsugu for serving as the members of the thesis committee. Their advice allowed me to improve my research.

Dr. Kenichiro Saita supervised me in my first year in the laboratory. He taught me the fundamentals of research life. He kindly guided me even after his moving to the quantum chemistry laboratory. I would like to express my sincere gratitude to him. My thanks go to Dr. Yu Harabuchi for discussions on my study. My thanks also go to Professor Keisuke Takahashi not only for discussion but also for giving me kind advice on my career.

I would like to thank all the seniors. Especially, Dr. Yosuke Sumiya, Dr. Makito Takagi, Dr. Kanami Sugiyama, Dr. Takuma Ito, Dr. Hiroaki Okada, and Dr. Hitoshi Nabata, who had kindly taught me many things and helped me countless times. Their profound knowledge and skills were always great inspirations to me. It was also a great pleasure to have a conversation with them at the conferences.

I would like to express my gratitude to Kazuma Sawamoto, Yotaro Tabata, and Wataru Kanna for being my colleagues in my research life. Especially, Wataru Kanna has been a great support and inspiration throughout the three years of doctoral course. I respect his enthusiasm for his research.

Most part of the computation in this study was performed using Research Center for Computational Science (RCCS), Okazaki, Japan. This research life was made possible by the fellowships, Hokkaido University Ambitious Doctoral Fellowship and Hokkaido University EXEX Doctoral Fellowship Ambitious Doctoral Course. I sincerely appreciate the financial support from Hokkaido University.

Finally, I express my deepest gratitude to my family for their selfless support.